Front. Mech. Eng. 2025, 20(3): 22
https://doi.org/10.1007/s11465-025-0838-2

REVIEW ARTICLE

Heat transfer in cutting and grinding processes: mechanisms, models, and applications

Xiaotong CHEN[a], Xianggang KONG[a], Min YANG (✉)[a], Fan QIANG[b], Yanbin ZHANG[a], Xin CUI[a], Mingzheng LIU[a], Benkai LI[a], Xiao MA[a], Changhe LI[a]

[a] Key Laboratory of Industrial Fluid Energy Conservation and Pollution Control (Ministry of Education), Qingdao University of Technology, Qingdao 266520, China
[b] Jining Antai Mine Equipment Manufacturing Co., Ltd., Jining 272300, China
✉ Corresponding author. Email: 18266487809@163.com (Min YANG)

ABSTRACT The heat transfer process is a critical topic in the field of cutting and grinding machining, playing a vital role in reducing machining temperatures and improving machining quality. In these operations, heat transfer is generally characterized by specific parameters, including the energy distribution coefficient and the convective heat transfer coefficient. These parameters affect the magnitude and direction of energy flow in the heat transfer process, directly impacting cutting and grinding temperatures. However, comprehensive reviews summarizing current studies on heat transfer processes are lacking. To effectively control heat transfer, thereby managing cutting/grinding temperatures while improving workpiece surface quality, it is essential that we understand how machining parameters, material properties, and cooling methods influence the heat transfer, and this knowledge is critical for guiding the practical production. This paper analyzes and summarizes heat transfer process parameter models in cutting and grinding operations. First, the study examines energy flow and distribution ratios during cutting and grinding processes, classifying and summarizing various energy partition coefficient models based on different research methods. Second, convective cooling mechanisms in cutting and grinding machining are analyzed, summarizing models of convective heat transfer coefficients. The paper then reviews the practical application of these models, highlighting the influence law of each factor on the models. Finally, the most widely recognized and accurate models of heat transfer process parameters are summarized and identified, analyzing the mechanisms by which different factors alter these parameters. Based on current challenges in heat transfer process parameter research, the paper proposes possible future research directions. The goal is to provide theoretical guidance and technical support for advancing research in heat transfer and improving thermal control in machining.

KEYWORDS cutting, grinding, energy distribution coefficient, convective heat transfer coefficient, heat transfer theory

1 Introduction

Thermal damage during machining is one of the main factors limiting the productivity of the workpiece and the quality of the finished product [1]. In industries such as aerospace and toolmaking, machining accuracy and workpiece performance are critical [2–4]. However, operations such as turning, drilling, milling, and grinding generate heat due to the interaction of various parts. In particular, grinding produces a substantial amount of heat that accumulates in the machining area [5–7]. Excessive heat buildup and rising temperature negatively affect the surface quality and performance of the workpiece and may even reduce the lifespan of the cutting tool or grinding wheel [8–10].

A portion of the energy input into the machining area is converted into heat through the interaction between the tool and the workpiece. This heat is transferred between different parts in the machining area via the contact interface. During this process, the amount of heat transferred to each part continuously varies due to multiple influencing factors

Received November 17, 2024; accepted February 13, 2025; online June 20, 2025

[11,12]. Aiming to better understand and investigate the mechanisms and variations in heat transfer, specific parameters are used to represent the process. In cutting and grinding machining, most of the generated heat is mainly transferred to the workpiece. In non-dry machining processes, the coolant also absorbs a considerable portion of the heat due to its effective cooling properties [13,14]. Therefore, two key heat transfer process parameters are used: the energy distribution coefficient (EDC) for measuring the amount of heat transferred into the workpiece and the convective heat transfer coefficient (CHTC) for measuring the heat transfer capacity of the fluid. The EDC quantifies the proportion of energy transferred into the workpiece relative to the total energy input into the machining area [15–17]. Aiming to control the surface temperature of the workpiece during machining and ensure quality, the heat transferred to the workpiece should be minimized (that is, the EDC should be reduced) [18]. Through the construction of a model, the influencing factors of the EDC can be identified and adjusted to reduce its value effectively [19,20]. The CHTC characterizes the efficiency of heat exchange between a fluid and a solid surface. In non-dry machining, coolant removes heat from the machining area through thermal convection with the workpiece, tool, or grinding wheel. In addition, high-speed rotation of the workpiece or machining tool can enhance convective heat transfer due to airflow effects. The solution of CHTC is also notably complex due to the influence of machining parameters, workpiece material, coolant type, and flow rate, affecting the efficiency of convective heat transfer [21,22]. Simultaneously, excessive use of coolant raises environment and health concerns [23–25]. Aiming to address these concerns, researchers have explored alternative lubrication methods, such as the minimum quantity lubrication (MQL) [26–28] and nanofluid minimum quantity lubrication (NMQL) [27,29,30], which further complicate the modeling and calculation of CHTC. However, constructing accurate CHTC models enables effective evaluation of convective heat transfer within the machining zone and helps identify strategies to enhance CHTC, thereby reducing heat accumulation, particularly in the grinding zone [31–33].

The study of heat transfer process parameters is conducive to an in-depth understanding of the laws of heat transfer in the machining area and control of the influencing factors, which is of great significance for the control of temperature in the machining process. The EDC reflects the proportion of heat transferred to the workpiece, and the CHTC reflects the heat carried away by the cutting fluid, all of which have a direct influence on the temperature change in the machining zone [34–36].

Domestic and international researchers have extensively studied the heat transfer process parameters, as shown in Fig. 1. In the machining process, the main energy source is supplied by the machining tool or grinding wheel. The contact area between the tool and the workpiece becomes a major heat source, generating a substantial amount of heat that accumulates in the machining area [37–39]. Therefore, when studying the heat transfer process, establishing a heat source model within the machining area, commonly represented as either a triangular or rectangular heat source, is necessary [40–42]. Heat generated during machining is distributed among several destinations, including the workpiece, the tool or grinding wheel, the coolant, and the chips. The amount of heat dissipated through other methods is relatively small. Therefore, most researches typically assume that the heat generated in the machining zone is transferred only to the following components: the workpiece, the grinding wheel or tool, the coolant, and the debris [43].

The energy transferred to the workpiece is a primary focus of study, and its proportion relative to the total energy input into the machining area is defined as the EDC. Two main approaches to determining this coefficient are as follows: theoretical analysis or a combined approach with experiments. Models established through theoretical analysis typically do not require experimental data. These models include analytical methods that consider factors such as abrasive grain–workpiece contact [44,45] and the physical properties of materials [46]. The required parameters for these models are inherent to the workpiece or machining tool, along with standard machining parameters, which can be used for simulation and model computation. By contrast, models that incorporate experimental data require not only inherent material and process parameters but also certain values that must be obtained through experimental measurements [47,48]. For instance, models that consider surface temperature rise of the workpiece or the CHTC depend on experimentally measured surface temperature data and CHTC values during machining to construct the model [49,50]. CHTC modeling aims to facilitate energy transfer to the cooling fluid. The difficulty of model construction lies in the complexity of fluid changes during processing and the variety of cooling methods with technological advancements [51–53]. The model is constructed based on different ideas. One category focuses on fluid flow, considering factors such as hydrodynamics, different Péclet numbers, particle contact conditions, and other models. The other category considers the boiling state of the fluid, because varying levels of cam cause the fluid to transition between different boiling states, namely, no

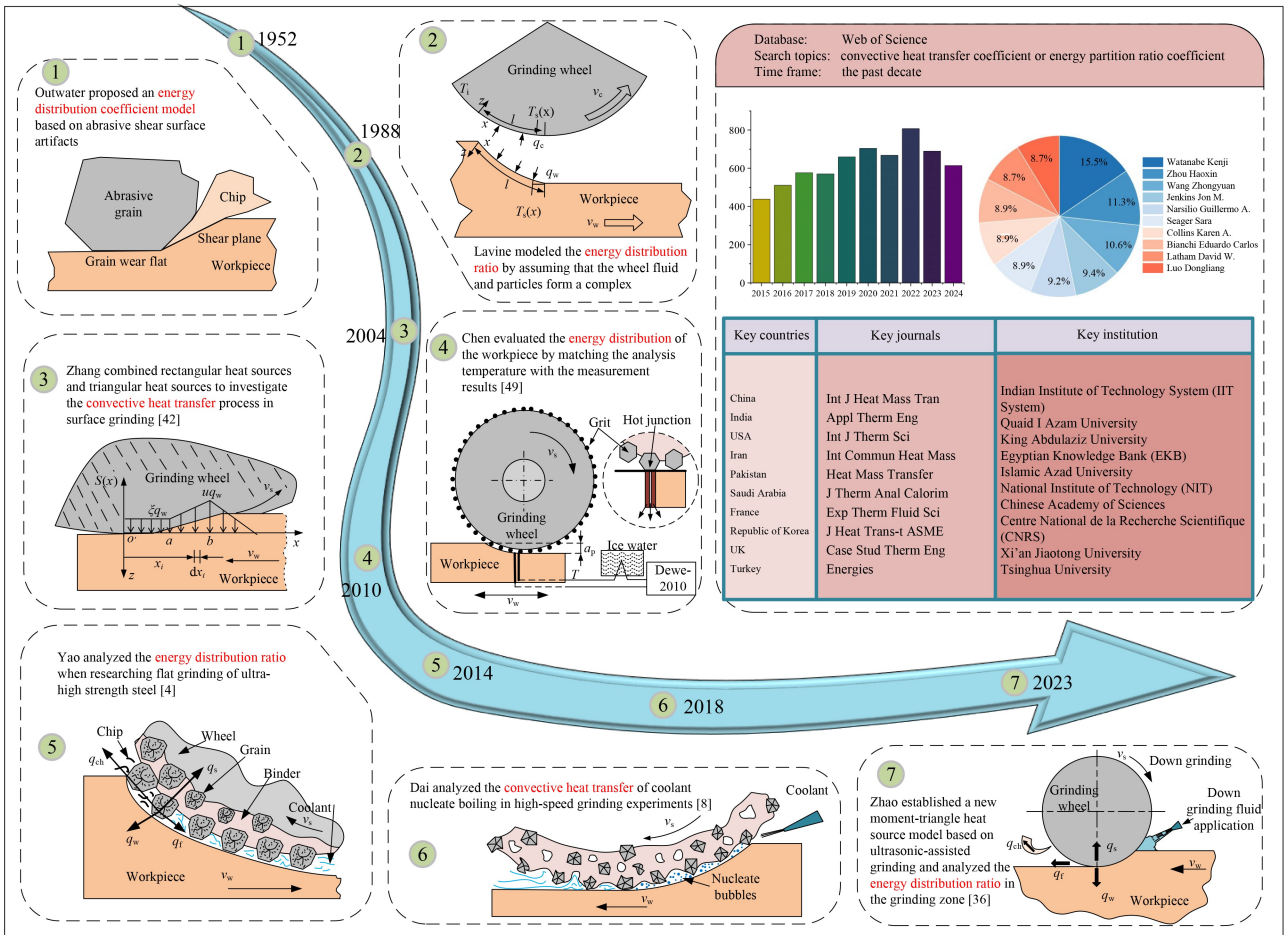

Fig. 1 History of the development of thermal process coefficient modeling [4,8,36,42,49].

boiling, nucleate boiling, transition boiling, and film boiling, which notably impact model construction [28]. Additionally, with the emergence of new cooling methods such as MQL, parameters such as the number of cooling droplets [54,55] and the diffusion area [27,56,57] must be considered.

The research framework is shown in Fig. 2, focusing on the study of heat transfer process parameters in machining, specifically, the EDC and CHTC. The two coefficients are investigated across different machining modes, including cutting (turning, milling, and drilling) and grinding. Among these modes, grinding typically generates more heat due to its larger contact area, making it more prone to thermal damage [58,59]. Therefore, EDC and CHTC have been studied more extensively and carefully in the context of grinding. Aiming to investigate heat transfer process parameters across different machining modes, researchers have adopted different ideas and proposed a variety of models. This study compiles and summarizes these models and their applications, aiming to address current problems in heat transfer research and provide valuable references for future studies.

In response to existing challenges, this study presents future research directions for the heat transfer process in cutting and grinding machining. By summarizing the EDC and CHTC models and their applications, the influence of grinding parameters, grinding wheel parameters, workpiece physical parameters, cooling methods, and other factors on heat transfer process parameters, as well as the underlying influence mechanisms, are revealed. The classification emphasizes high-precision models developed under various conditions and analyzes how each factor affects the heat transfer process. The goal is to provide theoretical guidance and technical support for advancing the understanding of heat transfer mechanisms, ultimately contributing to improved workpiece quality and processing efficiency.

2 Energy distribution mechanisms and models

In the machining process, excessive heat is generated due to material deformation, contact friction and other factors, and is transferred to various parts of

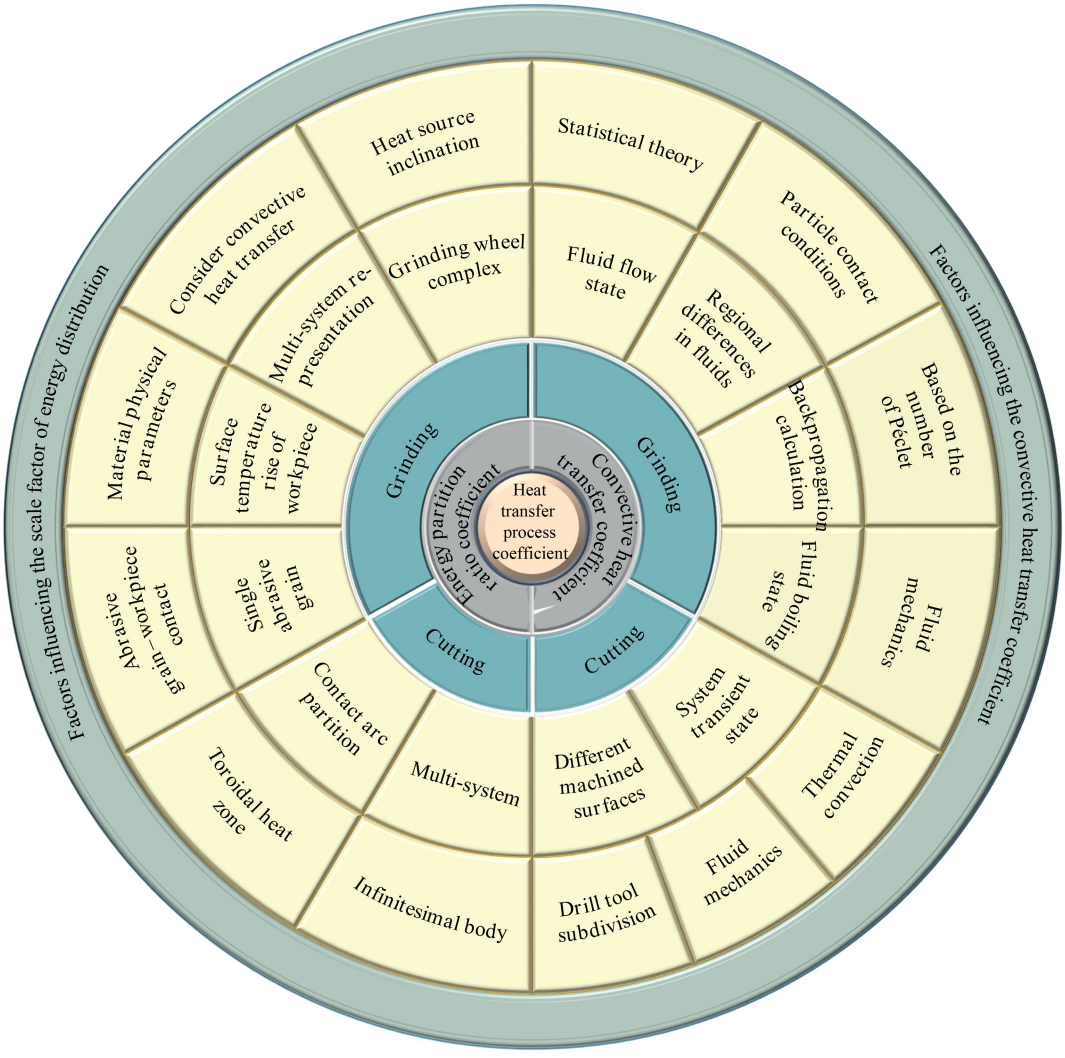

Fig. 2 Review narrative logic.

the processing area. The fraction of heat transferred to the workpiece substantially affects its temperature, making this proportion a key focus in the study of heat transfer process parameters. This proportion is referred to as the EDC R_w. The study of R_w is a prominent research topic domestically and internationally, with many scholars exploring it using different methods.

The EDC is a complex variable to determine; however, its fundamental definition is the ratio of the energy transferred to the workpiece to the total energy input in the machining area. Therefore, the EDC of the workpiece is expressed as follows:

$$R_w = \frac{q_w}{q_t}, \tag{1}$$

where q_w represents the heat transferred to the workpiece and q_t is the total heat input to the machining area, which is closely related to factors such as machining power. The following section provides an overview of EDC values for different machining methods.

2.1 Turning

Turning is a common metal cutting process widely used in machinery manufacturing, automotive industry, and other fields. This process plays a particularly important role in the production of precision parts [60]. During turning, most of the heat is generated by friction between contact surfaces, while plastic deformation of the workpiece material also contributes to heat generation [61–63]. The high temperatures and heat distribution within the cutting zone are key factors influencing tool wear and overall machining quality [64]. The heat distribution among the cutting tool, chip, and workpiece is primarily determined by the relative thermophysical properties of the tool and workpiece materials [65,66]. The following section presents and summarizes reported EDC models for the cutting process.

2.1.1 Multi-system calculation based on analytical methods

In 2005, Quan and He [67], using an analytical method, assumed that all the cutting deformation work is converted into heat, with no heat lost to the external environment, and that the heat at the contact surfaces is uniformly distributed. As shown in Fig. 3, let R_1 represent the proportion of heat flowing to the chip from the shear surface, R_2 the proportion of heat flowing to the workpiece from the tool–chip interface, and R_3 the proportion of heat flowing to the workpiece from the tool–workpiece interface.

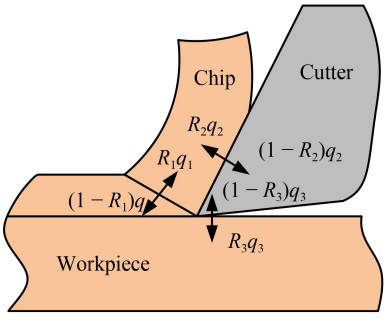

Fig. 3 Heat sources and heat distribution in the cutting zone.

For orthogonal free dry cutting, the EDCs for energy distribution are as follows:

$$R_1 = \frac{1}{1 + 1.328\sqrt{\dfrac{a_1 \Lambda_h}{v_c h_D}}}, \tag{2}$$

$$R_2 = \frac{q_2(l_f \bar{A}/k_t) - \bar{\theta}_s + \theta_0'}{q_2\left[\dfrac{l_f \bar{A}}{k_t} + \dfrac{0.377 l_f}{k_w\sqrt{v_{ch} l_f/(4a_2)}}\right]}, \tag{3}$$

where a_1 and a_2 are the thermal diffusivity of the workpiece material at different temperatures, Λ_h is the cutting deformation coefficient, v_c is the cutting speed, h_D is the cutting thickness, q_2 is the cutting heat generated per unit of time at the tool–chip interface, l_f is the tool–chip contact length, θ_0' is the initial temperature of the tool, $\bar{\theta}_s$ is the average temperature of the shear surface, k_t is the thermal conductivity of cutting tools, k_w is the thermal conductivity of the workpiece material, A_t is the tool–chip contact area coefficient, and v_{ch} is the chip flow rate.

Determining the values of parameters such as heat flow density and friction on the rear blade face is difficult; thus, these values are often ignored in practical calculations.

2.1.2 Based on infinitesimal element

In 2021, Zhao et al. [68] introduced the concept of tool–chip contact infinitesimal element and developed a time-varying tool–chip EDC prediction model for coated tools. They clarified the time-varying effect of tool–chip heat distribution coefficients and revealed the coupled effects of tool coating thickness, tool coating, tool substrate, and the thermophysical properties of the workpiece. Additionally, they examined the influence of intermittent milling and machining speed on heat distribution at the tool–chip interface.

As shown in Fig. 4, the infinitesimal element model of the cutting process using a coated tool is taken as a semi-infinite body, based on the principles of energy conservation and the Block criterion. At a given moment t, the tool–chip contact infinitesimal element is also considered a semi-infinite body. The coated tool is assumed to maintain perfect thermal contact with the chip, indicating no additional thermal resistance at the interface. Furthermore, the materials are considered isotropic with constant physical properties, and no internal heat generation occurs within either the coated tool or the chip. Under these assumptions, the time-varying distribution coefficient of the tool–chip interface for the coated tool can be calculated as follows:

$$R_{chip}(t) = \frac{A(x_1, k_c, \lambda_c, k_s, \lambda_s, t)}{A(x_1, k_c, \lambda_c, k_s, \lambda_s, t) + 3[2B(k_w, \lambda_w, t)]^{-1}}, \tag{4}$$

where

$$A(x_1, k_c, \lambda_c, k_s, \lambda_s, t) = \frac{4\sqrt{\lambda_c}}{k_c} \cdot \sum_{m=0}^{\infty} |C|^{n+1} \cdot \sqrt{\frac{t}{\pi}}\left\{\exp\left[-\frac{(n+1)^2 x_1^2}{t\lambda_c}\right] - \operatorname{erfc}\left[-\frac{(n+1)x_1}{\sqrt{t \cdot \lambda_c}}\right]\right\} + \frac{2}{k_c}\sqrt{\frac{t\lambda_c}{\pi}}$$

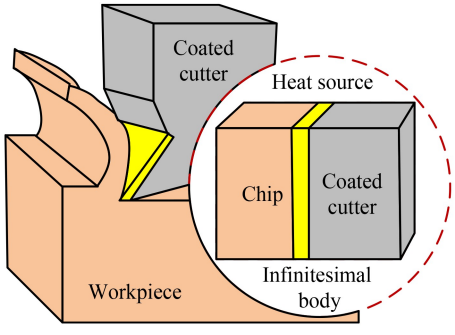

Fig. 4 Coated tool cutting and machining of infinitesimal element.

is the time-varying coefficient considering the coating thickness x_1, the coating thermal conductivity k_c, the coating thermal conductivity rate λ_c, the substrate thermal conductivity k_s, and the substrate thermal conductivity rate λ_s, while

$$B(k_w, \lambda_w, t) = \frac{2}{k_w}\sqrt{\frac{t\lambda_w}{\pi}}$$

is the time-varying coefficient considering the workpiece thermal conductivity k_w and the workpiece thermal conductivity rate λ_w.

2.2 Milling

Milling is mainly used to remove material and shape the workpiece to the desired dimensions. The heat generated during the milling process mainly originates from the friction between the tool and the workpiece surface. This heat directly affects tool wear and durability, as well as the machining accuracy and surface quality of the workpiece [69].

Komanduri and Hou [70] presented an analytical model of orthogonal cutting to determine energy distribution. They also confirmed the relationship between energy distribution in the main shear zone in orthogonal cutting for different materials and cutting conditions and the heat number $N_{th.n} = h_u \cdot v_c \cdot \alpha^{-1}$, where h_u is the undeformed chip thickness and α is the temperature diffusion coefficient of the workpiece material. To this day, research on the EDC in milling processes has mainly focused on the development of empirical models for determining energy distribution during cutting.

In 2012, Sölter and Gulpak [71] discretized the grinding arc into four domains V_i and determined the heat flux from the workpiece by iteratively applying an inverse process. They assumed that the associated cutting power remained approximately constant within each domain.

As shown in Fig. 5, assuming that 100% of the spindle's effective power is converted into mechanical energy, the proportion of energy R_w dissipated to the workpiece within the domain Ω_i can be calculated as follows:

$$R_{w,i} = \frac{q_w A_i}{P_{el.meas.i}}, \tag{5}$$

where A_i is the area of region Ω_i and $P_{el.meas.i}$ is the effective spindle power.

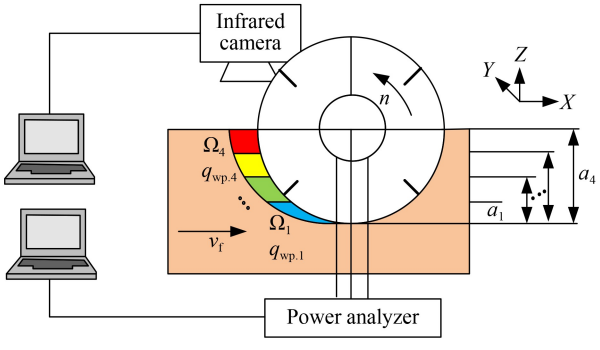

Fig. 5 Experimental setup [71].

2.3 Drilling

Drilling is mainly used for creating holes in workpieces. In the drilling process, when the drill bit contacts the workpiece material, friction generates a substantial amount of heat, especially at high drilling speeds [72,73]. During the stripping and movement of chips, the friction between the chips, drill bit, and workpiece also generates heat [74]. Furthermore, the heat flowing into the tool is unfavorable for surface processing in plough-slip [75].

In 2016, Cuesta et al. [76] proposed a model based on a new experimental approach to determine the difference in heat transfer to the workpiece between dry and lubricated drilled holes. The temperature of the sidewall of a drilled hole depends on the heat distribution between the chip and the workpiece. The heat flow in the drilled hole can be considered as an instantaneous transfer to the surface drilled, which is then propagated by conduction. As shown in Fig. 6, the heat in the workpiece can be approximated as a cylindrical annulus. Therefore, the heat transferred to the workpiece is as follows:

$$q_w = mcT = L\rho(\pi/4)(d_2^2 - d_1^2)cT, \tag{6}$$

where c is the specific heat capacity, ΔT is the temperature rise, L is the depth of the borehole, d_1 is the borehole diameter, d_2 is the diameter of the heated cylinder, and ρ is the density.

Assuming that all work is converted to heat, the heat produced during drilling (q_t) is calculated as shown below.

$$q_t = W = (\pi/4) \cdot d_{drill}^2 \cdot LK_s, \tag{7}$$

where K_s is the ratio of cutting force to cutting cross-sectional area, d_{drill} is the diameter of the drill bit, and the proportion of energy entering the workpiece can be calculated from the definition. Subsequently,

$$R_w = \frac{q_w}{q_t} = \frac{\rho(d_2^2 - d_1^2)c\Delta T_{max} f_z z}{8M_z}, \tag{8}$$

where f_z is the feed per tooth, z is the number of teeth, and M_z is the torque.

Studies on modeling the EDC coefficient of proportionality in planning and boring machining are limited, and no relevant models currently exist; thus, they will not be discussed further in this study.

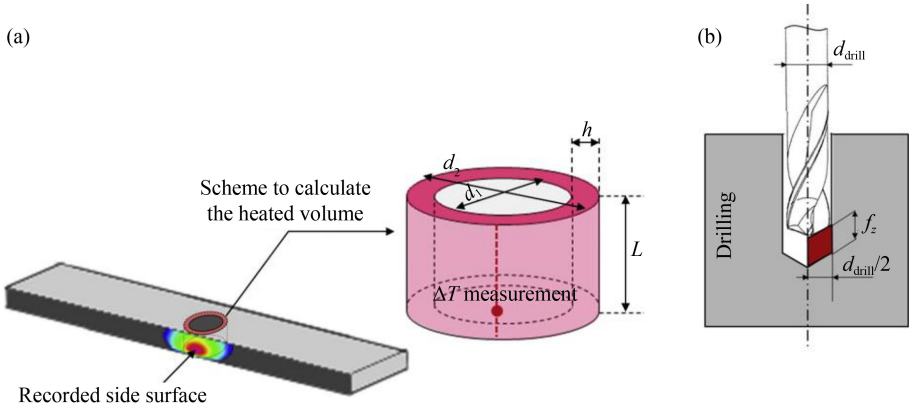

Fig. 6 Schemes employed to calculate (a) heated volume and (b) removed material [76].

Table 1 provides a summary of the factors influencing the EDC model in cutting machining.

2.4 Grinding

Grinding is a machining process suitable for finishing high-hardness materials and is generally the final process for important components. Therefore, ensuring that components of acceptable quality are produced is crucial [77,78]. For some materials, thermal damage is a major limiting factor in improving removal rates while maintaining surface quality [79,80].

Simultaneously, during grinding, material is removed by a large number of abrasive particles with a substantially shallow depth of cut. Negative cutting angles result in higher energy consumption per unit volume of material removed compared to other cutting processes, such as milling and turning [81–83]. A schematic of the heat sources generating heat around the abrasive grits is shown in Fig. 7. Heat is generated at the following three locations [84]:

(a) Grain wear flat–workpiece interface, AB

(b) Shear surface, BC

(c) Abrasive grain and Grinding debris contact interface, BD

The EDC for the grinding process has been studied by many scholars domestically and internationally. In their investigations, some scholars have derived models based on the grinding wheel's abrasive grains, such as the single-grain model and the abrasive grains–workpiece contact model [85], among others. Other scholars combine experimental research, consider the physical properties of the processed material, or measure grinding temperatures through grinding experiments to derive energy distribution models. Additionally, some researchers have explored convection heat transfer, heat-source inclination, and other factors to conduct an in-depth study of the model. Below are the EDC models that have been reported or introduced in the grinding process.

2.4.1 Based on a single grain of grinding wheel

The EDC model for grinding, based on the contact

Table 1 Modeling of EDC in cutting operations

Processing method	Model category	Reference	Basis of the model	Machining tools	Cooling condition	Model calculation results	Model accuracy
Turning	Multi-system calculation based on analytical methods	Quan and He [67]	The following assumptions are presented: the cutting deformation work is converted into heat, no heat is transferred to the outside world, and the heat is uniformly distributed on the contact surface. A planar heat source model is used	YT15 tools, alumina-based ceramic tools	–	9.5%–20.0%	–
	Based on infinitesimal element	Zhao et al. [68]	The concept of infinitesimal element in tool–chip contact is proposed	Coated tools	–	37.65%–62.14%	56.52%
Milling	Based on different regions of the cutting contact arc	Sölter and Gulpak [71]	The cutting arc is discretized into four domains. Assuming that the associated cutting power is approximately constant in each domain, 100% of the effective power of the spindle is converted into mechanical energy	Sandvik R390-11 T3 08E-PL 1010	Dry milling	9%–46%	–
Drilling	Consider a circular heat zone	Cuesta et al. [76]	Drilling heat flow is considered to be an instantaneous transfer to the surface being drilled, propagated by conduction, with all work converted into heat	TiAlN coated carbide tools	Oil lubrication/dry drilling	6.5%–7.8% for oil lubrication (max); 20% for dry drilling	–

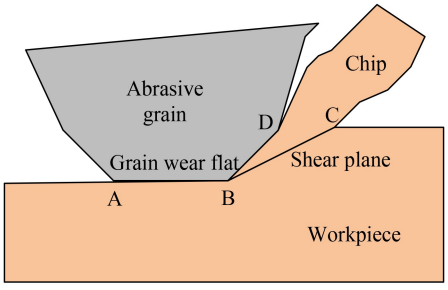

Fig. 7 Grain grinding process.

between a single abrasive grain and the workpiece, was first proposed by Rowe [84] to measure the thermal attributes of a single abrasive grain through grinding tests. The proportional model of heat distribution for a single abrasive grain is applicable to normal and slow-feed grinding processes, regardless of the grinding process parameters and cooling methods.

GUO et al. [86] constructed a numerical calculation model for the profile grinding temperature, using the distribution of a triangular heat source within the grinding arc and simplifying the one-dimensional heat-conducting process. This model was also based on the theoretical analysis of the continuous grinding temperature of a plane. Therefore, the abrasive particle was modeled as a truncated cone.

On this basis, Guo [87] conducted a theoretical discussion and experimental analysis of the profile grinding temperature. Using this model, the proportion of energy entering the workpiece material in the ordinary flat grinding processing zone can be calculated, as shown in Fig. 8. The conical abrasive grain moves along the surface of the workpiece with a velocity of v_s. The grinding heat is conducted along the contact surface $A_0 = \pi r_0^2$ between the abrasive grain and the workpiece, and is transferred to the grain, the workpiece, and the coolant. The proportion of heat transferred to the workpiece at the initial moment is R_{dry}, while the remaining heat is transferred to the abrasive grain. The maximum temperature rise at the abrasive grain–workpiece contact surface is T_{gmax}.

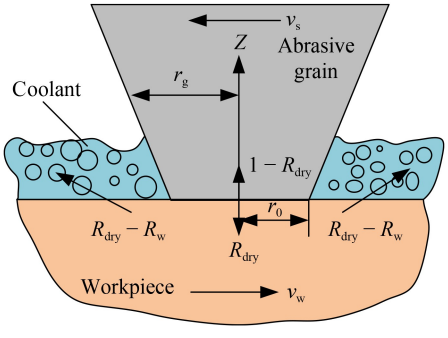

Fig. 8 Heat distribution model for single grain grinding.

$$\begin{cases} T_{gmax} = 1.13\dfrac{(1-R_{dry})q_t}{(k\rho c)_g^{1/2}}\left(\dfrac{l_c}{\nu_s}\right)^{1/2}\dfrac{1}{f(\zeta)A}, \\ \zeta \equiv \left(\dfrac{\gamma^2\pi\alpha_g l_c}{2A_0\nu_s}\right)^{1/2}, \end{cases} \tag{9}$$

where the subscript g refers to the abrasive grain, and α_g represents the thermal diffusivity of the abrasive grain. The function γ is the geometry coefficient of a single grain, defined as $\gamma = d_{rg}/d_z$. A is the ratio of the total wear area of the protruding abrasive grains on the grinding wheel surface to the total area of the grinding wheel. Additionally, r_g denotes the radius of the top of the conical abrasive grains.

When the coolant enters the grinding wheel aperture, its running speed matches that of the grinding wheel. At this time, the contact surface between the workpiece, as well as the highest temperature rise of the machined surface, are T_{fmax} and T_{wmax}, respectively.

$$T_{fmax} = 1.06\frac{(R_{dry}-R_w)q_t}{(k\rho c)_f^{1/2}}\left(\frac{l_c}{v_s}\right)^{1/2}\frac{1}{1-A}, \tag{10}$$

$$T_{wmax} = 1.06\frac{R_w q_t}{(k\rho c)_w^{1/2}}\left(\frac{l_c}{v_w}\right)^{1/2}, \tag{11}$$

where the subscripts f and w denote the coolant and the workpiece material, respectively.

Assuming that the maximum temperature rise at the contact surface between the workpiece and the abrasive grain, the contact surface between the workpiece and the coolant, and the machined surface of the workpiece are all equal (i.e., $T_{gmax} = T_{fmax} = T_{wmax}$), the heat distribution ratio of the heat transferred into the inner part of the workpiece material, R_w, can be calculated as follows [86,88]:

$$R_w = \left[1+\Omega\left(\frac{v_s}{v_w}\right)^{1/2}\right]^{-1}, \tag{12}$$

$$\Omega \equiv 0.94\frac{(k\rho c)_g^{1/2}}{(k\rho c)_w^{1/2}}Af(\zeta) + \frac{(k\rho c)_f^{1/2}}{(k\rho c)_w^{1/2}}(1-A). \tag{13}$$

When the temperature of the grinding arc exceeds the boiling point temperature of the coolant, the coolant enters the bubble nucleation boiling state, enhancing the convective heat transfer capacity. However, when the temperature of the grinding arc exceeds 130 ℃, the coolant in the arc area is transitions into a film boiling state, notably reducing its heat transfer capacity. At this point, the coolant loses its ability to transfer heat and cool the system. In typical grinding processes, the grinding temperature in the contact arc zone can exceed 130 ℃, thereby causing $(k\rho c)_f = 0$. The single grain heat distribution ratio model does not consider the energy

carried away by the chips. The melting energy of steel-like metal materials is approximately 6 J/mm^3, which is equivalent to 45% of the chip energy. Therefore, the proportion of heat removed by the chip, R_{ch}, can be calculated as follows:

$$R_{\mathrm{ch}} = \frac{0.45e_{\mathrm{sch}}}{e_{\mathrm{s}}} \approx \frac{6}{e_{\mathrm{s}}}, \tag{14}$$

where e_{sch} is the specific chip formation energy and e_{s} is the specific grinding energy.

Considering the heat carried away by the chips and subtracting the proportion of this heat, the model for the heat distribution ratio of a single grain gives the proportion of energy entering the workpiece, R_{w}, for ordinary flat grinding as follows [89]:

$$\begin{aligned} R_{\mathrm{w(AB)}} &= R_{\mathrm{w(EF)}} \\ &= \left(1 - \frac{6}{e_{\mathrm{s}}}\right)\left[1 + 0.94\frac{(k\rho c)_{\mathrm{g}}^{1/2}}{(k\rho c)_{\mathrm{w}}^{1/2}} Af(\zeta)\left(\frac{v_{\mathrm{s}}}{v_{\mathrm{w}}}\right)^{1/2}\right]^{-1}. \end{aligned} \tag{15}$$

In 2010, Xu et al. [90] improved the traditional heat-source model by integrating the heat transfer process, the end surface temperature of single wear grains, and a one-dimensional heat transfer model to analyze the dynamic effects of grinding on heat transfer. They then studied the energy distribution ratio. As shown in Fig. 9, the wear grains are assumed to be cylindrical, and thermal convection between the sides of the grains and the surrounding air is neglected. Under these conditions, the heat transfer state of the wear grains can be modeled as a semi-infinite cylindrical unsteady state with one-dimensional heat transfer, subject to the first boundary condition.

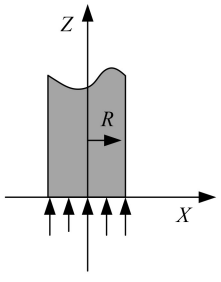

Fig. 9 Heat transfer model of a single wear particle.

In time t, the heat transfer is q_{a} per square meter, and then the heat transferred to the workpiece is calculated as follows:

$$q_{\mathrm{w}} = q_{\mathrm{t}} - q_{\mathrm{a}}\pi R^2 = F_{\mathrm{t}}v_{\mathrm{s}}\tau_0 - 2b\sqrt{\frac{\tau_0}{\pi}}(\theta_{\mathrm{a}} - \theta_0)\pi R^2, \tag{16}$$

where F_{t} is the tangential grinding force, b is the heat storage coefficient, θ_0 is the average temperature of the abrasive grain, and θ_{a} is the surface temperature of the workpiece. Introducing the empirical formula for the grinding force F_{t}, the EDC is given by the following:

$$R_{\mathrm{w}} = 1 - \frac{2b(\theta_{\mathrm{a}} - \theta_0)\sqrt{\pi}R^2}{C_1 v_{\mathrm{s}}^{-x+1/2} v_{\mathrm{w}}^{y} a_{\mathrm{p}}^{z+1/4} d_{\mathrm{s}}^{1/4}}. \tag{17}$$

Based on Eq. (17), R_{w} is influenced by the thermal properties of the wear grain and the coating material, as well as by the mechanical properties of the coating material and the grinding parameters.

2.4.2 Considering abrasive grain–workpiece contact

In 2001, Rowe [84] studied the heat-source modeling using an inclined heat-source model, as shown in Fig. 10. In this model, the total heat directed toward the contact zone is divided into four directions, with the proportions of heat in each direction summing up to the total heat.

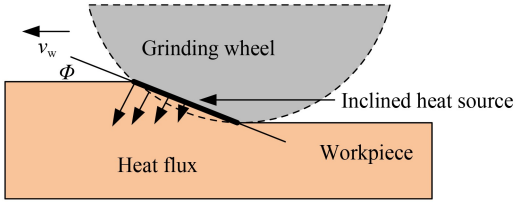

Fig. 10 Inclined heat source. The contact zone is represented by a straight line at an angle Φ to the direction of movement.

$$q_{\mathrm{t}} = q_{\mathrm{w}} + q_{\mathrm{s}} + q_{\mathrm{ch}} + q_{\mathrm{f}}, \tag{18}$$

$$1 = R_{\mathrm{w}} + R_{\mathrm{s}} + R_{\mathrm{ch}} + R_{\mathrm{f}}, \tag{19}$$

where q_{s} is the heat flow to the abrasive grain, q_{ch} is the heat flow to the chip, and q_{f} is the heat flow to the coolant. $R_{\mathrm{w}} = q_{\mathrm{w}}/q_{\mathrm{t}}$, and so on.

After rearrangement, the heat absorbed by the workpiece and the grain can be determined.

$$q_{\mathrm{ws}} = q_{\mathrm{w}} + q_{\mathrm{s}} = q_{\mathrm{t}} - q_{\mathrm{ch}} - q_{\mathrm{f}}. \tag{20}$$

The heat of the abrasive chips, q_{ch}, and the heat of the fluid, q_{f}, can be estimated based on the processing conditions. The temperature of the abrasive chips is assumed to be slightly below the melting temperature, and the fluid is divided into boiling and non-boiling cases. For the non-boiling case, the temperature in the contact region is approximately two-thirds of the maximum temperature. Therefore, based on the model of Hahn [84], the workpiece–grain particle energy distribution ratio, R_{ws}, can be obtained as follows:

$$R_{\mathrm{ws}}=\frac{q_{\mathrm{w}}}{q_{\mathrm{w}}+q_{\mathrm{s}}}=\left[1+\frac{k_{\mathrm{g}}}{\sqrt{r_0 v_{\mathrm{s}}(k\rho c)_{\mathrm{w}}}}\right]^{-1}. \tag{21}$$

R_{ws} depends on the thermal conductivity of the abrasive particles k_{g}, the thermal properties of the workpiece $\beta_{\mathrm{w}}=\sqrt{(k\rho c)_{\mathrm{w}}}$, the rotational speed of the grinding wheel v_{s}, and the radius of the particles to wear r_0. The total wear area increases with the wear of the grinding wheel. Therefore, the radius of wear will also increase as the grinding wheel is used.

In 2018, Guo [87] analyzed the temperature in profile grinding theoretically and experimentally. As shown in Fig. 11, during the grinding process with an integral grinding wheel, the closed area between the grinding wheel and the workpiece (i.e., between B and E) makes it difficult for the coolant to penetrate, preventing effectively cooling. Therefore, most of the grinding heat is carried away by the workpiece and the grinding wheel. The high temperature in the grinding contact arc area causes the coolant to enter a film boiling state, losing its cooling capability. Therefore, the proportion of grinding heat removed by the coolant is assumed to be $R_{\mathrm{f}}=0$.

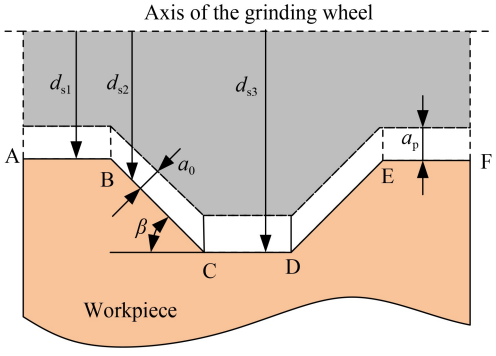

Fig. 11 Schematic of molded grinding process.

Subtracting the heat carried away by the chips, the ratio of energy transferred to the workpiece is as follows [84,87]:

$$\begin{aligned}R_{\mathrm{w}}&=R_{\mathrm{wg}}(1-R_{\mathrm{ch}})\\&\approx\left(1-\frac{6}{e_z}\right)\left[1+\frac{k_{\mathrm{g}}}{(r_0\nu_{\mathrm{c}})^{1/2}(k\rho c)_{\mathrm{w}}^{1/2}}\right]^{-1}.\end{aligned} \tag{22}$$

Rowe [84] proposed an energy distribution ratio model for surface grinding based on the contact between the workpiece and the abrasive grits, combined with the heat transfer coefficient. The schematic of the abrasive grain grinding process is shown in Fig. 12. During the grinding process, the wear planes of the abrasive grains generate heat, which is partly transferred to the workpiece and partly to the abrasive grains. Rowe correlated the theoretical model for the predicted distribution ratio with experimental results, which led to the development of an effective model applicable to cubic boron nitride (CBN) and aluminum oxide abrasives. Based on the solution provided by the circular heat-source model for a semi-infinite body, as shown in Fig. 13(a), the heat transfer coefficient of the workpiece, h_{w}, was obtained.

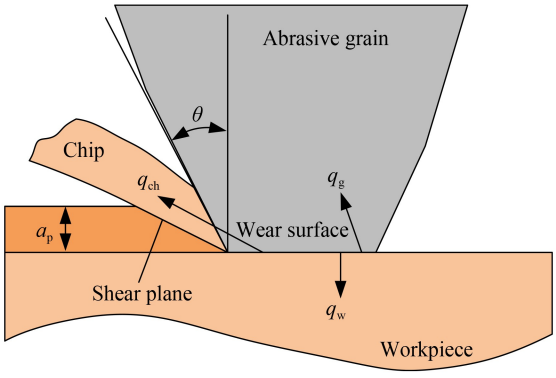

Fig. 12 Generation and transfer of heat in the plane of contact between abrasive grain and workpiece.

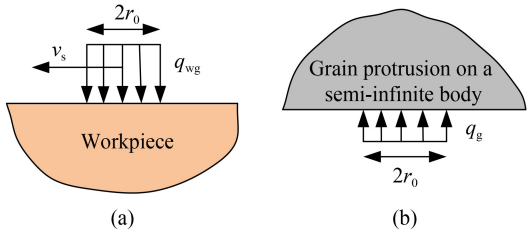

Fig. 13 (a) Modeling of the workpiece temperature rise under a grain. (b) Grain modeled as a stationary semi-infinite body.

$$h_{\mathrm{w}}=\frac{(k\rho c)_{\mathrm{w}}^{1/2}v_{\mathrm{s}}^{1/2}}{0.974r_0^{1/2}}. \tag{23}$$

As shown in Fig. 13(b), the abrasive grain is assumed to be a stationary object that is continuously subjected to a steady circular heat flux during grinding. The abrasive grain is treated as an infinitesimal protrusion on a semi-infinite object. Based on this model, the heat transfer coefficient h_{g} of the abrasive grain can be determined.

$$h_{\mathrm{g}}=\frac{k_{\mathrm{g}}}{2r_0\tau}\left[\frac{1}{\pi^{1/2}}-\mathrm{ierfc}\left(\frac{1}{2\tau}\right)\right], \tag{24}$$

where the time constant $\tau=(\alpha_{\mathrm{g}}l_{\mathrm{c}}/r_0^2v_{\mathrm{s}})^{1/2}$.

By incorporating the two heat transfer coefficients into the transient EDC model, the proportion of energy transferred to the workpiece material at the modified transient moment can be obtained as follows:

$$\begin{aligned} R_{\mathrm{w}} =&(1-R_{\mathrm{ch}})\frac{1}{1+q_{\mathrm{g}}/q_{\mathrm{wg}}}\\ =&(1-R_{\mathrm{ch}})\frac{1}{1+h_{\mathrm{g}}/h_{\mathrm{wg}}}\\ \approx&\left(1-\frac{6}{e_{\mathrm{s}}}\right)\left[1+\frac{0.974k_{\mathrm{g}}}{(r_0\nu_{\mathrm{s}})^{1/2}(k\rho c)_{\mathrm{w}}^{1/2}}\frac{1}{\Phi(\tau)}\right]^{-1}. \end{aligned} \tag{25}$$

$$\begin{aligned} \phi(\tau) =&1+\frac{1}{6\tau^2}+\frac{4\tau}{3\sqrt{\pi}}\\ &\cdot\left\{1-\left[\exp\left(\frac{1}{4\tau^2}\right)\right]^{-1}\left(1+\frac{1}{4\tau^2}\right)\right\}\\ &-\operatorname{erf}\left(\frac{1}{2\tau}\right)\left(1+\frac{1}{6\tau^2}\right). \end{aligned} \tag{26}$$

The heat transfer coefficient of the abrasive grain, $h_{\mathrm{g}} = k_{\mathrm{g}}/r_0$, and the time constant τ approaches infinity when the heat transfer reaches a steady state. At this point, in the steady state, the proportion of energy transferred to the workpiece material in the closed region between point B and point E is as follows:

$$R_{\mathrm{w(BE)}} = \left(1-\frac{6}{e_{\mathrm{s}}}\right)\cdot\left[1+\frac{0.974k_g}{(r_0v_{\mathrm{s}})^{1/2}(k\rho c)_{\mathrm{w}}^{1/2}}\right]^{-1}. \tag{27}$$

In their model of abrasive grain and workpiece contact, as shown in Fig. 14, Li and Zhao [91] indicated that the nominal contact area between the grinding wheel and the workpiece is denoted by A, while the actual contact area is A_{R}. According to the linearized model, the energy E_{w} entering the workpiece per unit of time due to thermal convection is as follows:

$$E_{\mathrm{w}} = \frac{(c_{\mathrm{p}})_{\mathrm{w}}\theta_{\mathrm{m}}}{2}\cdot(v_{\mathrm{w}}b_{\mathrm{s}}\bar{a}_{\mathrm{p}})_{\mathrm{w}} = \frac{\theta_{\mathrm{m}}b_{\mathrm{s}}}{2}\cdot\left[2(k\rho c_{\mathrm{p}})_{\mathrm{w}}v_{\mathrm{w}}l_{\mathrm{c}}\right]^{1/2}, \tag{28}$$

where c_{p} denotes the mass constant pressure specific heat capacity, θ_{m} is the temperature, b_{s} is the grinding width, a_{p} is the grinding depth, and $(k\rho c_{\mathrm{p}})_{\mathrm{w}}$ is related to the thermal properties of the workpiece.

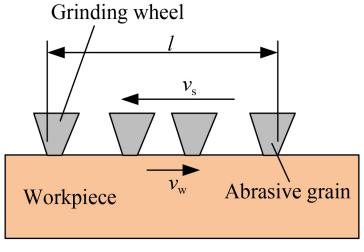

Fig. 14 Contact of the grinding wheel with the workpiece.

The energy E_{s} entering the grinding wheel per unit time due to thermal convection is as follows:

$$\begin{aligned} E_{\mathrm{s}} =&\frac{(c_{\mathrm{p}})_{\mathrm{s}}\theta_{\mathrm{m}}}{2}\cdot\left(v_{\mathrm{s}}\frac{A_{\mathrm{R}}}{A}\cdot b\cdot\bar{a}_{\mathrm{p}}\right)\\ =&\frac{1}{2}\theta_{\mathrm{m}}b\left[2(k\rho c_{\rho})_{\mathrm{s}}\cdot v_{\mathrm{s}}\cdot\frac{A_{\mathrm{R}}}{A}l\right]^{1/2}. \end{aligned} \tag{29}$$

The resulting EDC coefficients are presented as

$$R = \frac{E_{\mathrm{w}}}{E_{\mathrm{w}}+E_{\mathrm{s}}} = \frac{1}{\left[1+\frac{(k\rho c_{\mathrm{p}})_{\mathrm{s}}}{(k\rho c_{\mathrm{p}})_{\mathrm{w}}}\frac{v_{\mathrm{s}}}{v_{\mathrm{w}}}\left(\frac{A_{\mathrm{R}}}{A}\right)_{\mathrm{s}}\right]^{1/2}}. \tag{30}$$

For flat grinding, $(v_{\mathrm{w}}/v_{\mathrm{s}})(A_{\mathrm{R}}/A)_{\mathrm{s}} \approx 1$. Thus, the EDC of energy distribution under flat grinding conditions is computed as follows:

$$R = \frac{1}{\left[1+(k\rho c_{\mathrm{p}})_s/(k\rho c_{\mathrm{p}})_{\mathrm{w}}\right]^{1/2}}. \tag{31}$$

When the effect of the coolant is considered, the energy transferred to the grinding wheel is equal to the sum of the energy imparted to the abrasive particles and the energy transferred to the coolant on the surface of the wheel. Therefore, under wet grinding conditions, the proportion of energy transferred to the grinding wheel is as follows [92]:

$$\begin{aligned} R =&\frac{R_{\mathrm{w}}}{R_{\mathrm{w}}+R_{\mathrm{s}}} = \frac{E_{\mathrm{w}}}{E_{\mathrm{w}}+E_{\mathrm{s}}}\\ =&\left[1+\sqrt{\frac{(k\rho c_{\mathrm{p}})_{\mathrm{s}}}{(k\rho c_{\mathrm{p}})_{\mathrm{w}}}\frac{v_{\mathrm{s}}}{v_{\mathrm{w}}}\left(\frac{A_{\mathrm{R}}}{A}\right)_{\mathrm{s}}}+\sqrt{\frac{(k\rho c_{\mathrm{p}})_{\mathrm{f}}}{(k\rho c_{\mathrm{p}})_{\mathrm{w}}}\frac{v_{\mathrm{s}}}{v_{\mathrm{w}}}}\right]^{-1}, \end{aligned} \tag{32}$$

where $(k\rho c_{\mathrm{p}})_{\mathrm{f}}$ is related to the coolant and $(k\rho c_{\mathrm{p}})_{\mathrm{s}}$ is related to the abrasive grains on the surface of the grinding wheel.

2.4.3 Considering the surface temperature of the workpiece

In the grinding process, the surface temperature rise of the workpiece can be measured to calculate the amount of heat absorbed by the workpiece [93,94]. This measurement serves as the basis for calculating the proportion of energy distribution during the grinding process.

For example, Rowe [84] obtained the energy distribution ratio by relating the maximum background temperature to the heat entering the workpiece based on the Jaeger solution for a sliding heat source and corrections for different flux distributions.

$$R_{\mathrm{w}} = \frac{\pi}{C}b\cdot\sqrt{(k\rho c)_{\mathrm{w}}v_{\mathrm{w}}l_{\mathrm{e}}}\cdot\frac{\theta_{\mathrm{m}}}{q_{\mathrm{t}}}, \tag{33}$$

where θ_{m} is the maximum background temperature. The value of C depends on the shape of the heat source and the value of the Péclet number.

When the Péclet number is high, the C value is shown in Table 2.

Table 2 Value of coefficient C

Heat distribution	Coefficient C	Position of maximum temperature X/L [84]
Uniform	3.540	1
Triangular	3.304	0

In 2011, Hadad et al. [95] investigated the temperature and energy distribution during MQL grinding. The experiments were conducted using CBN and Al_2O_3 grinding wheels. As shown in Fig. 15, the experiment treats the contact zone as a strip heat source of length l_c, which moves along the surface of the workpiece with a velocity v_{ft} to calculate the temperature of the contact zone.

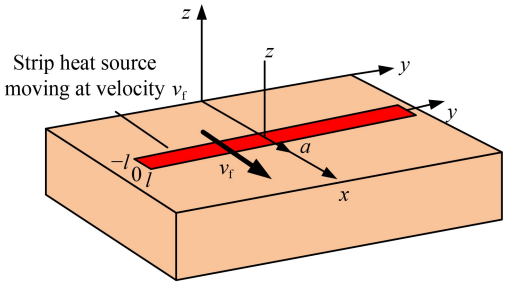

Fig. 15 Moving band heat source on the semi-infinite surface with a length of $l_c = 2l$ [95].

An assumption is that the contact zone heat is transferred to the workpiece, grinding wheel, chips and coolant during the grinding process (Fig. 16). Based on the assumption of a triangular heat-source distribution in the x–z plane, the temperature rise of the workpiece is as follows:

$$T_0(x,z) = \frac{q_w}{\pi k_w}\int_{-l_c/2}^{l_c/2} \exp\left[-V_{ft}(x-a)/(2\alpha)\right] \cdot K_0\left\{\frac{V_{ft}}{2\alpha_w}\left[(x-a)^2+z^2\right]^{1/2}\right\} f(a)\mathrm{d}a, \quad (34)$$

where $f(a) = 1 + 2a/l_c$ is the triangular heat-source distribution and K_0 is the Type II zero-order modified Bessel function.

The maximum temperature rise T_{max} of the workpiece during grinding was measured in the experiment, and the total energy input can be calculated by measuring the tangential grinding force as q_t as shown below:

$$q_t = \frac{F_t V_c}{b l_c}, \quad (35)$$

where F_t is the tangential grinding force, b is the workpiece width, and l_c is the actual grinding contact length.

Therefore, calculating the energy distribution of the workpiece by evaluating the maximum temperature rise T_{max} is possible.

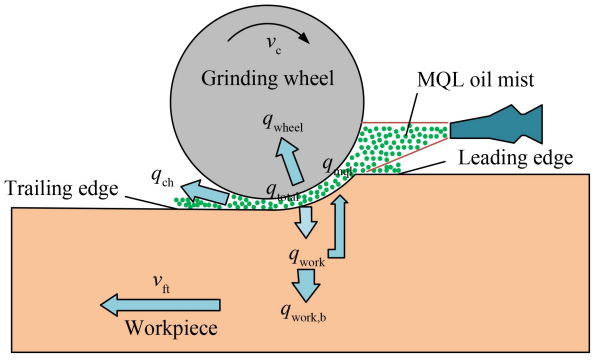

Fig. 16 Schematic of heat flow distribution in the grinding wheel zone [95].

$$T_{max} = \frac{\beta q_w \alpha_w^{1/2} l_c^{1/2}}{k_w V_{ft}^{1/2}}, \quad (36)$$

where k_w denotes the thermal conductivity of the workpiece, α_w is the heat diffusivity of the workpiece, and β denotes a constant related to the shape of the heat source ($\beta = 1.06$ for triangularly distributed heat sources).

In 2021, Peng et al. [96] investigated the height of the energy distribution ratio and its changing law by high-speed grinding of nickel-based high-temperature alloys. As shown in Fig. 17, for high-speed grinding, an inclined triangular heat-source is more appropriate, and the angle Φ between the line of motion and the plane of the belt source can also more accurately represent the amount of moving heat, the maximum grinding temperature rise T_{max} on the contact workpiece surface based on the one-dimensional conduction sliding heat-source theory can be expressed as [37,97]

$$T_{max} = C_0 \cdot \frac{q_w}{\beta_w} \cdot \sqrt{\frac{l_c}{\nu_w}}, \quad (37)$$

where C_0 is the parameter factor in the circular moving heat-source model. $\beta_w = \sqrt{(k\rho c)_w}$. For the value of C_0 [97], the shape of the heat flow density distribution during the grinding process is approximately triangular. The sliding heat-source solution gives a value of C_0 approximately equal to 1.

Therefore, the energy distribution ratio R_w to the workpiece can be simply calculated using the measured grinding surface temperature T_s:

$$\begin{cases} R_w = \dfrac{q_w}{q_t} = \dfrac{T_{max} h_w}{q_t} = \dfrac{(T_s - T_0)\cdot h_0}{q_t}, \\ h_w = \dfrac{\beta_w}{C}\sqrt{\dfrac{\nu_w}{l_c}}, \end{cases} \quad (38)$$

where T_0 is the ambient temperature. $T_0 = 20$ ℃, and h_0 is defined as the heat transfer factor, which is determined by the thermal properties of the workpiece, the speed of movement of the heat-source, and the contact geometry.

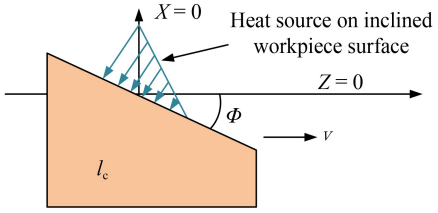

Fig. 17 Grinding contact for deep grinding is accurately represented as a heat source moving into the surface at an angle Φ.

In 2018, Ding et al. [98] investigated the temperature and energy distribution in the cylindrical grinding process under various process and thermophysical parameter conditions. They used a physical model-based approach, combined with finite element simulation and experimental validation. The research emphasized the effect of workpiece speed on energy distribution.

Temperature modeling was conducted using a moving tilted triangular strip source temperature model, based on the Jaeger model:

$$T = \frac{8\alpha_w^2 q}{\pi k l_c \nu_w^2} \cdot \int_{x\nu_w/(2\alpha_w)}^{(x-l_c)\nu/(2\alpha_w)} u \cdot \exp(-u) \cdot k_0(u)\mathrm{d}u - \frac{4\alpha_w q x}{\pi k l_c \nu_w} \cdot \int_{x\nu_w/(2\alpha_w)}^{(x-l_c)\nu/(2\alpha_w)} \exp(-u) \cdot k_0(u)\mathrm{d}u. \quad (39)$$

The model for calculating the energy distribution of the workpiece, based on the maximum temperature of the workpiece, can be expressed as follows:

$$R_w = T_{\max} \cdot \left\{ P'_{\mathrm{net}} \left[k_1 \int_{xv/(2\alpha_w)}^{(x-l_c)v/(2\alpha_w)} u^2 \cdot \exp(-u) \cdot k_0(u)\mathrm{d}u + k_2 \int_{xv/(2\alpha_w)}^{(x-l_c)v/(2\alpha_w)} u \cdot \exp(-u) \cdot k_0(u)\mathrm{d}u + k_3 \int_{xv/(2\alpha_w)}^{(x-l_c)v/(2\alpha_w)} \exp(-u) \cdot k_0(u)\mathrm{d}u \right] \right\}. \quad (40)$$

In 2003, Li and Zhao [91] stated that the heat transferred to the workpiece during the grinding process notably affects the temperature of the grinding zone and referred to the energy distribution model. In 2019, Zhang et al. [99] applied this model to the MQL grinding of Ti–6Al–4V. The density of heat flow into the workpiece during grinding is as follows:

$$q_w = \frac{q_w}{q_t} \cdot q_t = \frac{\nu_s F_t}{b l_c} \cdot R = \frac{\nu_s F_t}{b\sqrt{d_s a_p}} \cdot R. \quad (41)$$

The energy scaling factor can be expressed as shown below.

$$R = \frac{k_w \nu_w^{1/2}}{q_t \beta \alpha_w^{1/2} a_p^{1/4} d_s^{1/4}} \theta_{\max}, \quad (42)$$

where $\theta_{\max}$ is the peak rise of temperature.

2.4.4 Based on material physical parameters

Mao et al. [100] considered various factors to re-evaluate the heat distribution ratio into the workpiece. On this basis, Rowe [97] conducted a thermal analysis of efficient deep grinding to explore optimal working conditions for the process.

In this analysis, the heat in the grinding zone is assumed to flow in the following four directions: workpiece, grinding wheel, chips, and fluid. The total heat flow is as follows:

$$q_t = q_w + q_S + q_{ch} + q_f. \quad (43)$$

The heat flow to the workpiece, grinding wheel, fluid, and chips can be expressed in terms of convection/conduction factors [101]. This heat flow is related to the maximum contact temperature $T_{\text{max-c}}$ and the fluid burnout temperature T_b, while the heat of the chips q_{ch}, is related to the average temperature of the workpiece $\overline{T}$, but not to the melting temperature of the workpiece material T_w.

$$\begin{aligned} q_w &= h_w T_{\max-c}, \\ q_s &= h_s T_{\max-c}, \\ q_f &= h_f T_{\max-c}|_{T_{\text{max-c}} \leqslant T_b}, \\ q_{ch} &= h_{ch} \overline{T}. \end{aligned} \quad (44)$$

An assumption is that the heat flowing into the chip enables it to reach the critical temperature for melting; thus,

$$q_{ch} = \rho_w c_w T_w \frac{a_p v_w}{l_c}. \quad (45)$$

The heat flow into the coolant q_f requires suitable experimental data. Two main types of coolant are available: pure oil and oil-in-water emulsion. For the oil-in-water emulsion, $q_f = 0$ is assumed under boiling conditions [97]. During the grinding process, the temperature in the grinding zone is typically high and can easily reach the boiling point of the coolant. At this time, the coolant and the surface of the workpiece form an insulating layer due to vaporization, notably reducing the heat transfer between the coolant and the workpiece surface [102]. Therefore, the heat flow density transferred to the

coolant is assumed to be zero, denoted as $q_f = 0$.

Based on Hana's distribution model, the grinding wheel and the workpiece are regarded as a subsystem, and the total heat of the grinding wheel and the workpiece is $q_{ws} = q_w + q_s$. Thus, the "workpiece–grinding wheel" distribution ratio R_{ws} is defined as shown below.

$$R_{ws} = \frac{q_w}{q_w + q_s} = \left[1 + \frac{0.974k_g}{\sqrt{(k\rho c)_w r_0 v_s}}\right]^{-1}. \tag{46}$$

The following represents the heat flow into the workpiece during grinding.

$$\begin{aligned} q_w &= R_{ws}\left(q_t - q_{ch} - q_f\right) \\ &= \left[1 + \frac{0.974k_g}{\sqrt{(k\rho c)_w r_0 v_s}}\right]^{-1} \cdot \left(\frac{F_t \nu_s}{l_c b} - \rho_w c_w T_w \frac{a_p \nu_w}{l_c}\right). \end{aligned} \tag{47}$$

By substituting the above heat model of the workpiece, the proportion of energy flowing into the workpiece can be obtained.

$$R_w = \left[1 + \frac{0.974k_g}{\sqrt{(k\rho c)_w r_0 v_s}}\right]^{-1} \left(1 - \frac{\rho_w c_w T_w \dfrac{a_p \nu_w}{\sqrt{a_p d_s}}}{\dfrac{F_t \nu_s}{\sqrt{a_p d_s} b}}\right). \tag{48}$$

Based on the equation, the model fully considers several factors. By incorporating these effects, the model extends its range of applicability and has become a commonly used method for calculation.

Ramanath and Shaw [103] proposed a method to calculate the energy distribution ratio between the workpiece and the grinding wheel. As shown in Fig. 18, during a surface grinding operation, they assumed that the grinding wheel behaves as a perfect adiabatic body, with all the heat flowing into the workpiece. By applying the Jaeger solution to Fig. 18, the average working temperature over the grinding wheel–workpiece contact arc can be easily obtained.

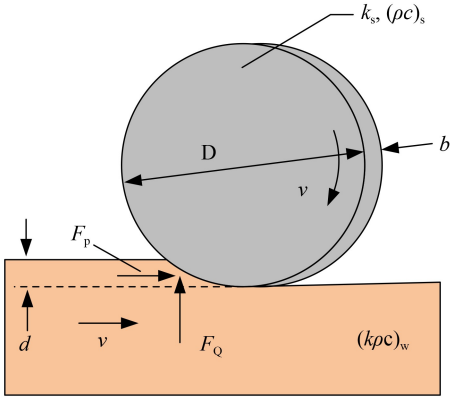

Fig. 18 Two-dimensional surface grinding operation.

Assuming that the average surface temperatures of the workpiece and the grinding wheel in the grinding zone are equal, the EDC between the workpiece and the grinding wheel is as follows:

$$R_{ws} = \left[1 + \sqrt{\frac{(k\rho c)_g}{(k\rho c)_w}}\right]^{-1}. \tag{49}$$

However, the model applies only to the energy distribution between the grinding wheel and the workpiece. The model does not involve the speed and grinding parameters of the grinding wheel, nor does it consider changes in the temperature gradient or the grain shape of the wheel. Therefore, this model can only provide an approximate energy distribution ratio.

Kohli et al. [104] investigated the energy distribution of workpieces during grinding with aluminum oxide and CBN grinding wheels. The grinding temperature is typically calculated using either a rectangular (uniform) heat flow density distribution or a triangular heat flow density distribution. While results from both models show only a small difference, the internal temperature distribution remains largely the same. As shown in Fig. 19, the triangular heat-source mode was found to be highly relevant after the study because it provides better correlation between the measured and calculated temperatures.

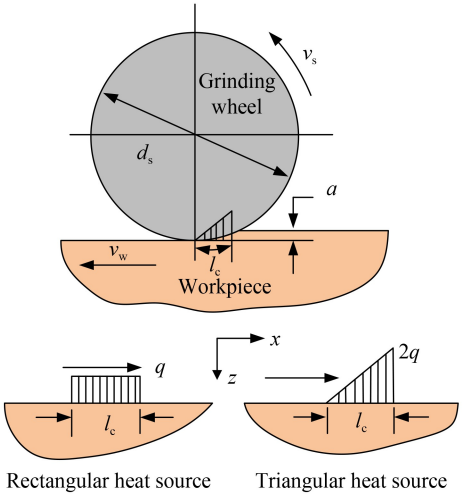

Fig. 19 Illustration of plunge grinding and heat flux distributions.

The energy input to the workpiece was calculated analytically by matching the calculated temperature with the measured temperature. The energy distribution was then obtained by dividing the input workpiece energy by the measured net grinding

energy. Additionally, the effective number of grains was incorporated into the grinding energy distribution model. By equalizing the maximum temperatures of the workpiece and the abrasive grains at their interfaces, the energy distribution of the workpiece for the triangular heat-source distribution was obtained as follows:

$$R_{\mathrm{w}}=\left[1+1.06\sqrt{\frac{\pi(k\rho c)_{\mathrm{g}}v_{\mathrm{s}}}{2(k\rho c)_{\mathrm{w}}v_{\mathrm{w}}}}f(\zeta)A_0G_{\mathrm{a}}\right]^{-1}, \tag{50}$$

where G_{a} is the number of active abrasive grains per unit area on the surface of the grinding wheel, A_0 is the average single-grain workpiece contact area corresponding to the cross-sectional area of the cone, and the value of A_0 corresponding to the measured value of R_{w} can be obtained by calculation. The function $f(\zeta)$ considers that the cross-sectional area of the abrasive grain is larger than the contact area between the abrasive grain and the workpiece.

2.4.5 Slicing multiple energy distribution subsystems

In 2006, Jin and Stephenson [105] proposed a comprehensive method to analyze the energy distribution ratio R_{w} of the workpiece, establishing the energy distribution relationship between the workpiece, abrasive, abrasive fluid, and grinding chip as follows:

$$R_{\mathrm{w}}=\frac{q_{\mathrm{w}}}{q_{\mathrm{t}}}=\frac{R_{\mathrm{ws}}\cdot R_{\mathrm{wch}}}{R_{\mathrm{ws}}+R_{\mathrm{wch}}-R_{\mathrm{ws}}\cdot R_{\mathrm{wch}}\left(1-\frac{h_{\mathrm{f}}}{h_{\mathrm{w}}}\right)}, \tag{51}$$

where h_{f} is the convection coefficient of the coolant.

$$\begin{aligned}R_{\mathrm{ws}}&=\frac{q_{\mathrm{w}}}{q_{\mathrm{w}}+q_{\mathrm{s}}}=\frac{h_{\mathrm{w}}}{h_{\mathrm{w}}+h_{\mathrm{s}}},\\ R_{\mathrm{wch}}&=\frac{q_{\mathrm{w}}}{q_{\mathrm{w}}+q_{\mathrm{ch}}}=\frac{h_{\mathrm{w}}}{h_{\mathrm{w}}+h_{\mathrm{ch}}},\end{aligned} \tag{52}$$

where h_{ch} is defined as the heat transfer coefficient of the chip.

In 2012, Hadad and Sadeghi [106] investigated the thermal analysis of the MQL grinding process. They introduced a new method for calculating the grinding temperature and workpiece energy distribution during the MQL grinding process by examining the grinding wheel and workpiece as a system.

In the model (Fig. 20), heat is assumed to be generated at the grinding wheel–workpiece interface (global scale) and within the workpiece. The two mechanisms of heat generation are friction and plastic deformation. Three heat-source locations are available in the grinding process: the contact surface between the abrasive grit and the workpiece, the contact surface between the abrasive grit and the chip, and the shear surface between the workpiece and the chip.

As shown in Fig. 21, the total heat flux q_{t} generated by grinding is instantaneously transferred to the chip

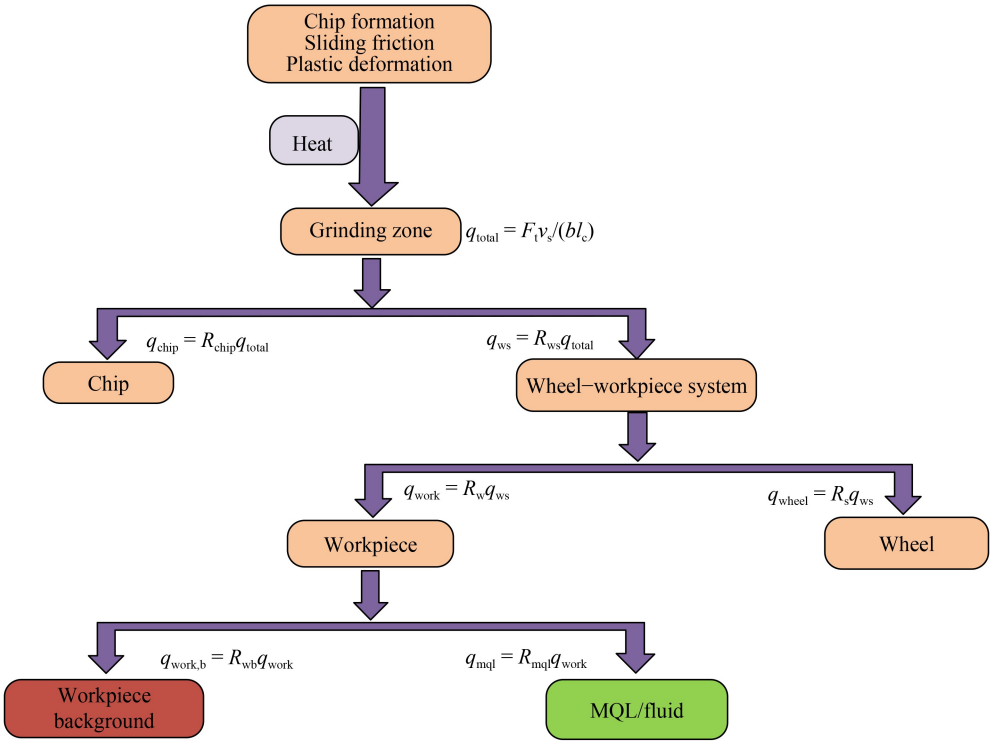

Fig. 20 Schematic of heat flux partitioning during grinding process [106].

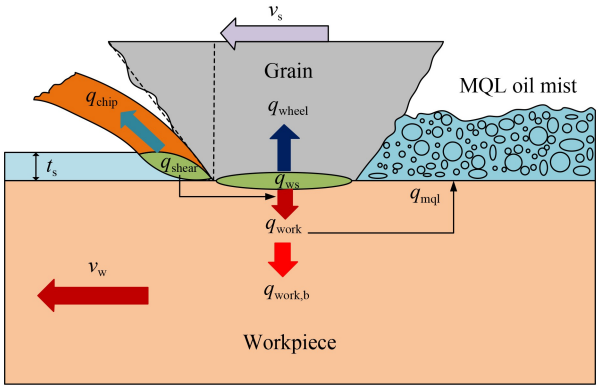

Fig. 21 Heat transfer in grain–workpiece interface [106].

and to the system of the workpiece and grinding wheel.

$$q_t = q_c + q_{w\text{-}g}. \tag{53}$$

Within the system of workpieces and grinding wheels, heat flows into the workpiece and the grinding wheel, where $q_{w\text{-}g} = q_w + q_g$. The heat inflow into the workpiece, removed by the coolant, is subtracted, leaving the actual heat transferred to the workpiece. For the circular contact, the speed between grinding wheel grain and workpiece is assumed to be consistent with the grinding wheel speed. By considering the heat distribution ratio, the proportion of heat transferred to the workpiece can be obtained as follows:

$$R_w = \left[1 + \frac{0.974k_g}{\sqrt{(k\rho c)_w \cdot (l_{wf}/2) \cdot V_c}} \frac{1}{F}\right]^{-1}, \tag{54}$$

where F is the transient function, and Black gives an approximate computational model F. The τ is modeled as a dimensionless time and l_{wf} is the average diameter of the wear plane.

$$\begin{cases} F = 1 - \exp\left(-\dfrac{\tau}{2}\right), \\ \tau = \left(\dfrac{4\alpha_g l_c}{l_{wf}^2 V_c}\right)^{1/2}. \end{cases} \tag{55}$$

In 2012, Zhu et al. [107] indicated that existing grinding temperature models generally assume that the effective contact radius of the abrasive grain is a constant, resulting in poor prediction accuracy. Aiming to address the modeling accuracy, an enhanced model that considers the geometry and distribution of abrasive grains is proposed. As shown in Fig. 22, a single abrasive grain is regarded as a cone, providing the heat diffusion coefficient of the grain as shown below.

$$\alpha_g = \frac{k_g}{\rho_g c_g}. \tag{56}$$

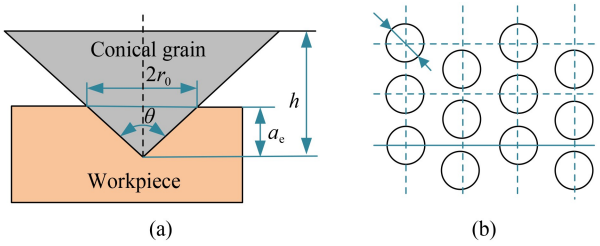

Fig. 22 (a) Schematic of conical grain. (b) Orderly arrangement of cross-array model [107].

The effective contact radius of the abrasive grains varies considerably depending on the depth of cut and the cone angle of the abrasive grains. Therefore, treating it as a constant for estimation is unreasonable and introduces some error. Based on the model shown in Fig. 22, the calculation model for the effective contour radius, considering different depths of cut and variable taper angles, is $r_0 = a_p \cdot \tan(\theta/2)$, which, when incorporated into the existing EDC, yields a more reasonable model of R_w.

$$R_{ws} = \left[1 + \frac{0.974k_g}{\beta_w \sqrt{a_p \cdot \tan(\theta/2) \cdot \nu_s}} \cdot \frac{1}{F}\right]^{-1}. \tag{57}$$

In 2016, Jin et al. [108] divided the heat distribution in the grinding zone into multiple systems, derived the EDC for each system based on the existing models. They then derived the EDC model for the workpiece based on existing models. Previous grinding models mainly focused on plane grinding, with the complexity of gear grinding, the point-source temperature rise solution was further developed. As shown in Fig. 23, this model accounts for the non-uniform heat sources occurring within the grinding zone for three-dimensional involute shapes. Thus, the model allows for the calculation of grinding

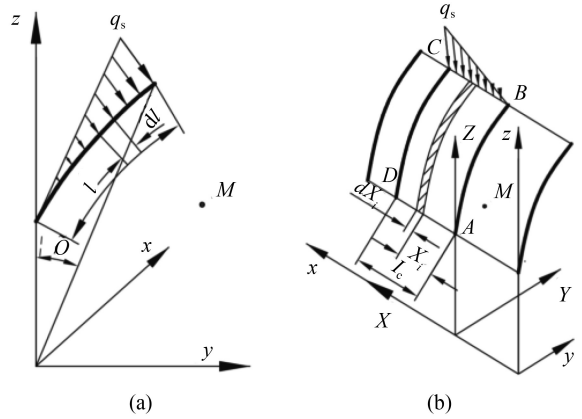

Fig. 23 Distribution of the heat flux density at the three-dimensional involute shape grinding zone (a) along the tooth profiles and (b) along the contact length [108].

temperatures and an analysis of how the energy distribution ratio of the workpiece changes along the gear tooth profiles under different grinding conditions.

The energy distribution ratio R_{ws} between the workpiece and the grinding wheel was obtained based on Hahn's model, and the energy distribution ratio R_{wch} between the workpiece and the chips was obtained based on Stephenson and Jin's model.

$$R_{wch}(\xi_i)=\frac{h_w(\xi_i)}{h_w(\xi_i)+h_{ch}(\xi_i)}=\frac{1}{1+0.753\sqrt{\dfrac{\nu_s(\xi_i)t_a(\xi_i)}{\alpha_w\gamma}}}, \tag{58}$$

where $\alpha_w=k_w/(\rho_w c_w)$ is the thermal diffusivity of the abrasive chips, γ is the shear strain in the chip formation zone, and $t_a(\xi_i)$ is the undeformed chip thickness.

Combining the above sub-models, the EDC for the workpiece can be derived as follows:

$$R_w(\xi_i)=\frac{q_w}{q_t}=R_{ws}(\xi_i)R_{wch}(\xi_i)\cdot\left\{R_{ws}(\xi_i)+R_{wch}(\xi_i)-R_{ws}(\xi_i)R_{wch}(\xi_i)\cdot\left[1-\frac{h_f(\xi_i)}{h_w(\xi_i)}\right]\right\}^{-1}, \tag{59}$$

where ξ is the roll angle.

2.4.6 Considering convective heat transfer

In 2002, Jin et al. [101] investigated the combustion threshold for efficient deep grinding. Based on thermal modeling of deep grinding conditions, they derived the theoretical expression for the workpiece burning threshold by comprehensively considering the grinding parameters, grinding wheel conditions, thermal properties of the workpiece and abrasive grains, as well as the convective heat dissipation of the grinding coolant and chips.

On this basis, Yang et al. [109], in their study of nanoparticle spray cooling, found that nanofluids play a major role in heat dissipation within the grinding zone, with the convective heat transfer of the nanofluid carrying away most of the heat. They developed a mathematical model for R_w by calculating the CHTC of the grinding wheel, workpiece, coolant, and chips, without the need to directly measure the grinding zone temperature.

Rowe [110] improved the thermal model by considering the effect of convective heat transfer in different states of the coolant on the energy distribution. He developed a division expression that distinguishes between the upper and lower boundaries, enhancing the modeling of heat flow distribution between the grinding wheel and the workpiece. In wet grinding, if the liquid film boiling temperature is exceeded, then the coolant no longer serves as an effective heat sink in the grinding zone.

In the calculation process, as shown in Fig. 24, the energy distribution ratio between the grinding wheel and the workpiece is calculated based on a simple two-slider model. However, after further consideration, the chips and the coolant, as heat dissipation components, have no substantial effects on the calculation of R.

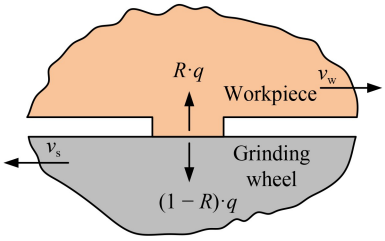

Fig. 24 Energy distribution between the grinding wheel and the workpiece.

The grinding wheel and the workpiece can be regarded as two sliders. After considering the density and nature of the heat flow in the grinding wheel and the workpiece, an assumption is that both are affected by the sliding heat source. Considering these factors, the energy ratio of the workpiece can be determined.

$$R_{ws}=\frac{1}{1+\sqrt{\dfrac{v_s}{v_w}\dfrac{(k\rho c)_s}{(k\rho c)_w}}}. \tag{60}$$

If the energy from the convection of chips and coolant is considered, then the predicted distribution ratio is reduced and the EDC can be corrected as shown below.

$$R=R'\left(1-\frac{e_{cc}+e_{cf}}{e_c}\right). \tag{61}$$

Typical values of e_{cc} are 6 J/mm^3, and the value of e_{cf} is 0 when fluid boiling occurs, leading to an increasingly substantial effect of chips at relatively low specific energies.

$$R=R'\left(1-\frac{6}{e_c}\right). \tag{62}$$

In 2022, Zheng et al. [111] considered the role of coolant in the grinding process and established an improved external wet grinding temperature model that accounts for the lubricating effect of the coolant, building on previous models. The model determines the EDC of the workpiece through the relationship between the EDC of different subsystems. As shown in Fig. 25, the schematic illustrates cylindrical

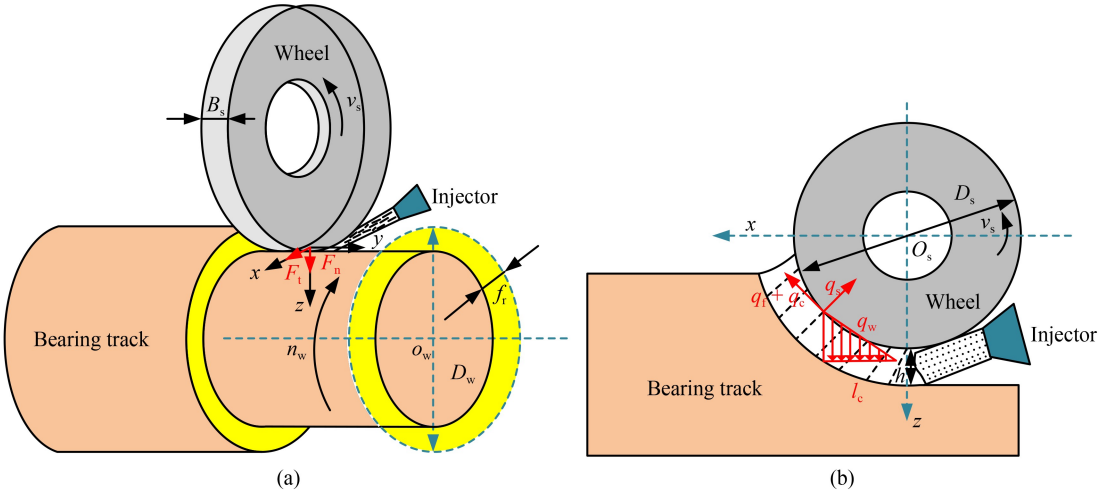

Fig. 25 Cylindrical grinding model. (a) Schematic of cylindrical grinding. (b) Heat flux distribution diagram [111].

grinding and the heat distribution within the grinding zone.

The energy ratio R_w flowing into the workpiece can be calculated by the following relation [108].

$$R_w = \left[\frac{1}{R_{ws}} + \frac{1}{R_{wch}} - \left(1 - \frac{h_f}{h_w}\right)\right]^{-1}, \tag{63}$$

where h_f is the CHTC of the coolant, h_w is the CHTC of the workpiece, and R_{ws} and R_{wch} are the energy distribution ratios of the workpiece–grinding wheel and the workpiece–chip, respectively.

$$R_{ws} = \frac{1}{1 + \dfrac{0.974k_s}{\beta_w\sqrt{r_0\nu_s}}\left[1 - \exp\left(-\frac{\tau}{2}\right)\right]^{-1}}, \tag{64}$$

$$R_{wch} = \frac{1.328\sqrt{\alpha_w\gamma/(\nu_s a_{gmax})}}{1 + 1.328\sqrt{\alpha_w\gamma/(\nu_s a_{gmax})}}, \tag{65}$$

where the dimensionless number τ is given by $\tau = \left[k_s^{1/2} l_c (\rho_s c_s)^{-1/2}/(r_0^2\nu_s)\right]^{1/2}$, k_s is the thermal conductivity of the grinding wheel, ρ_s is the density of the grinding wheel, and c_s is the specific heat of the grinding wheel. The shear strain is defined as $\gamma = \cos\theta/[\sin\varphi \cdot \cos(\varphi + \theta)]$, where θ and φ are the half of the grinding tip angle and the shear angle, respectively, and a_{gmax} is the maximum undeformed chip thickness.

2.4.7 Grinding wheel and fluid composite as a whole

In 2000, Guo and Malkin [88] proposed a quantitative method for calculating grinding temperature and workpiece energy distribution. Aiming to analyze heat transfer during the grinding process, they approximated the heat transfer problem in two dimensions by considering straight-face plunge grinding, as shown in Fig. 26. The contact between the grinding wheel, fluid, and workpiece was simplified as two planar contact surfaces, and the heat source was modeled as a suitable rectangular heat source.

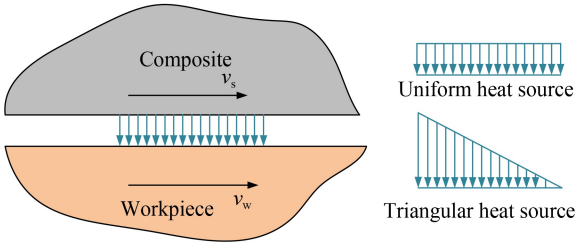

Fig. 26 Illustration of temperature-matching model.

This method of estimating energy distribution is based on matching the temperature in the grinding area. Therefore, the grinding wheel and fluid are considered as a composite material. Assuming that the energy distributed to the workpiece along the grinding zone remains constant, the energy distribution in the workpiece can be calculated as follows:

$$R = \left[1 + \sqrt{\frac{(k\rho c\nu)_c}{(k\rho c\nu)_w}}\right]^{-1}, \tag{66}$$

where k is the thermal conductivity and ρ_c is the volume-specific heat. The subscript c represents the composite and w represents the workpiece.

The thermal properties of the wheel–liquid composites are unknown and the location of the maximum temperature varies. Thus, this relatively simple model can only be used for qualitative analysis of the energy distribution.

Lavine [112] presented a simple analytical model for heat transfer between the grinding wheel, workpiece surface, and coolant, predicting the proportion of energy entering the workpiece. As shown in Fig. 27, the grinding zone is modeled as a two-dimensional region. Assuming that the coolant fills the thermal boundary layer pores and remains stationary relative to the grinding wheel, the grinding wheel is considered as a composite material comprising coolant and abrasive grains, with their combined properties determining the overall properties of the wheel.

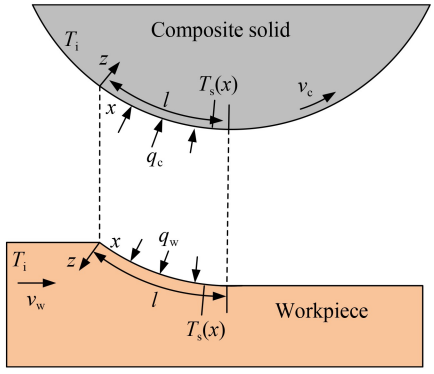

Fig. 27 Model of the grinding zone.

The total heat generated is divided into two parts: the heat conducted to the workpiece and the heat entering the complex comprising the grinding wheel and the fluid. The proportion of energy transferred to the workpiece is then given by the following:

$$R = \left[1 + \frac{\sqrt{(k\rho c_{\mathrm{P}} V)_{\mathrm{c}}}}{\sqrt{(k\rho c_{\mathrm{P}} V)_{\mathrm{w}}}}\right]^{-1}. \tag{67}$$

The ratio of the actual contact area of the grinding wheel to the nominal contact area of the workpiece, namely A_{R}/A, is much less than 1 for the grinding wheel and equal to 1 for the liquid film. The proportion of energy allocated to the workpiece is then calculated as follows:

$$R_{\mathrm{w}} = \left[1 + \sqrt{\frac{(k\rho c)_{\mathrm{g}} \nu_{\mathrm{s}} A_{\mathrm{R}}}{(k\rho c)_{\mathrm{w}} \nu_{\mathrm{w}} A}} + \sqrt{\frac{(k\rho c)_{\mathrm{f}} \nu_{\mathrm{s}}}{(k\rho c)_{\mathrm{w}} \nu_{\mathrm{w}}}}\right]^{-1}. \tag{68}$$

Kim et al. [113] investigated the heat flow density distribution and energy distribution in the workpiece during creep feed grinding. On this basis, they measured the surface temperature of the workpiece and used inverse analysis to determine the energy distribution value. These results were the compared with those calculated using the moving heat-source theory. The analysis was conducted separately under different working conditions for down grinding and up grinding (Fig. 28).

The energy distribution in the workpiece can be

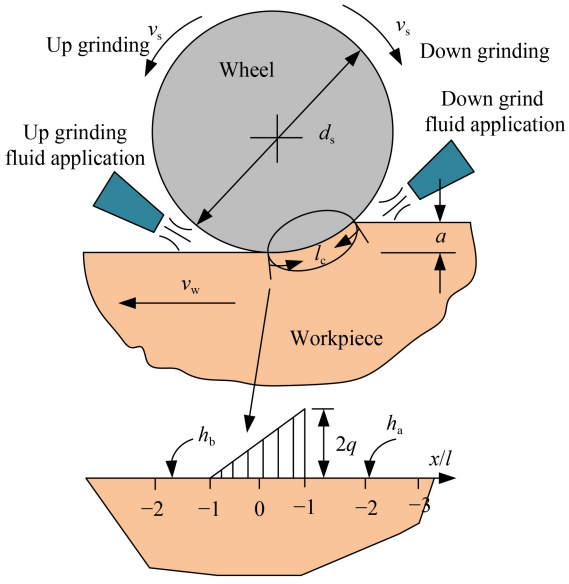

Fig. 28 Illustration of up and down grinding and thermal model.

easily obtained by modeling the grinding zone as a band heat source moving at the wheel speed along the workpiece surface. This approach involves calculating the maximum surface temperature at the interface on one side of the composite and assuming a sufficiently large Péclet number, such that heat conduction in the direction of motion can be neglected.

$$\varepsilon = \left[1 + \sqrt{\frac{(k\rho c)_{\mathrm{c}} v_{\mathrm{s}}}{(k\rho c)_{\mathrm{w}} v_{\mathrm{w}}}}\right]^{-1}. \tag{69}$$

Takazawa [114] considered the thermal parameters of the grinding wheel and the workpiece, treating them as a composite heat conductor. The grinding process was modeled as two contact heat conductors moving at different speeds. A one-dimensional heat conduction model was then used to calculate the percentage of heat transferred to the workpiece as follows:

$$R_{\mathrm{w}} = \begin{cases} \dfrac{1}{1 + \sqrt{\dfrac{(k\rho c)_{\mathrm{s}}}{(k\rho c)_{\mathrm{w}}} \cdot \dfrac{\nu_{\mathrm{s}}}{\nu_{\mathrm{w}}}}} & (Pe > 5), \\ \dfrac{1}{1 + 0.6\dfrac{\sqrt{(k\rho c)_{\mathrm{s}}}}{(\rho c)_{\mathrm{w}}} \cdot \dfrac{f}{\nu_{\mathrm{w}}}} & (Pe < 5). \end{cases} \tag{70}$$

In 2017, Yin and Marinescu [115] modeled the grinding zone as a heat source, assuming that most of the heat is transferred to the workpiece, while the remaining energy is carried away by the grinding wheel, abrasive fluid, and chips. Based on Lavin's model [116], they assumed that the grinding wheel is a composite of coolant and wheel, with the heat entering the wheel denoted as q_{s}.

$$q_s = \frac{T_m b}{2}\sqrt{2(k\rho c)_s \cdot v_s \frac{A_R}{A} l_c}, \quad (71)$$

where T_w is the melting point of the workpiece and A_R is the contact area of the abrasive grains.

Based on Malkin's study, the energy imparted to the abrasive chips can be calculated using the specific energy of the abrasive chips.

$$q_c = \frac{e_c \cdot MRR}{b \cdot l_c} = \frac{\rho_w c_w T_m b\, a_p v_w}{b \cdot \sqrt{a_p d_s}} = \frac{\rho_w c_w T_m a_p v_w}{\sqrt{a_p d_s}}, \quad (72)$$

where d_s is the diameter of the grinding wheel. MRR is the material removal rate.

An assumption is that most of the heat is transferred to the workpiece and the coolant. Therefore, the heat involved in the heat transfer process comprises the heat flow density q_w of the workpiece and the convective heat flow density q_f of the coolant. The energy distribution can then be expressed as follows:

$$R_{wf} = \frac{q_w + q_f}{q_t} = 1 - \frac{q_c + q_s}{q_t} = 1 - \frac{1}{\dfrac{F_t V_s}{b\sqrt{a_p d_s}}} \cdot \left[\frac{\rho_w c_w T_m a_p V_w}{\sqrt{a_p d_s}} + \frac{T_m b}{2}\sqrt{2(k\rho c)_s V_s \beta \sqrt{a_p d_s}}\right]. \quad (73)$$

This energy distribution equation considers the effects of workpiece feed rate, depth of cut, equivalent grinding wheel diameter, tangential grinding force, and the physical and thermal properties of the grinding wheel and the workpiece on R_{wf}. This equation also considers the cooling effect of the coolant, and the results for the tangential grinding force F_t reflect the effect of the coolant.

2.4.8 Considering heat source tilt angle

In 2001, Jin et al. [117] conducted a thermal study of high-efficiency deep grinding (HEDG) investigated the relationship between workpiece energy distribution and grinding parameters. They developed an analytical model for deep grinding that considered the influence of the inclination angle of the heat-source plane on its direction of motion. Under HEDG conditions with a large Péclet number, the inclination angle substantially affects the temperature of the grinding zone, which cannot be ignored. Therefore, they developed an analytical thermal model for deep grinding conditions that incorporates the effect of the inclination angle.

Using the tilt-shift heat-source planar model, the average heat flow of the workpiece can then be obtained as shown below.

$$q_w = \frac{\theta_{max}(c\rho)_w \nu_w \sin\varphi}{2\,\mathrm{erf}\left[\nu_w \sin\varphi \cdot (t_o/4\alpha)^{1/2}\right]}. \quad (74)$$

The average heat flow of the composite solid is $q_c = (\theta_{max}/1.128)\sqrt{\nu_s l^{-1}(k\rho c)_c}$. Based on the definition, the EDC considering the inclination of the heat source is given as

$$R = \left\{1 + \frac{2(k\rho c)_c^{1/2}(\nu_s/l_c)^{1/2}}{1.128(c\rho)_w \nu_w \sin\varphi} \cdot \mathrm{erf}\left[\nu_w \sin\varphi \cdot \left(\frac{t_o}{4\alpha_w}\right)\right]\right\}^{-1}. \quad (75)$$

Table 3 further summarizes the factors influencing the EDC model in grinding processing.

3 Convection heat transfer mechanism and modeling

Convection heat transfer is a complex process that involves thermal conduction and convection. This process occurs when a fluid is in direct contact with a solid surface, a relative motion exists between the fluid and the wall, and a temperature difference emerges. Owing to fluid viscosity, in the flow through the solid surface, by the influence of frictional resistance will be formed on the solid surface with a large velocity gradient of the boundary layer. Several factors affect convective heat transfer, including the properties of the fluid, the nature of fluid flow, and the characteristics of the heat transfer surface [118,119].

The cooling effect provided by the coolant plays a crucial role in the machining process. Therefore, accurately determining the CHTC is essential for calculating surface temperature in non-dry machining processes [120]. However, predicting or solving for the CHTC is challenging due to variability in processing parameters, uncertainties in the physical parameters of materials, and differences in fluid properties [121,122].

3.1 Turning

In the turning process, cutting fluid cooling is one of the most commonly used methods for temperature control. Additionally, the high-speed rotation of the workpiece or tool generates strong convection heat transfer with the surrounding air, which plays a crucial role in effectively reducing the workpiece temperature.

In 2023, Yin et al. [123] constructed a model of the CHTC during the turning of slender shafts, aiming to improve the machining accuracy. During the cutting process, the end face and surface of the slender shaft

Table 3 Modeling of EDC in grinding

Model category	Reference	Basis of the model	Grinding wheel	Cooling condition	Model calculation results	Model accuracy
Based on a single grain of grinding wheel	Guo et al. [87]	Distribution of heat sources in right-angled triangles and simplification of one-dimensional heat-conducting processes based on the theory of continuous grinding temperatures in planar surfaces	Aluminum oxide/CBN grinding wheel	Soluble oils, cold air and ester oils	Aluminum oxide grinding wheel is 73%–77%; CBN grinding wheel is 67%–70.5%	Maximum error: 40%
	Qiu et al. [89]	Consideration of heat carried away by chips, improved based on a single particle distribution model	Seeded gel (SG; 3SG80KV)	Dry grinding	76.5%–84.4%	–
	Xu et al. [90]	Combining the heat transfer process, the end face temperature of individual wear grains, and a one-dimensional heat transfer model to analyze the dynamic effect of grinding on the heat transfer process and study the energy distribution ratio	Cup grinding wheel	Wet grinding	6.8%–8.6%	16%–22%
Considering abrasive grain workpiece contact	Rowe [84]	The chip temperature is close to, but not greater than, the melting temperature, and the average temperature in the contact area is approximately two-thirds of the maximum temperature	Aluminum oxide/CBN grinding wheel	Casting cooling	–	–
	Guo et al. [87]	Based on the theory of continuous grinding temperature of flat surfaces, the coolant does not provide sufficient cooling in a closed area	Aluminum oxide/CBN grinding wheel	Soluble oil, cold air, and ester oil cooling	Aluminum oxide grinding wheel is 80%–84.5%; CBN grinding wheel is 79%–83%	–
	Rowe [84]	The abrasive grain, considered as a stationary object, is regarded as a protrusion of infinitesimal depth on a semi-infinite object	Aluminum oxide/CBN grinding wheel	Dry grinding	Aluminum oxide grinding wheel is 65%–80%; CBN grinding wheel is 35%–50%	–
		The time constant reaches infinity when heat transfer enters a steady-state	Aluminum oxide/CBN grinding wheel	Dry grinding	–	–
	Li and Zhao [91]	Using a linearized model in unit time	–	Dry grinding	–	–
Considering the surface temperature of the workpiece	Rowe [84]	Relating the maximum temperature to the heat entering the workpiece using the Jaeger solution for sliding heat sources and corrections for different flux distributions	Aluminum oxide/CBN grinding wheel	Dry grinding	Aluminum oxide grinding wheel is 50%–80%; CBN grinding wheel is 25%–43%	13%–20%
	Hadad et al. [95]	Consider the contact zone as a banded heat source moving along the surface of the workpiece at the speed of the workpiece	Aluminum oxide/CBN grinding wheel	Dry grinding/ MQL/wet grinding	Aluminum oxide grinding wheels MQL grinding is 73%–77%; dry grinding is approximately 82%; wet grinding is below 36%; CBN grinding wheel MQL grinding is 52%; dry grinding is below 14%; wet grinding is approximately 46%	5.4%–15.4%
	Peng et al. [96]	Calculation of the maximum grinding temperature rise of the contact surface based on a one-dimensional conduction sliding heat-source theory using a triangular heat source	Electroplated CBN grinding wheels	Dry grinding/wet grinding	Dry grinding is 28%–39%; wet grinding is below 12%	–
	Ding et al. [98]	Physical model-based approach and moving inclined delta belt source temperature model, derived by finite element simulation and experiments	CBN vitrified bond grinding wheel	Dry grinding	30%–50%	–
Based on material physical parameters	Mao et al. [100]	Considering the change in various physical property parameters at different temperatures	Aluminum oxide/CBN grinding wheel	Wet grinding	–	–
	Ramanath and Shaw [103]	Assuming that the grinding wheel is a perfect adiabatic body and all the heat flows into the workpiece, the energy distribution at the contact of the grinding wheel is even	–	–	51%–70%	–
	Kohli et al. [104]	Matching calculated temperature to measured temperature using triangular heat flow density distribution	Aluminum oxide/CBN grinding wheel	–	Aluminum oxide grinding wheel is 60%–75%; CBN grinding wheel is 20%	–

(*Continued*)

Model category	Reference	Basis of the model	Grinding wheel	Cooling condition	Model calculation results	Model accuracy
Slicing multiple energy distribution subsystems	Jin and Stephenson [105]	Interlinking the energy distribution relationship between the workpiece, the abrasive, the coolant, and the grinding chip	CBN grinding wheel	Mineral oil cooling	51%–83%	–
	Hadad and Sadeghi [106]	An assumption is that the heat is generated at the grinding wheel–workpiece interface and inside the workpiece, with circular contact between the grinding wheel particles and the workpiece, and at a speed consistent with the rotational speed of the grinding wheel	Aluminum oxide/CBN grinding wheel	MQL	55%	–
	Zhu et al. [107]	Considering the geometry and distribution of abrasive grains, individual grains are regarded as cones	CBN grinding wheel	Dry grinding/oil-based coolant	38%–55%	13.8%–21.6 %
	Jin et al. [108]	Extension of the point source temperature rise solution to obtain a model of the kinematic non-uniform heat-source occurring in the grinding zone of a three-dimensional involute shape	SG grinding wheel (3SG46-H12VSP)	Dry grinding	65%–85%	–
Considering convective heat transfer	Yang et al. [109]	Nanofluids are the main medium for heat dissipation in the grinding zone	–	Dry grinding/ spray cooling/ nanoparticle jet spray cooling	–	Less than 7.7%
	Rowe [110]	Calculations based on a simple two-slider model considering the effect of convective heat transfer on energy distribution for different boiling states of the coolant	–	–	–	–
		Correction of the coefficients considering the convective heat transfer between chips and coolant	–	–	54%–87%	–
	Zheng et al. [111]	Solving the EDC model of a workpiece through the relationship between the EDCs of different subsystems	Aluminum oxide grinding wheel	Dry grinding/wet grinding	Wet grinding is 32.3%–34.1%; dry grinding is 45.3%–47.9%	–
Grinding wheel and fluid composite as a whole	Guo and Malkin [88]	Approximating the heat transfer problem in two dimensions and considering the grinding wheel and the fluid as a composite material	Aluminum oxide/CBN grinding wheel	Wet grinding	Aluminum oxide grinding wheel is 60%–70%; CBN grinding wheel is 20%	–
	Lavine [112]	The following assumptions are presented: the fluid fills the entire pore space within the thermal boundary layer, the fluid is at rest relative to the grinding wheel, and the grinding wheel is viewed as a composite of the coolant and abrasive grains	Aluminum oxide grinding wheel	Wet grinding	–	–
	Kim et al. [113]	By measuring the resulting workpiece surface temperature, the energy distribution value is obtained via inverse analysis	Aluminum oxide grinding wheel	Wet grinding	Down grinding is 3%; up grinding is 4.5%	–
	Takazawa [114]	Viewing the grinding wheel and the workpiece as a composite heat conductor and the grinding process as two contact heat conductors moving at different speeds, a one-dimensional thermal conductivity model is used	–	–	–	–
	Yin and Marinescu [115]	Assuming that the grinding wheel is a composite of the coolant and the grinding wheel, most of the heat is conducted to the workpiece and the coolant	–	Wet grinding	About 85%	6.94%–14.87 %
Considering heat source tilt angle	Jin et al. [117]	The EDC is analyzed by considering the inclination effect of the heat-source plane on the direction of motion	–	–	50%–60%	–

experience relative motion with the surrounding air, leading to convective heat transfer.

For the slender shaft end face, the CHTC h_1 is calculated as follows:

$$h_1 = 28\left(1+\sqrt{0.45u}\right), \tag{76}$$

where u is the linear velocity of the ambient air around the circumferential end face, which can be

calculated using the spindle speed n and the diameter d of the slender shaft end face. $u = \pi dn/60000$.

For elongated axial circumferential surfaces, the forced CHTC h_2 can be calculated using the Nusselt equation, which is given by:

$$h_2 = 1000 \cdot Nu \cdot k_a / d, \tag{77}$$

where k_a is the thermal conductivity of air. The Nusselt number Nu is calculated as follows:

$$Nu = \begin{cases} 0.664 Re^{1/2} Pr^{1/2} & (Re < 10^5), \\ 0.037 Re^{4/5} Pr^{1/3} & (Re \geqslant 10^5), \end{cases} \tag{78}$$

where Re is the Reynolds number and Pr is the Prandtl number of the flowing air.

3.2 Milling

Milling is an intermittent process; therefore, air convection also facilitates effective cooling of the tool between machining intervals [124].

3.2.1 Based on fluid mechanics

In 2022, Chen et al. [125] used an analytic approach to model convective heat transfer in tools. Milling, as an intermittent cutting process, allows the tool to cooled through convective heat transfer with the surrounding air when the cutting edge is not in contact with the workpiece [126].

$$h_0 = \frac{Nu \cdot k_a}{D}, \tag{79}$$

where D is the diameter of the milling cutter.

The average Nussle number Nu is

$$Nu = 0.318 Re_r^{0.571}, \tag{80}$$

where Re_r is the dimensionless rotational Reynolds number,

$$Re_r = \frac{\Omega D^2 \rho_a}{2\mu}, \tag{81}$$

where Ω is the cylinder angle, ρ_a is the air density, and μ is the dynamic viscosity of air, and the physical parameters of air are shown in Table 4.

Table 4 Physical parameters of air

Parameter	Value	Unit
k_a	0.024	W/(m·°C)
ρ_a	1.29	kg/m^3
μ	1.983×10^{-5}	kg/(m·s)

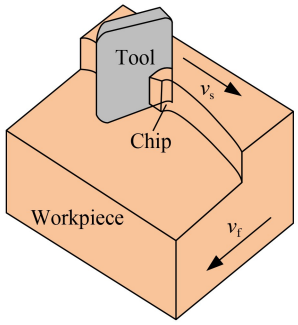

Fig. 29 Schematic of face milling.

3.2.2 Considering air thermal circulation

In 2004, Wang et al. [127] analyzed the CHTC on the surface of a wave-shaped flute milling cutter blade during face milling by integrating principles from heat transfer, fluid mechanics, and cutting theory. As shown in Fig. 29, during face milling, the rotating cutter induces high-speed tangential motion of the surrounding air along the outer edge of the cutter disk, resulting in a phenomenon known as thermal circulation. Considering the complexity of the heat-source flow problem, the CHTC is assumed to be uniform along each convection boundary of the milling cutter. Additionally, the air adjacent to the milling cutter disk is considered an incompressible Newtonian fluid with constant physical properties, no internal heat source, and negligible heat dissipation from viscous friction. Moreover, another assumption is that the air at the wall of the milling cutter disk is in the exuberant turbulence zone.

The layer of air adhering to the wall of the rotating disk moves with a linear velocity v along the outer edge, undergoing uniform circular motion. This flow condition closely resembles to the fluid flow around a single tube. Therefore, the Reynolds number of the air can be expressed as follows:

$$Re = \frac{\pi d^2 n}{60 v}. \tag{82}$$

The air becomes turbulent at normal operating speeds near the knife plate against the wall; thus, airflow is assumed to remain consistently in a turbulent state. The CHTC at the knife plate against the wall is given as follows:

$$h = C \frac{k_f}{d} \left(\frac{\pi D^2 n}{60 v} \right)^m, \tag{83}$$

where D is the diameter of the cutter, k_f is the thermal conductivity of the fluid, and C and m are coefficients to be determined based on the Re criterion.

3.3 Drilling

The drilling process typically occurs deeper within the workpiece, making it more difficult for the cutting

fluid to reach the machining area, which notably affects the cooling efficiency [128,129]. Drilling is generally a fast process and is therefore suitable for analysis under transient situations. Moreover, different regions of the drill experience varying cooling effects [128].

3.3.1 System transient heat transfer

In 2012, Kurgin et al. [130] investigated the CHTC under MQL lubrication during hole reaming. The reaming and drilling processes is typically remarkably rapid, and the system is transient. The capacitance method can be used to solve for the transient CHTC. Assuming no temperature gradient exists within the object, the capacitance equation is as follows:

$$\frac{T_t - T_\infty}{T_a - T_\infty} = \exp\left(-\frac{hA_f}{\rho c V}t\right), \tag{84}$$

where T_t is the temperature at moment t, T_a is the initial temperature of the object, T_∞ is the convective ambient temperature, A_f is the convective surface area, and V is the volume.

The Biot number must be calculated to determine the presence of internal temperature gradients. The results of the total capacity analysis are valid when the Biot number is less than 0.1. The Biot number is calculated as follows:

$$\frac{h(V/A)}{k} < 0.1, \tag{85}$$

where k is the thermal conductivity of the object.

3.3.2 Zoned heat transfer analysis in drilling tools

In 2017, Pontes et al. [131] investigated the CHTC of the cutting fluid over the auger complex to effectively model the temperature at the tool tip. As shown in Figs. 30 and 31, heat exchange can be idealized into four regions during the drilling process. The maximum heat removal occurs in the second region, where the drilling tool and cutting fluid are in contact. Under steady-state conditions, where all heat

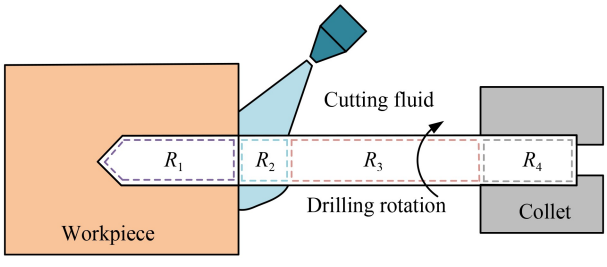

Fig. 30 Modelling of drill tool in four different regions [131].

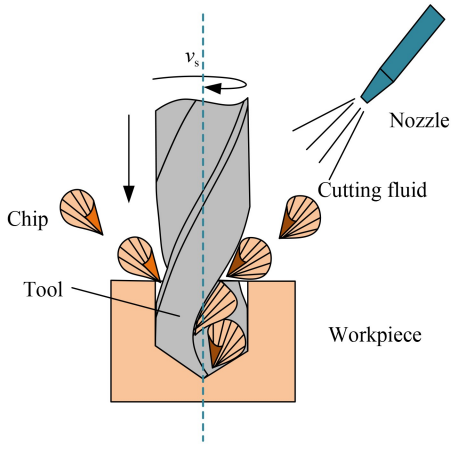

Fig. 31 Schematic representation of the drilling process [131].

transferred to the drill is expected to be exchanged with the cutting fluid, the average temperature of the drill surface in contact with the cutting fluid is calculated as follows:

$$T_d = \frac{1}{A_f}\int_{A_f} T\mathrm{d}A. \tag{86}$$

Once the average drill surface temperature T_d is identified, the average CHTC is calculated as follows:

$$h = \frac{q_f}{A_f(T_d - T_f)}, \tag{87}$$

where T_f is the temperature of the cutting fluid.

Studies focused on modeling CHTC in planning and boring machining are few, and no relevant models have been established. Therefore, these topics will not be discussed further herein. Table 5 provides a summary of the factors that influence the modeling of CHTC in cutting operations.

3.4 Grinding

Compared to cutting, grinding generates more frictional heat due to the intense friction between the abrasive grains and the workpiece. This heat tends to accumulate in the grinding zone, potentially causing burns on the workpiece and damaging the grinding wheel. Therefore, the cooling effect provided by the coolant is critical in the grinding process [132]. The convective heat transfer of the coolant is a primary mechanism for dissipating heat in the grinding zone, especially during coolant flooding, where most of the heat is carried away through the coolant [133]. Therefore, in non-dry grinding, determining the CHTC is a key factor in predicting the workpiece surface temperature and controlling machining quality [134].

However, excessive use of coolant has many

Table 5 Modeling of CHTC coefficients in cutting operations

Processing method	Model category	Reference	Basis of the model	Machining tools	Cooling condition	Model calculation results	Model accuracy
Turning	Distinguishing workpiece convection surfaces	Yin et al. [123]	The workpiece is an elongated shaft, and the different surfaces are considered separately	Carbide cutting tools	Dry cutting	The rotating end face of the slender shaft is 6.17 × 10^{-5} W/(mm^2·K); the rotating surface is 4.526 × 10^{-5} W/(mm^2·K)	–
Milling	Based on fluid mechanics	Chen et al. [125]	Analytical method, considering convective heat transfer with air	Carbide four-flute milling cutter	Dry milling	–	–
	Consider air thermal circulation	Wang et al. [127]	Combining heat transfer, fluid dynamics, and cutting theory, the heat bypass problem is considered, assuming that the CHTC is equal for each convection boundary of the milling cutter	Wave edge milling cutter	Dry milling	–	–
Drilling	System transient heat transfer	Kurgin et al. [130]	The heat transfer process is remarkably fast and transient, assuming the absence of temperature gradient inside the object	–	MQL	22–300 W/(m^2·°C)	When the Biot number is less than 0.1, the error is within 5%
	Zoned heat transfer analysis in drilling tools	Pontes et al. [131]	Dividing the drill bit into four heat exchange zones, all heat transferred to the drill bit is expected to exchange with the cutting fluid	Steel core drilling tools	Cutting fluid lubrication	3270–5190 W/(m^2·K)	–

disadvantages [135], and in high-speed grinding, breaking through the air barrier layer and effectively reaching the grinding zone for cooling is difficult for the coolant [136,137]. Therefore, researchers have developed a variety of cooling methods such as MQL [138,139] and NMQL [140,141]. Owing to the diversity of cooling methods and the variability of machining conditions, determining the CHTC becomes a complex problem [142]. Researchers have used a variety of approaches to derive different CHTC models, including those that consider factors such as boiling states of the fluid, particle contact conditions, different grinding zones, and those based on hydrodynamics, statistical theory, energy distribution.

3.4.1 Considering the fluid boiling state

In 2019, Zhang et al. [99] investigated the grinding process of low-temperature air nanofluid MQL lubrication and established a CHTC model based on the theory of boiling heat transfer and conduction. Notably, the boiling heat transfer process in the grinding zone can be divided into four stages: natural convective heat transfer, nucleate boiling heat transfer, transition boiling heat transfer, and film boiling heat transfer. The effect of grinding temperature on the heat transfer coefficient is shown in Fig. 32, demonstrating the four boiling stages of the cooling medium.

In a natural convection state, the coolant does not boil, and nanofluid convection heat transfer becomes the main heat transfer mode. Yang et al. [143] investigated the CHTC under MQL conditions without considering the boiling convection heat transfer coefficient. When the nanofluid is injected into the grinding zone, the ejected nanofluid is discretized into N_l droplets, each with a volume V_l per unit time as follows:

$$\begin{cases} V_\mathrm{i} = r_\mathrm{surf}^3 \cdot \left\{ \dfrac{\pi}{2} \dfrac{1}{\tan\theta_\mathrm{n}} \left(\dfrac{1}{\cos\theta_\mathrm{n}} - 1 \right) \right. \\ \qquad \left. \cdot \left[1 + \dfrac{1}{3} \dfrac{1}{\tan^2\theta_\mathrm{n}} \left(\dfrac{1}{\cos\theta_\mathrm{n}} - 1 \right)^2 \right] \right\}^{-1}, \\ V_\mathrm{l} = \dfrac{\pi d_0^3}{6}, \\ N_\mathrm{l} = \dfrac{Q' t}{V_\mathrm{l}}, \\ t = \dfrac{a_\mathrm{w}}{v_\mathrm{w}}, \end{cases} \tag{88}$$

where Q' is the nanofluid supply during the grinding time, r_surf is the diffusion radius of a single droplet, N_l is the droplet volume, t is the total grinding time, a_w is the length of the workpiece, V_l is the volume of a single droplet, d_0 is the diameter of the sphere of a single droplet, and θ_n is the contact angle.

Therefore, the CHTC for the natural convection state is introduced as follows:

$$h_{n1} = \frac{N_\mathrm{l} c_\mathrm{l} \rho_\mathrm{l} V_\mathrm{l}}{\pi r_\mathrm{surf}^2 \cdot t} + h'_\mathrm{a}, \tag{89}$$

where c_l is the droplet specific heat capacity, ρ_l is the nanofluid density, T_s is the saturation temperature, and h'_a is the room temperature air CHTC.

When the boiling state of the coolant is considered, as shown in Fig. 32, the CHTC reaches its maximum value at the endpoint of nucleated boiling, which

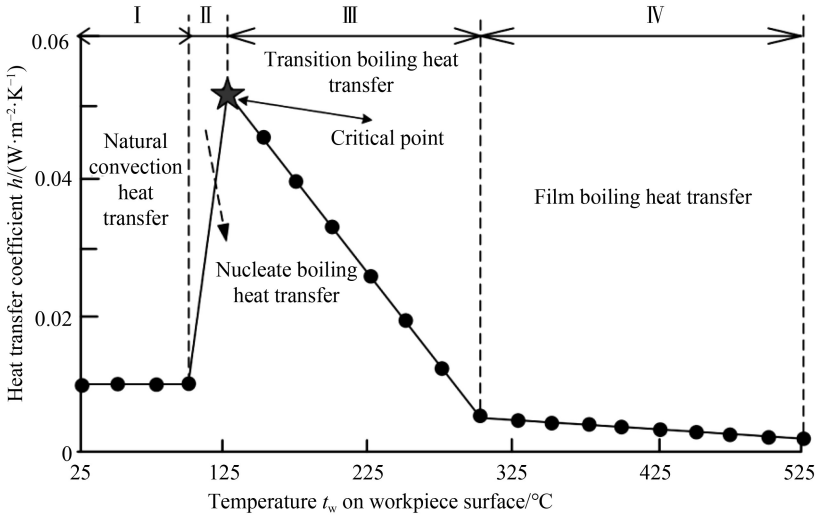

Fig. 32 Schematic of the influence of grinding surface temperature on heat transfer coefficient [99].

marks the starting point of transitional boiling heat transfer. At this point, the CHTC can be calculated as follows:

$$h_{n2}=\frac{\left[h_{fa}+c_l(T_s-T_l)\right]Q'\rho_l}{\pi r_{surf}^2(T_{n2}-T_l)}+h'_a, \tag{90}$$

where h_{fa} is the latent heat of vaporization and T_l is the nanofluid temperature.

When the nanofluid enters the film boiling state, the endpoint of transitional boiling marks the starting point of film boiling. At this stage, the CHTC is calculated as follows:

$$\begin{cases} h_{n3}=\dfrac{N_l Q'\rho_l\left[h_{f_d}+c_l(T_s-T_l)\right]}{bl_c(T_{n3}-T_l)} \cdot\left\{0.027\exp\left[\dfrac{0.08\sqrt{\ln(We/35+1)}}{B^{1.5}}\right]+0.21k_dB\cdot\exp\left(-\dfrac{90}{We+1}\right)\right\}+h'_a, \\ We=\dfrac{\rho_l d_0 v_n^2}{\sigma}, \\ v_n=\sqrt{\dfrac{\frac{p_0-p_0}{\rho_l}+\frac{16Q'^2}{\pi^2 d_0^2}}{1+\varepsilon}}\cdot\cos\theta, \\ B=\dfrac{c_v(T_m-T_s)}{h_{fa}}, \\ l_c=\sqrt{a_p d_s}, \\ k_d=\dfrac{k_v}{c_v\mu_v}, \end{cases} \tag{91}$$

where p_a is the pressure inside the nozzle, p_0 is the atmospheric pressure, v_l is the droplet jet velocity along the nozzle direction, v_n is the droplet vertical impact velocity on the heat transfer surface, k_v is the thermal conductivity of the steam, μ_v is the steam kinetic viscosity, c_v is the mass heat capacity of the steam, θ is the droplet jet and the horizontal direction of the angle, and σ is the surface tension.

In 2023, Liu et al. [144] analyzed the heat transfer behavior of the liquid film at the interface of the low-temperature cold air MQL-lubricated grinding wheel–workpiece. They further established a CHTC model based on the liquid film flow heat transfer process within the grinding zone. As shown in Fig. 33, the total liquid film heat transfer q_t in the grinding zone comprises the liquid film flow heat transfer q_f and the heat transfer from the boiling bubble group q_b.

For the total heat of the liquid film, the energy input into the grinding zone is assumed to be completely converted into the heat generated during the interaction between the grinding wheel and the workpiece.

$$Q_t=F_x\cdot l_c=F_x\cdot\sqrt{d_s a_p}. \tag{92}$$

For the boiling bubble heat exchange, the liquid film in the nucleate boiling state is assumed to form spherical bubbles on the workpiece surface. Applying the Fritz formula, all the bubbles, from the nucleation of the gas to their growth and detachment, contribute to the total heat absorbed, denoted as Q_b.

$$Q_b=N_b w l_c\zeta_b\rho_a\frac{\pi d_b^3}{6}, \tag{93}$$

where ζ_b is the latent heat of the bubble, taken as 384.3 kJ/kg. d_b is the diameter of a single bubble, ρ_a is the density of the air, and N_b is the number of nucleation sites (per unit area) on the superheated surface.

The CHTC of the flowing liquid film can be modeled by substituting the parameters into the relevant calculation equation as follows:

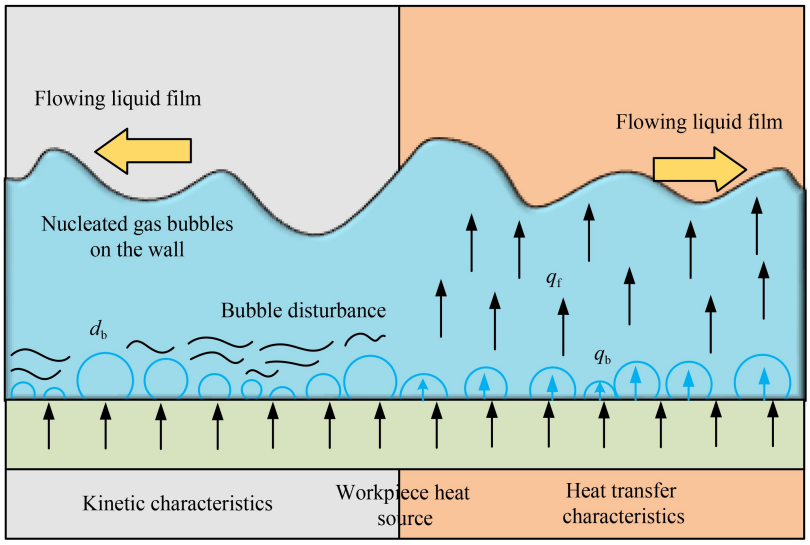

Fig. 33 Nucleate boiling and flow heat transfer process of flowing liquid film in the grinding zone.

$$h_f = \frac{(Q_t - Q_b) \cdot h_a}{Nu_f \cdot wl_c(T_w - T_f)}. \tag{94}$$

In 2014, Mao et al. [145] established a mathematical model for the heat transfer coefficient in the MQL grinding zone, based on the atomization mechanism and the varying heat transfer characteristics exhibited of droplets at different wall temperatures. Aiming to simplify the calculation, an assumption is that a constant heat flow is applied to a small unit of the grinding surface within a unit time step. The droplets are further assumed to penetrate the air barrier and vapor layer surrounding the grinding wheel, entering the small contact area for effective heat transfer. The heat transfer on the surface is assumed to occur through convection for the air, while the droplets transfer heat through heating and boiling. Given the small diameter of the droplets, they are assumed to reach the wall temperature instantaneously upon contact with the heat transfer surface.

No boiling heat exchange. The heat transfer in this region is divided into two components: convective heat transfer between the air and the wall, and heating heat transfer of the liquid droplets. By applying the Nusselt number calculation equation, the CHTC for the air to the wall is as follows:

$$h_a = 0.906 Re^{1/2} Pr^{1/3} k_a l^{-1}. \tag{95}$$

The heat transfer coefficient h_l for droplet heating is as follows:

$$h_l = \frac{c_l m_0 (t_w - t_l)}{t_w - t_l}, \tag{96}$$

where m_0 is the mass of the droplets involved in the heat transfer and t_l is the initial temperature of the droplets.

The total heat transfer coefficients are presented as follows:

$$h = h_a + h_l. \tag{97}$$

In the non-boiling zone, the heat carried away by MQL cooling and the wall temperature are approximately linear. Therefore, the heat transfer coefficient in this region can be approximated as a constant value.

Nucleate boiling heat transfer and transition boiling heat transfer. In the nucleate boiling zone and the transition boiling heat transfer zone, the change in heat transfer is highly complex, and the relationship between wall temperature becomes nonlinear. However, the spray heat transfer and wall temperature follow a parabolic distribution, reaching a maximum at the critical heat flow density at the maximum value. The critical heat flow density is as follows:

$$\begin{aligned} q_{max} &= N_l \left[h_{fa} + c_l(t_s - t_l)\right] \varphi + q'_a, \\ q'_a &= 0.906 Re^{1/2} Pr^{1/3} \frac{\lambda}{l}(t_w - t_0), \end{aligned} \tag{98}$$

where q'_a is the air convection heat transfer and φ is the liquid mass flow rate.

Assuming that all droplets sprayed onto the heat transfer surface are evaporated and that N_l is 1, it can be simplified as follows:

$$q_{max} = \left[h_{fa} + c_l(t_s - t_l)\right] \varphi + q'_a. \tag{99}$$

Therefore, the heat transfer coefficient at the critical heat flow density is calculated as follows:

$$h_{max} = \frac{q_{max}}{t_w - t_l}. \tag{100}$$

Stabilized film boiling heat transfer. The heat transfer in this area includes the following three components: heat transfer between liquid droplets and the hot surface, convective heat transfer between the airflow and the hot surface, and the heat transfer of a single droplet hitting the high-temperature wall, which can be expressed as follows:

$$q_{\mathrm{d}} = \frac{\pi d^3}{6}\rho_{\mathrm{l}}\left[h_{\mathrm{fa}} + c_{\mathrm{l}}(t_{\mathrm{s}} - t_{\mathrm{l}})\right] \cdot \left\{0.027 \cdot \exp\left[\frac{0.08\sqrt{\ln(We/35+1)}}{B^{1.5}}\right] + 0.21 k_{\mathrm{d}} B \cdot \exp\left(\frac{-90}{We+1}\right)\right\}, \tag{101}$$

where We is the Weber number; $We = \rho_1 d v_{\mathrm{n}}^3/\sigma$. Also, we have $B = c_{\mathrm{v}}(t_{\mathrm{w}} - t_{\mathrm{s}})/h_{\mathrm{fa}}$ and $k_{\mathrm{d}} = k_{\mathrm{v}}/(c_{\mathrm{v}}\mu_{\mathrm{v}})$.

High-temperature surface heat transfer due to droplet collision per unit area per unit time:

$$q_1'' = q_{\mathrm{d}} N_{\mathrm{l}} = q_{\mathrm{d}} \frac{6Q_{\mathrm{l}}}{S\pi {d_0}^3}, \tag{102}$$

where S is the area covered by the nozzle jet and d_0 is the droplet diameter.

The convective heat exchange between air flow and wall surface is calculated as follows:

$$q_{\mathrm{a}}'' = 0.906 Re^{1/2} Pr^{1/3} \frac{\lambda}{l}(t_{\mathrm{w}} - t_0). \tag{103}$$

Consequently, the CHTC in the boiling zone of the stable film state is presented below.

$$h_{\mathrm{b}} = \frac{q_1'' + q_{\mathrm{a}}''}{t_{\mathrm{w}} - t_0}. \tag{104}$$

3.4.2 Based on fluid mechanics

In 2024, Gupta and Yadav [22] employed computational fluid dynamics to develop a mathematical model for the CHTC of the coolant. They analyzed the total heat generated in the grinding zone and its distribution among the grinding wheel, workpiece, fluid, and chips. The heat flow to the fluid, denoted as q_{f}, is expressed as follows:

$$q_{\mathrm{f}} = h_{\mathrm{f}} \cdot T_{\max} = q_{\mathrm{t}} - (q_{\mathrm{w}} + q_{\mathrm{s}} + q_{\mathrm{ch}}), \tag{105}$$

where the total heat q_{t} depends on the speed ratio, grinding depth, grinding wheel, workpiece material, and diameter.

$$q_{\mathrm{t}} = \frac{\nu_{\mathrm{w}}}{\nu_{\mathrm{t}}} a_{\mathrm{p}}^{3/2} d_{\mathrm{s}}^{1/2} F_{\mathrm{vm}},$$

$$q_{\mathrm{w}} = \frac{\beta_{\mathrm{w}}}{\mathrm{C}} \sqrt{\frac{\nu_{\mathrm{p}}}{l_{\mathrm{c}}}} \cdot T_{\max},$$

$$q_{\mathrm{s}} = q_{\mathrm{w}} \frac{k_{\mathrm{g}}}{\beta_{\mathrm{w}}\sqrt{r_{\mathrm{a}}\nu_{\mathrm{t}}}},$$

$$q_{\mathrm{ch}} = \frac{pcav_{\mathrm{p}}}{l_{\mathrm{c}}} \cdot T_{\mathrm{ch}}, \tag{106}$$

where F_{vm} is the specific main grinding resistance.

In 2017, Yang et al. [146] investigated micro-scale cranial grinding under various cooling conditions and developed a CHTC model based on fluid dynamics.

$$h = 0.023 k_{\mathrm{nf}} (2u_0 b_0)^{0.8} \eta^{-0.8} Pr^{0.4}/(2b_0), \tag{107}$$

where k_{nf} is the thermal conductivity of the fluid, u_0 is the exit velocity, b_0 is the half-width of the nozzle exit cross-section, and η is the kinematic viscosity of the fluid. After transformation, h can be modified as follows:

$$h = 105.6 k_{\mathrm{nf}}^{0.6} \rho_{\mathrm{nf}}^{0.8} c_{\mathrm{nf}}^{0.4}/\mu^{0.4}, \tag{108}$$

where ρ_{nf} is the fluid density, c_{nf} is the specific heat capacity of the fluid, and μ_{f} is the dynamic viscosity of the fluid.

In 2003, Jin et al. [147] estimated the CHTC using a fluid dynamics and thermal model fit. When the coolant enters the grinding area, the temperature distribution of the cooling medium within the thermal boundary layer is shown in Fig. 34(a). Assuming the surface temperature of the workpiece is uniform and constant at T_{w}, the coolant temperature outside the thermal boundary layer is also set as T_{w}. As shown in Fig. 34(b), δ_{t} denotes the thickness of the thermal boundary layer at position x. An assumption is that the flow rate of the coolant is equal to the peripheral speed of the grinding wheel. At the surface of the workpiece, the heat flow q is expressed as shown below.

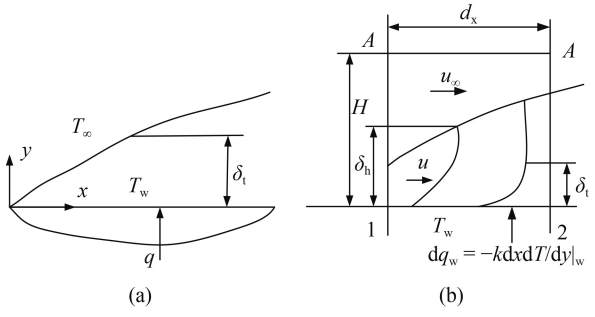

Fig. 34 (a) Thermal boundary layer of the coolant on the workpiece surface. (b) Control volume within the grinding zone for energy balance [147].

$$q = -k\left.\frac{\partial T}{\partial y}\right|_{\mathrm{w}} = h_{\mathrm{c}}(T_{\mathrm{w}} - T_\infty). \tag{109}$$

Solving for the CHTC, h_{c}, requires a coolant temperature gradient at the workpiece surface, while the internal temperature distribution of the coolant, T_{w} and T_∞, is related as follows:

$$\frac{T-T_{\mathrm{w}}}{T_{\infty}-T_{\mathrm{w}}}=\frac{3}{2}\frac{y}{\delta_{\mathrm{t}}}-\frac{1}{2}\left(\frac{y}{\delta_{\mathrm{t}}}\right)^{3}, \tag{110}$$

where δ is the thickness of the coolant film in the grinding zone.

By solving the integral equation with appropriate boundary conditions, the fluid mass flow is determined, from which the pressure gradient is derived. Then, through energy balance, the thermal boundary thickness δ_{t} is obtained as follows:

$$A_4\delta_{\mathrm{t}}^4+A_3\delta_{\mathrm{t}}^3+A_2\delta_{\mathrm{t}}^2+A_1\delta_{\mathrm{t}}+A_0=0, \tag{111}$$

where $A_0=-\frac{3}{2}\alpha(T_{\infty}-T_{\mathrm{w}})$, $A_1=0$, $A_2=\frac{\mu}{\rho c}\left[\frac{1}{2}\left(\frac{v_{\mathrm{s}}}{\delta}\right)^2-\frac{v_{\mathrm{s}}k_1}{2\mu}+\frac{k_1^2}{8\mu^2}\right]+\left[T_{\mathrm{w}}+\frac{4}{5}(T_{\infty}-T_{\mathrm{w}})\right]\cdot\left(\frac{v_{\mathrm{s}}}{\delta}-\frac{k_1\delta}{2\mu}\right)\cdot(T_{\infty}-T_{\mathrm{w}})$, $A_3=\frac{k_1}{\rho c}\left(\frac{v_{\mathrm{s}}}{4\delta}-\frac{k_1\delta}{8\mu}\right)+\frac{k_1}{2\mu}\left[T_{\mathrm{w}}+\frac{7}{8}(T_{\infty}-T_{\mathrm{w}})\right]\cdot(T_{\infty}-T_{\mathrm{w}})$, and $A_4=\frac{k_1^2}{24\mu\rho c}$.

This condition leads to four solutions, wherein only one fits the thermal boundary thickness range from which the CHTC h_{c} can be derived.

In 2009, Lin et al. [148,149] investigated the CHTC of a fluid using fluid dynamics theory and an analytical model to describe heat transfer in the grinding zone under different grinding conditions. They developed an analytical model for calculating the CHTC by coupling fluid dynamics with heat transfer theory. As shown in Fig. 35, a schematic illustrates the heat transfer between the grinding wheel and the workpiece under typical surface grinding conditions.

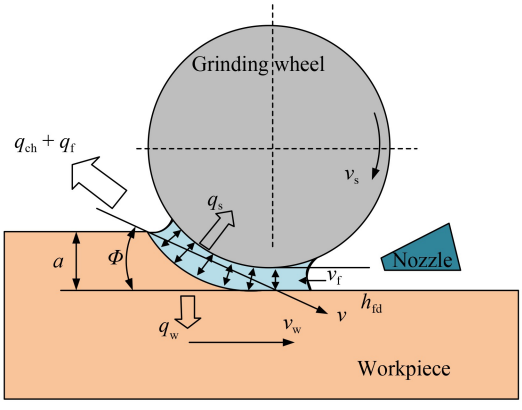

Fig. 35 Illustration of fluid application in surface grinding [148].

First, semi-empirical equations based on the theory of heat conduction in solids yield the following:

$$Nu=0.664Re^{1/2}Pr^{1/3}, \tag{112}$$

where $Re=\rho_{\mathrm{f}}\nu_{\mathrm{av}}l_{\mathrm{c}}/\mu_{\mathrm{f}}$, $Pr=\mu_{\mathrm{f}}C_{\mathrm{f}}/k_{\mathrm{f}}$, and $Nu=h_{\mathrm{f}}l_{\mathrm{c}}/k_{\mathrm{f}}$.

Combining the above equations, the CHTC h_{f} is then derived as follows:

$$h_{\mathrm{f}}=G\sqrt{\frac{\nu_{\mathrm{a}}\nu}{l_{\mathrm{c}}}}, \tag{113}$$

where v_{av} is the average velocity of the fluid through the grinding zone. G is a constant related to density, temperature, and the friction coefficient.

$$\begin{aligned}G&=0.664\rho^{1/2}C_{\mathrm{p}}^{1/3}\mu^{-1/6},\\ l_{\mathrm{c}}&=\left[8R_{\mathrm{r}}^2F_{\mathrm{n}}'(k_{\mathrm{s}}+k_{\mathrm{w}})d_{\mathrm{s}}+ad_{\mathrm{s}}\right]^{1/2},\end{aligned} \tag{114}$$

where R_{r} is the roughness factor.

3.4.3 Adoption of the backpropagation method

In 2022, Jin et al. [150] established a backpropagation calculation method to determine the distribution of fluid CHTC in the grinding zone under deep-cut grinding conditions. This method is based on measured grinding temperature signals and a circular contact moving heat-source model.

By considering the energy distribution of heat flow in the grinding zone—among the workpiece, grinding wheel, grinding chips, and grinding fluid—the temperature distribution obtained through actual measurement can be used for inverse analysis to deduce the heat flux density distribution across these subsystems. This process leads to the introduction of the CHTC in the grinding zone, as illustrated in Fig. 36.

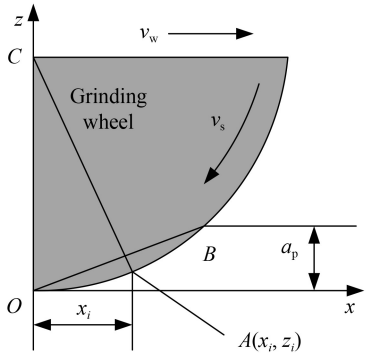

Fig. 36 Schematic of the contact zone for grinding wheels.

$$h_{\mathrm{f}}(x_i)=h_{\mathrm{w}}(x_i)\left[\frac{1}{R_{\mathrm{w}}(x_i)}-\frac{1}{R_{\mathrm{ws}}}-\frac{1}{R_{\mathrm{wch}}(x_i)}+1\right]. \tag{115}$$

Gao et al. [151] improved the model for calculating the CHTC in vertical axis surface grinding, based on the research of Hideo Fukui in Japan. They analyzed the grinding temperature using an analytical method and obtained the temperature distribution along the depth direction of the surface by measuring temperatures at various depths within the workpiece surface layer. This data was then used to derive a formula for calculating the grinding CHTC.

The amount of heat convected outward from a surface is proportional to the temperature difference between the surface and the surrounding fluid, as well as the heat transfer area. For a one-dimensional heat conduction problem, the heat flux through a surface can be determined from the basic definition of heat conduction, and applying the law of conservation of energy yields the following expression:

$$h = k\left.\frac{\partial T}{\partial z}\right|_{z=0}(T_{\mathrm{w}} - T_{\mathrm{f}})^{-1}. \tag{116}$$

The temperature gradient near the surface and its surface temperature are difficult to determine directly. However, they can be measured by measuring the temperature of the surface layer of the workpiece at different depths, allowing for the determination of the temperature distribution along the depth direction of the object, and subsequently, the required parameters. Let the temperature distribution of the surface layer of the object follow a parabolic distribution.

$$T(z) = A_0 + A_1 z + A_2 z^2, \tag{117}$$

where A_0, A_1, and A_2 are coefficients to be determined.

$$\begin{aligned} &T_{\mathrm{w}} = T(z)|_{z=0} = A_0, \\ &\left.\frac{\partial T}{\partial z}\right|_{z=0} = A_{\mathrm{f}}. \end{aligned} \tag{118}$$

Considering Eq. (117), we have

$$h = kA_1(A_0 - T_{\mathrm{f}})^{-1}. \tag{119}$$

When the three-point method is used to measure the surface temperature of the workpiece today, the coefficients A_0 and A_1 and are determined using the following equation:

$$\begin{cases} A_0 = \dfrac{z_1 \cdot z_3}{(z_3 - z_1)(z_2 - z_1)}T_1 - \dfrac{z_1 \cdot z_3}{(z_2 - z_1)(z_3 - z_2)}T_2 \\ \qquad + \dfrac{z_1 \cdot z_2}{(z_3 - z_1)(z_3 - z_2)}T_3, \\ A_1 = -\dfrac{z_3 + z_1}{(z_2 - z_1)(z_3 - z_1)}T_1 + \dfrac{z_3 + z_1}{(z_3 - z_2)(z_2 - z_1)}T_2 \\ \qquad - \dfrac{z_2 + z_1}{(z_3 - z_2)(z_3 - z_1)}T_3. \end{cases} \tag{120}$$

3.4.4 Based on the Péclet number

Lavine and Jen [152] assumed that the heat flow in the grinding zone is uniform and that the coolant fills the intergranular pores. They further assumed that the coolant is stationary relative to the grinding wheel and can be treated as a moving "semi-infinite solid". By neglecting heat transfer in the direction of motion, the fluid is assumed to be in an unboiled liquid state with a depth greater than the thermal boundary layer thickness. Based on the large Péclet number of the coolant (typically of the order of 10^5 or greater), the heat transfer coefficient of the fluid is as follows:

$$h_{\mathrm{f}}(x) = \sqrt{\pi(k\rho c_{\mathrm{p}})_{\mathrm{f}} v_{\mathrm{s}}/(4x)}, \tag{121}$$

where x is the distance from the grinding zone.

In 2015, Vinay and Srinivasa Rao [153] briefly analyzed the temperature destination in the grinding zone, as shown in Fig. 37. They also calculated the CHTC of the grinding fluid based on the motion characteristics during the grinding process, as shown below.

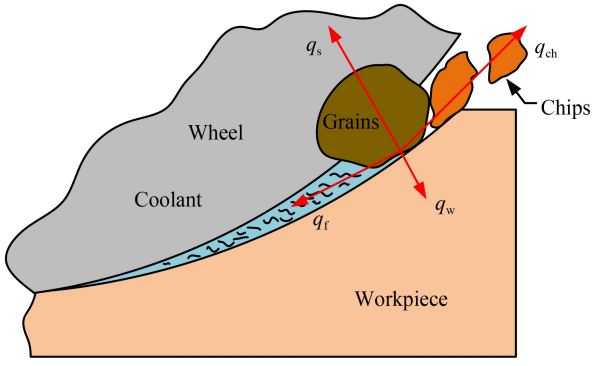

Fig. 37 Heat transfer paths within the contact zone [153].

$$h_{\mathrm{wp}} = \frac{\beta_{\mathrm{wp}}}{C}\sqrt{\frac{\nu_{\mathrm{s}}}{l_{\mathrm{c}}}}, \tag{122}$$

where C is the correction factor and depends on the dimensionless Péclet number Pe, according to Rowe [97]:

$$C = \begin{cases} 1.06, & \text{if } Pe > 10, \\ \dfrac{0.95}{\pi}\sqrt{2\pi + \dfrac{Pe}{2}}, & \text{if } 0.2 < Pe < 10, \\ 0.76, & \text{if } Pe < 0.2. \end{cases} \tag{123}$$

3.4.5 Differences in fluids in different areas of the grinding zone

In 2008, Shen [154] estimated the CHTC during the grinding process using the finite difference method for grinding heat modeling. Considering the complexity of the actual boundary conditions in the grinding process, different regions were analyzed and discussed in detail. The planar grinding configuration is shown in Fig. 38. The actual depth of cut in the grinding

zone decreases from the leading edge to the trailing edge, resulting in uneven convective cooling, the leading edge, contact zone, and trailing edge of the workpiece are considered separately. The grinding zone CHTC h_{contact} is assumed to be a linear function, as presented in Fig. 38:

$$h_{\text{contact}}(x) = h_1 + \frac{h_2 - h_1}{l_c}\left(x + \frac{l_c}{2}\right), \tag{124}$$

where $h_1 = \max[h_{\text{contact}}(x)]$ and $h_2 = \max[h_{\text{contact}}(x)]$. x is the local coordinate of the origin at the center of the grinding zone.

Assuming that the CHTC at the trailing edge is uniform, the CHTC between the trailing edge and the end of the contact zone does not vary. Therefore, at the trailing edge: $h_{\text{trailing}} = h_1$.

The cooldown effect of the leading edge is negligible; therefore, $h_{\text{leading}} = 0$.

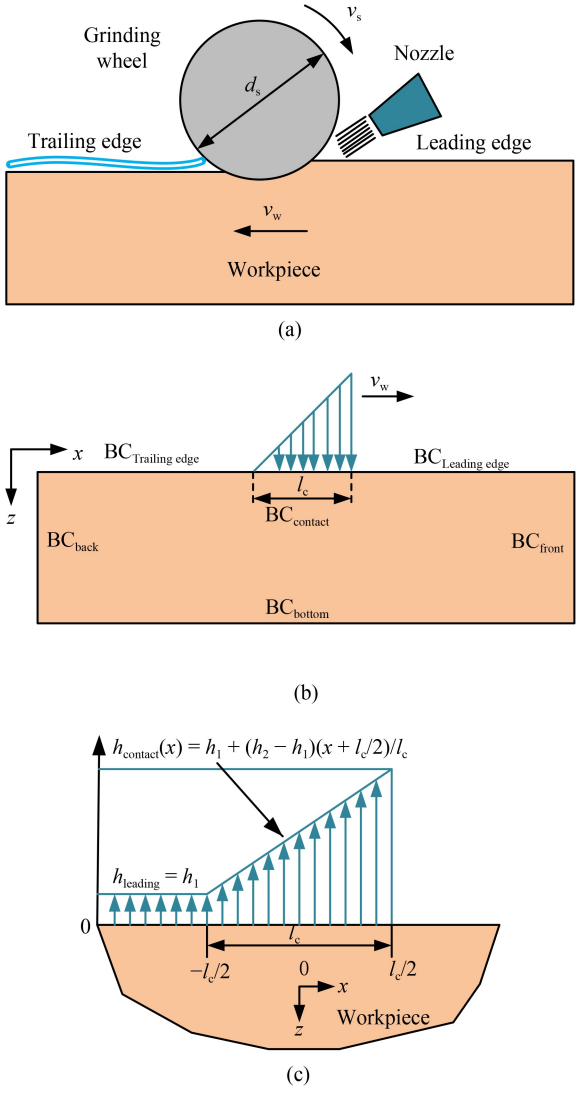

Fig. 38 Illustration of the boundary conditions (BCs): (a) surface grinding process and (b) the corresponding BCs. (c) Assumption of convection heat transfer coefficient.

3.4.6 Based on particle contact conditions

In 2013, Zhu et al. [107] proposed an improved temperature calculation model that considers the geometry and distribution of abrasive grains to improve model accuracy. Considering the effects of abrasive grain geometry, size, and concentration, the CHTC model was modified to propose a calculation model based on cross-arrays of grains. Assuming that the abrasive grains on the surface of the grinding wheel are arranged in an orderly manner according to a cross-array pattern, as shown in Figs. 22 and 39, and that the abrasive grains are modeled as cylinders with the same diameter, a new calculation model for the CHTC of the grinding surface of the workpiece is derived based on the multirow bundle heat transfer model for the outward flow of the fluid, as follows:

$$h_f = \frac{Nu \cdot k_f}{L_c} = \frac{Nu \cdot k_f}{d_g N} = \frac{Nu \cdot k_f}{d_g l_c L_g^{-1}}, \tag{125}$$

where L_c is the characteristic length, d_g is the equivalent mean abrasive grain diameter, and L_g is the mean particle spacing.

If the coefficients are integrated into the model by taking the average grain spacing to be approximately 1.5 times the grain spacing in the grinding wheel, and using the semi-empirical equations for the forced convection theory, the model for calculating the CHTC can be then rewritten as follows:

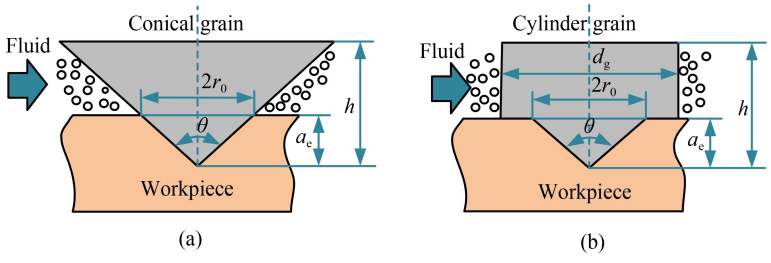

Fig. 39 (a) Before and (b) after of the equivalent average grain diameter [107].

$$h_{\mathrm{f}}=\frac{0.664 v_{\mathrm{s}}^{1/2} L_{\mathrm{g}}^{1/2} k_{\mathrm{f}}}{v_{\mathrm{f}}^{1/6} \alpha_{\mathrm{f}}^{1/3} d_{\mathrm{g}}^{1/2} l_{\mathrm{c}}^{1/2}}, \tag{126}$$

where α_{f} represents the thermal diffusion coefficient of the fluid.

3.4.7 Considering the fluid flow state

Zhang and Rowe [155,156] studied the role of fluid convection in cryogenic grinding around 2020. Convective heat transfer models typically assume that the fluid flows over the workpiece surface in a laminar flow state within the grinding zone. However, in reality, the fluid is mechanically agitated due to the constraints of the abrasive material, making the assumption of steady laminar flow problematic. Therefore, the CHTC in various cases is investigated based on the different flow states of the fluid.

Laminar flow modeling. When the fluid state in the grinding zone is determined to be laminar flow, the CHTC is obtained based on the assumption that the fluid flows through a smooth surface, as follows:

$$h_{\mathrm{f}}=\frac{4}{9} \rho_{\mathrm{f}}^{1/2} C_{\mathrm{f}}^{1/3} \eta^{-1/6} k_{\mathrm{f}}^{2/3} \nu_{\mathrm{s}}^{1/2} l_{\mathrm{c}}^{-1/2}. \tag{127}$$

Turbulent flow modeling. The results revealed that the fluid in the grinding zone behaves turbulently. This assumption is highly realistic because the fluid is vigorously agitated by the high-speed particles in the limited pore space between the grinding wheel particles. Turbulence helps bring the cooling fluid closer to the working surface by reducing the laminar boundary layer. As shown in Fig. 40, the dashed line shows the typical fluid temperature distribution. Therefore, the calculation of CHTC, considering turbulent flow, is modeled as follows:

$$h_{\mathrm{f}} \approx \frac{1}{40} \rho_{\mathrm{f}}^{4/5} C_{\mathrm{f}}^{1/3} \eta^{-7/15} k_{\mathrm{f}}^{2/3} \nu_{\mathrm{s}}^{4/5} l_{\mathrm{c}}^{-1/5}. \tag{128}$$

Fluid–wheel model. The boundary layer of the fluid is completely eliminated, and the fluid is assumed to maintain a zero-temperature rise to the workpiece surface, at which point the maximum CHTC will be produced, indicating an impossible limiting assumption. The following assumptions are also presented: the fluid entering the grinding contact zone is at zero-temperature rise above room temperature, the fluid passes through the workpiece at wheel speed, and a thermal boundary layer is established in a solid with heat transfer characteristics of the fluid. Thus, the CHTC is as follows:

$$h_{\mathrm{f}}=k_{\mathrm{f}}^{1/2} \rho_{\mathrm{f}}^{1/2} c_{\mathrm{f}}^{1/2} \nu_{\mathrm{s}}^{1/2} l_{\mathrm{c}}^{-1/2}. \tag{129}$$

In 2016, Wang [157] expressed the convective heat transfer problem in terms of a set of convective heat transfer differential equations and definite solution conditions. As shown in Fig. 41, when the grinding fluid first enters the grinding zone, it can be approximated as a laminar flow with velocity v_{s} over the workpiece surface. However, as the flow distance x increases, the flow transitions toward turbulence.

In the laminar flow state, the boundary layer integral equation system is used to solve for the CHTC. The average CHTC can then be obtained by averaging the local CHTC integrals over the length l_{c} under the condition of $Pr \geqslant 1$:

$$\bar{h}_{\mathrm{f}}=0.664 \frac{k_{\mathrm{f}}}{l_{\mathrm{c}}} Re^{1/2} Pr^{1/3}. \tag{130}$$

The temperature distribution is inhomogeneous over the entire length of the grinding arc; thus, the average CHTC is two-thirds localized CHTC.

$$\begin{cases} \bar{h}_{\mathrm{f}}=0.4427 \dfrac{k_{\mathrm{f}}}{l_{\mathrm{c}}} Re^{1/2} Pr^{1/3}, \\ Re=\dfrac{\rho_{\mathrm{f}} \nu_{\mathrm{s}} l_{\mathrm{c}}}{\eta_{\mathrm{f}}}, \\ Pr=\dfrac{C_{\mathrm{f}} \eta}{k_{\mathrm{f}}}. \end{cases} \tag{131}$$

The same method is applied in the case of turbulent flow. When the laminar flow section is notably short

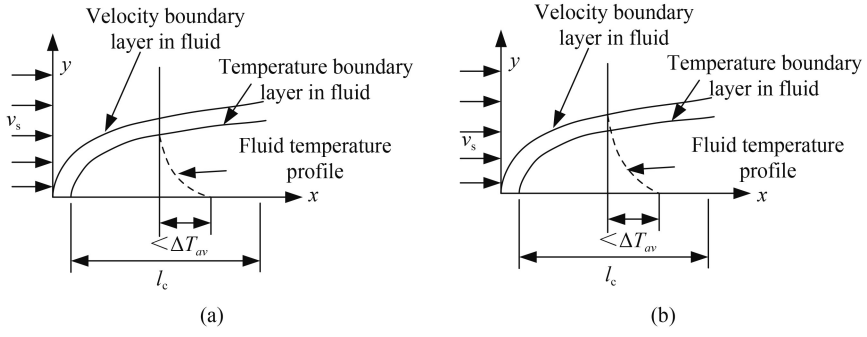

Fig. 40 (a) Laminar flow model or cooling on the grinding work surface. (b) Turbulent flow model for cooling on the grinding work surface.

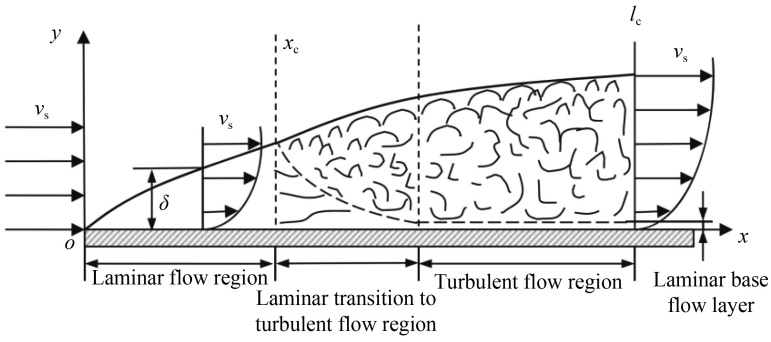

Fig. 41 Schematic of the process of boundary layer development in fluid swept flat plate flow [157].

due to high fluid velocity, approximating the boundary layer as being fully turbulent, the average heat transfer coefficient is calculated as follows:

$$\bar{h}_{\mathrm{f}} = 0.0247\frac{k_{\mathrm{f}}}{l_{\mathrm{c}}}Re^{4/5}Pr^{1/3}. \tag{132}$$

If the laminar flow section is not negligible and the combined laminar and turbulent flows are considered, then the average heat transfer coefficient along the grinding arc length for the mixed boundary layer is given as follows:

$$\bar{h}_{\mathrm{f}} = \frac{2k_{\mathrm{f}}}{3l_{\mathrm{c}}}\left[0.664Re^{1/2} + 0.037(Re_{\mathrm{lc}}^{4/5} - Re_{\mathrm{c}}^{4/5})\right]Pr^{1/3}. \tag{133}$$

The critical Reynolds number Re_{lc} is influenced by the degree of disturbance in the incoming flow and the roughness of the wall surface. During the grinding process, factors such as the jet pressure of the grinding fluid, the jet speed, the particle size of the grinding wheel, and the surface roughness of the workpiece all affect the value of the critical Reynolds number.

3.4.8 Based on statistical theory

During MQL grinding, surface heat transfer is highly nonlinear due to the large temperature gradient on the grinding surface, the complex kinematic characteristics of the spray, and the random distribution of droplet sizes [158,159].

In 2021, Yang et al. [143,160] investigated the atomization mechanism of nanofluid aerosol cooling and statistically analyzed the probability density of droplet sizes in the grinding zone. They used mathematical and statistical methods to analyze the effective heat transfer droplets within the nanofluid aerosol jet during grinding. Based on this analysis, a theoretical model for the CHTC of nanodroplets was established by calculating the heat transfer coefficients of the nanofluid jet and the accompanying high-pressure gas jet.

As shown in Fig. 42, when an aerosol droplet impinges on the grinding zone, it can rebound, diffuse, and splash. The rebound and crown droplet splash do not effectively contribute to heat transfer. The most effective heat transfer occurs when the droplet impinges on the surface of the heat source and diffuses along the surface, forming a liquid film. The critical Weber number that determines the effective droplet impact pattern is given by $2.0 \times 10^4 \times La^{-0.2} \leqslant We \leqslant 2.0 \times 10^4 \times La^{-1.4}$, where La is the Laplace number.

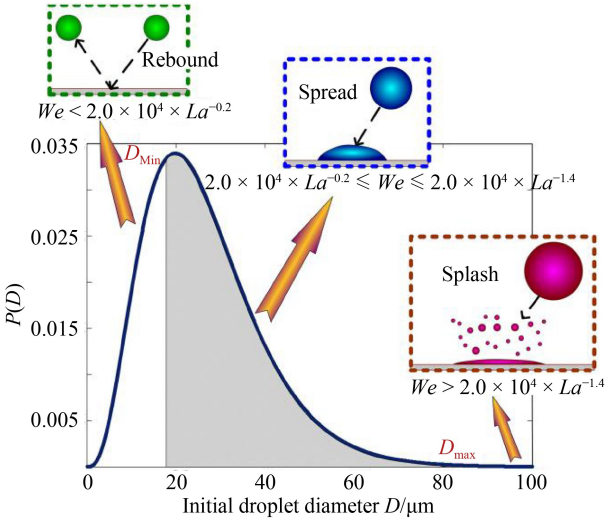

Fig. 42 Probability distribution of the mist droplets [160].

Assuming that the influence of the airflow around the grinding tool is overlooked, the velocity of the droplets hitting the solid surface can be taken as the velocity of the spray outlet. Based on the critical Weber number, the effective droplet diffusion size can be derived, that is, $D_{\min} \leqslant D \leqslant D_{\max}$, and the ratio of effective heat transfer droplets can be calculated as shown below.

$$P_{\mathrm{d}} = \int_{D_{\max}}^{D_{\min}} \frac{1}{6\overline{D}^4}D^3\exp\left(-\frac{D}{\overline{D}}\right)\mathrm{d}D. \tag{134}$$

For a single cooling droplet, the heat transfer coefficient h_s is presented below.

$$\begin{cases} J = c_f m_d \Delta T, \\ h_s = \dfrac{q_d}{\Delta T}, \\ J = q_s A' t_s, \end{cases} \tag{135}$$

where J is the amount of heat transfer for a single droplet, ΔT is the heat transfer temperature difference, q_d is the heat flow density of a single droplet heat transfer, t_s is the heat transfer time, m_d is the droplet mass, and A' is the diffusion area of the droplet.

By integrating over the effective region, the heat transfer coefficient for all effective heat transfer droplets is given by the following:

$$h_n = N_z \int_{D_{max}}^{D_{min}} \frac{h_s}{6\overline{D}^4} D^3 \exp\left(-\frac{D}{\overline{D}}\right) dD, \tag{136}$$

where N_z is the number of all droplets.

The CHTC of the gas introduced to high pressure $h_a = k_a \cdot Nu / b_c$, and the integrated CHTC for MQL cooling is as follows:

$$h_f = h_n + h_a. \tag{137}$$

Table 6 further summarizes the factors influencing the EDC in grinding operations.

Table 6 Modeling of CHTC coefficients in grinding processes

Model category	References	Basis of the model	Grinding wheel	Cooling condition	Cooling medium	Workpiece materials	Model accuracy
Considering the fluid boiling state	Yang et al. [143]	With nanofluid cooling, nanofluid convective heat transfer is the main heat transfer method under natural convection	Spherical diamond grinding tools	Spray cooling	SiO_2 nanofluid	Bovine femur	7%
	Zhang et al. [99]	CHTC reaches its maximum value at the end point of nucleate boiling heat transfer, that is, at the beginning of transition boiling heat transfer When the nanofluid is in film boiling, the endpoint of transition boiling marks beginning of film boiling	SiC vitrified bond grinding wheel	MQL	Base oil is KS-1008 synthetic grease, additive is Al_2O_3 nanoparticles as additive to prepare nanofluids	Ti–6Al–4V	–
	Liu et al. [144]	Based on the flow liquid film heat transfer law at the interface of the grinding wheel workpiece, the bubbles formed on the workpiece surface in the boiling state of the liquid film nucleus are assumed to be spherical in shape.	CBN grinding wheel	Dry grinding/low temperature cold air MQL	Lubricants	Ti–6Al–4V	8.5%–11.6%
	Mao et al. [145]	Starting from the atomization mechanism, based on the different heat transfer characteristics exhibited by the droplets at different wall temperatures	WA46	MQL spray lubrication	Aluminum oxide nanofluid	GCr15 bearing steel	–
Based on fluid mechanics	Gupta and Yadav [22]	Using a computational fluid dynamics approach	CBN grinding wheel	Wet grinding	Kerosene, water	Carbon Steel, Brass, Aluminum	–
	Yang et al. [146]	Based on fluid dynamics, the fluid is assumed to be turbulent	Spherical diamond grinding tools	NMQL	Hydroxyapatite nanofluids	bovine femur	6.5%
	Jin et al. [147]	Estimated using hydrodynamic and thermal simulations, assuming a uniform and constant workpiece surface temperature	Aluminum oxide grinding wheel	–	Water/mineral oil	–	–
	Lin et al. [148,149]	Derived from the coupling of fluid dynamics and heat transfer theory, based on solid heat transfer theory	Vitrified bond aluminum oxide grinding wheel	–	Water-based coolant	M50	3%–27%
Adoption of the backpropagation method	Jin et al. [150]	Based on the measured grinding temperature signal and the circular contact moving heat-source model, the EDC is inverted through the	Porous metal bond CBN grinding wheel	–	Oil-based grinding fluids	Nickel-based high-temperature alloys GH4169	–
	Gao et al. [151]	Analyze the grinding temperature using the analytical method, through the measurement of the temperature at different depths of the workpiece surface, to derive the temperature distribution of the object along the surface depth direction	Grinding disc	–	Water-based coolant	brass	–

(*Continued*)

Model category	References	Basis of the model	Grinding wheel	Cooling condition	Cooling medium	Workpiece materials	Model accuracy
Based on the Péclet number	Lavine and Jen [152]	The heat flow from the workpiece into the fluid is uniform, the fluid is stationary relative to the grinding wheel, and is observed as a moving "semi-infinite solid", based on a large Péclet number	Aluminum oxide/CBN grinding wheel	–	Water/mineral oil	Steel	–
	Vinay and Srinivasa Rao [153]	Based on motion characteristics during grinding	32A46-54J8VBE	Dry grinding/wet grinding	–	AISI D3 and AISI H13	5%
Differences in fluids in different areas of the grinding zone	Shen [154]	A grinding thermal model based on the finite difference method is used to analyze and explore different regions in detail	Vitrified bond aluminum oxide grinding wheel	MQL/wet grinding	Cimtech 500 synthetic grinding solution at 5 vol% concentration	Dura-Bar 100-70-02 ductile iron	–
Based on particle contact conditions	Zhu et al. [107]	Considering the effects of abrasive geometry, grain size, and grain concentration, the abrasive grains on the surface of the grinding wheel are assumed to be arranged in an orderly manner in a cross-array, and the abrasive grains are defined as cylinders with the same diameter as the grains	CBN grinding wheel	Dry grinding/wet grinding	Oil-based coolant	Ti–6Al–4V	7.5%–9.5%
Considering the fluid flow state	Zhang and Rowe [155,156]	Based on the different flow states of fluids, laminar flow, turbulent flow, and fluid grinding wheels as a whole are studied separately in three states	Green SiC grinding wheel	Wet grinding	Oil/water emulsion	Cemented carbide YG6	–
	Wang [157]	System of differential equations for convective heat transfer and definite solution conditions to express convective heat transfer problems	Green SiC grinding wheel	Wet grinding	Water-based coolant	Cemented carbide YG6	2.0%–2.7%
Based on statistical theory	Yang et al. [160]	Analysis of effective heat transfer droplets in the grinding zone of nanofluid aerosol jets using mathematical and statistical methods	–	–	SiO_2–saltwater nanofluid	Chemical vapor deposition diamond	7.26%

4 Application of heat transfer process parameters modeling

4.1 Energy distribution coefficient

Rowe [84] investigated the energy distribution and temperature prediction in the grinding process using CBN and alumina grinding as examples. By comparing two different models and demonstrating the sensitivity of important parameters, the abrasive grain model aligns more closely with the underlying reasoning.

The experimental results show that the thermal contact coefficients, derived indirectly from the grinding experiments, are notably lower than the performance values obtained from direct measurements. Therefore, the effective values obtained by correlating the theoretical model with the grinding experiments are lower, while the abrasive grain model demonstrates better agreement between the theoretical and experimental values of thermal performance.

Qiu et al. [89] studied the grinding heat transfer process in thread profile grinding and analyzed the process using two EDC models for two distinct grinding regions. One model uses a single-particle energy distribution, while the other uses an energy distribution model at the abrasive grain–workpiece interface. At $a_p = 0.005$ mm, the energy distribution to the ground workpiece reaches 76.5% and 84.4% for the AB and BC surfaces (Fig. 11), respectively. The thermal partition R_w(AB) is approximately 8%–9% lower than R_w(BE), which is due to the better heat dissipation conditions in the AB plane compared to the BE plane.

In 1999, Guo et al. [86] developed a numerical calculation model for profile grinding temperature based on the distribution of heat sources in right-angled triangles within the grinding arc and the simplification of the one-dimensional heat conduction process. This model was further supported by the theoretical analysis of continuous grinding temperature on a plane. After conducting numerous grinding tests with conventional aluminum oxide abrasives and CBN grinding wheels, and using different fluids (including soluble oil, cold air, and ester oil), the temperature rise of the workpieces under conventional and creep-feed conditions was measured. The energy distribution was obtained by measuring the temperature, integrating the positive heat flow

density, and dividing by the grinding power. Notably, the results indicate that the energy distribution is influenced by grinding conditions, the type of abrasive, and the application of the fluid, all of which can be quantitatively considered by using a single-grain thermal model.

Ding et al. [98] investigated the temperature and energy distribution in the cylindrical grinding process under various process parameter and thermophysical conditions through finite element simulation and experimental validation. The results revealed that the effect of workpiece rotational speed on the energy distribution to the chip is more pronounced than that of other grinding parameters. The rational selection of grinding parameters can notably reduce the energy distribution into the workpiece, from 80% to a range of 30%–50%, or even lower. The variation in the energy distribution ratio under different process parameters is shown in Fig. 43.

Wang et al. [161] determined the heat flow density of the workpiece using the finite difference method, based on measurements of the grinding force and grinding temperature, which allowed them to obtain the energy distribution. As shown in Fig. 44, the results indicate that the feed rate has a more substantial effect on grinding temperature and energy distribution compared to other factors. An increase in feed rate reduces the machining temperature but results in a considerably higher energy distribution. Studies have revealed that the energy distribution in dry grinding is approximately 5% when grinding the titanium alloy material TC4 with a vitrified bond CBN grinding wheel.

Hadad et al. [95] investigated the temperature and energy distribution in the MQL grinding process. The thermal performance of MQL grinding was analyzed and compared with dry grinding and fluid grinding. The results, shown in Tables 7 and 8, indicate that the energy distribution for MQL grinding with Al_2O_3 grinding wheel ranges from 73% to 77%, whereas the energy distribution for dry grinding is approximately 82%. In fluid grinding with Al_2O_3 grinding wheels, the cooling effect of the fluid in the contact zone reduces the energy distribution to less than 36%. By contrast, grinding with CBN grinding wheels results in a notably lower energy distribution to the workpiece due to the thermal conductivity of the CBN material, which is 46% in combination with MQL, 52% in dry grinding, and 14% in fluid grinding.

Zhan and Xu [162] conducted an experimental study on the temperature and energy distribution in grinding carbide with vacuum-brazed diamond grinding wheels. The effects of grinding conditions such as grinding wheel speed, feed rate, and depth of cut on the grinding temperature and energy distribution are shown in Fig. 45. The results indicate that the grinding temperature measured under different grinding conditions ranged from 10 to 100 °C. The energy distribution of dry grinding to the workpiece was between 35% and 70%.

Li et al. [163] used nanofluids prepared from different vegetable oils as base oils for high-

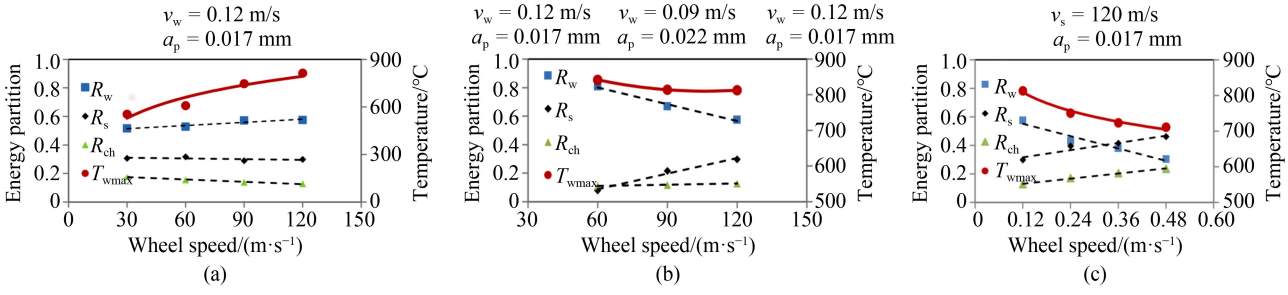

Fig. 43 (a)–(c) Variation of energy partition and temperature with different parameters [98].

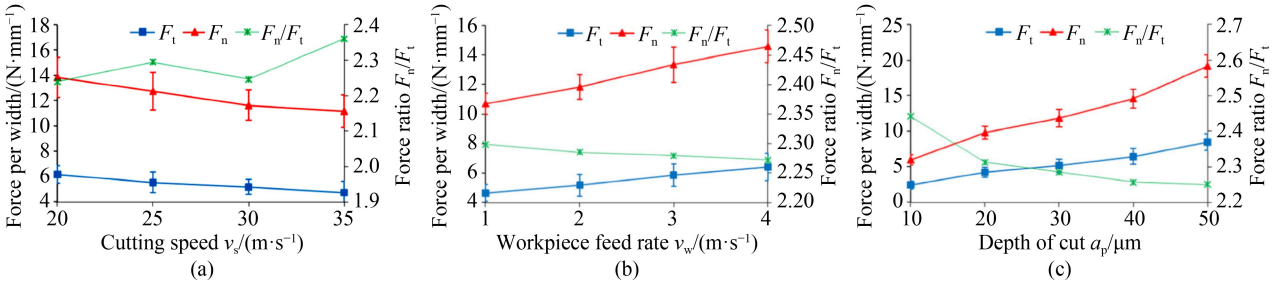

Fig. 44 Influence of grinding parameters on grinding forces and force ratio: (a) grinding speed; (b) workpiece feed rate; (c) depth of cut [161].

Table 7 Experimental results during grinding with Al_2O_3 grinding wheels

Test	F_t/N	F_t/F_n	R_w	T_{max}/°C
Dry	20.0	0.40	0.82	218
MQL(1)	17.3	0.36	0.77	169
MQL(2)	16.0	0.33	0.75	163
MQL(3)	14.8	0.31	0.77	152
MQL(4)	12.5	0.28	0.75	123
MQL(5)	10.5	0.25	0.73	105
Fluid	12.5	0.30	0.36	55

Table 8 Experimental results during grinding with CBN grinding wheels

Test	F_t/N	q_w	R_w	T_{max}/°C
Dry	18	3.2188×10^6	0.52	131
MQL(1)	16	2.7765×10^6	0.48	113
MQL(4)	15	2.6533×10^6	0.46	108
Fluid	15	7.8627×10^5	0.14	32

temperature nickel-based alloy MQL grinding experiments and compared the energy proportionality coefficients of seven vegetable oils for MQL grinding. The results are shown in Fig. 46, where castor oil-based MQL grinding demonstrates the highest energy proportion factor, while palm oil-based MQL grinding exhibits the lowest energy proportion factor. The results for the other five vegetable oils were similar, with values in between the above two. Palm oil is the best base oil for MQL grinding with an EDC of 42.7%.

Li et al. [164] conducted experiments on the efficient deep grinding of nickel-based high-temperature alloys using porous metal-bonded CBN supergrinding wheels to study the energy distribution to the workpiece during grinding. The results show that the energy distribution values for porous metal-bonded CBN grinding wheels generally range from 2% to 6%, which is lower than that of conventional vitrified CBN grinding wheels and alumina grinding wheels. In comparison, the energy distribution to the workpiece for conventional vitrified CBN grinding wheels ranges from 4% to 8%, while for conventional alumina grinding wheels, this distribution ranges from 25% to 65%.

Hou and Yao [165] studied the grinding process using fluted grinding wheel grindings and modeled the temperature distribution of the workpiece under conditions of periodic heat-source variation. As shown in Fig. 47, the experiment shows that R_w increases with the feed rate, while R_f decreases as the feed rate increases. The R_w for slotted grinding wheels is higher than that of non-slotted grinding wheels at feed rates ranging from 400 to 2000 mm/min. Additionally, the R_f for slotted grinding wheels is lower than that for non-slotted wheels. The heat flow density transferred to the coolant when the grinding wheel is slotted is not greater than that when the grinding wheel is not slotted.

Jin et al. [108] analyzed the heat transfer mechanism in involute gear form grinding, considering

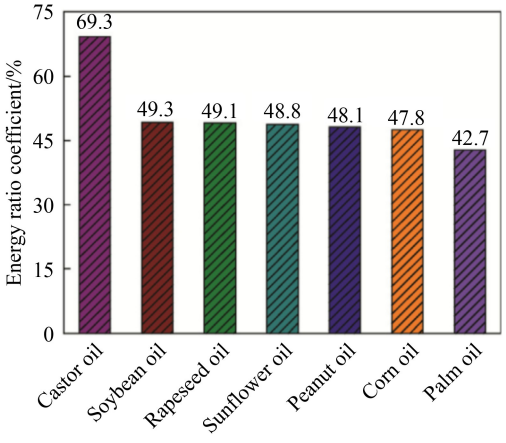

Fig. 46 Ratio coefficients of energy transferred into workpieces for the seven kinds of vegetable oil used in MQL grinding [163].

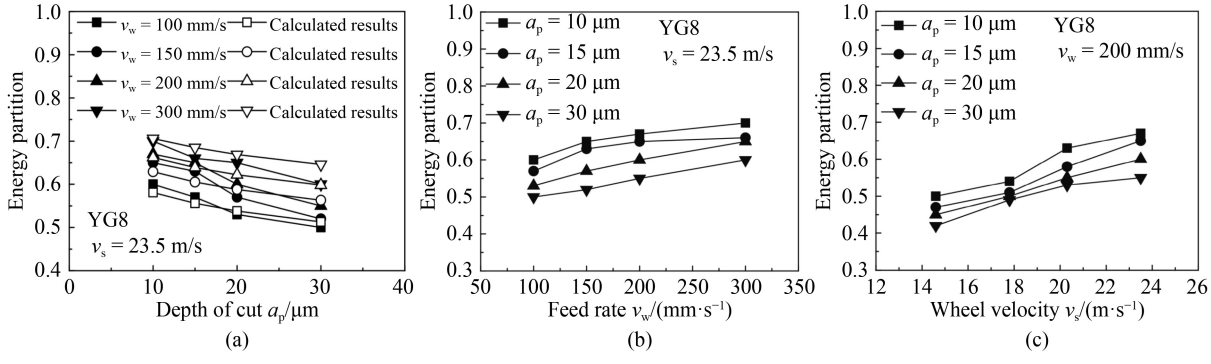

Fig. 45 Variation of energy partition as a function of (a) depth of cut (v_s = 23.5 m/s), (b) feed rate (v_s = 23.5 m/s), and (c) wheel velocity (v_w = 200 m/s) [162].

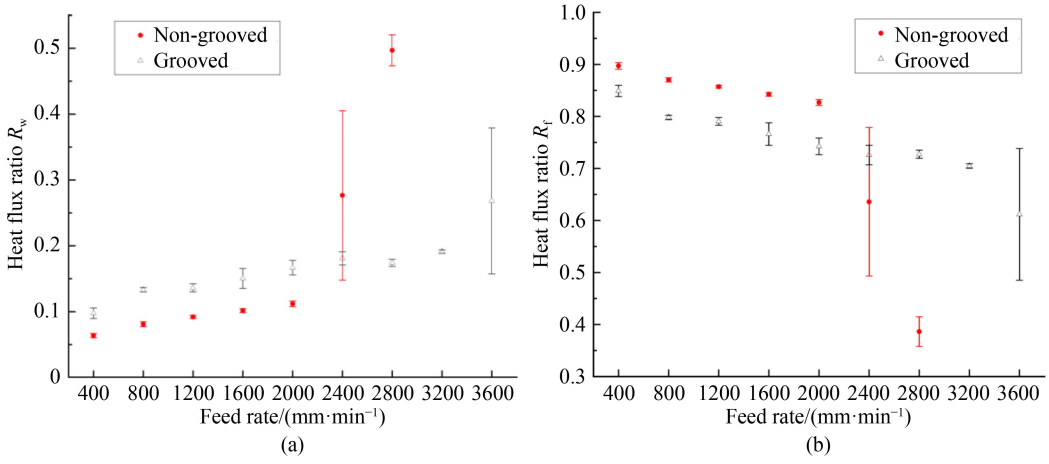

Fig. 47 (a) Heat flux ratio R_w with grooved and non-grooved wheels. (b) Effects of coolant with grooved and non-grooved wheels on R_f [165].

and analyzing in detail the variation in tooth contact geometry. The heat effect on the involute tooth form was investigated using a transient, non-uniform heat-source moving along a three-dimensional curved shape. The distribution of the energy distribution ratio of the workpiece along the involute contact profile under dry grinding conditions, with different grinding depths and table speeds, is shown in Fig. 48.

Overall, the energy distribution along the involute contact profile, from root to tip, gradually decreases under dry grinding conditions and varies with the grinding parameters. Increasing the grinding depth and table speed helps reduce the energy distribution.

Pang et al. [166] investigated thermal models in the grinding zone by analyzing dry and wet cylindrical plunge grinding. In studying the EDC coefficient of energy distribution, the effect of CHTC coefficient was considered. The analysis was conducted using two energy distribution models: R_{ws} and R_{wch} for workpiece–grinding wheel and the workpiece–chip, respectively. The results show that v_f and a_p have substantial effects on R_w, while v_s has minor effects on R_w. Specifically, R_w decreases with increasing v_f and increases with rising a_p.

Zhu et al. [107] proposed an improved temperature calculation model that considers the geometry and distribution of abrasive grains, as well as the workpiece–wheel energy distribution ratio, considering the effect of the cone angle during the machining process. Experimentally, the effective contact radius of abrasive grains was found to substantially influence the workpiece–wheel distribution ratio. As shown in Fig. 49(a), when $r_0 < 15$ μm, the predictions of the two models are similar; however, as r_0 continues to increase, the two models show considerable differences. Regarding the effect of abrasive geometry, the cone angle also has a substantial influence on the workpiece–wheel distribution ratio. As shown in Fig. 49(b), at a depth of cut of 5 μm, the R_{ws} value

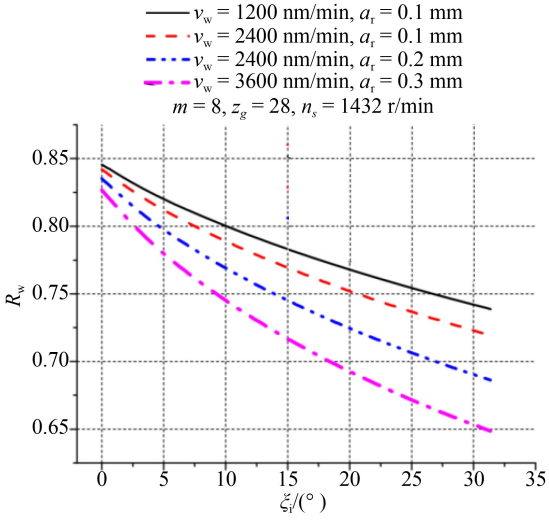

Fig. 48 R_w distributions along the ground tooth profile [108].

increases almost linearly with the taper angle in the range of 90°–170°. As the depth of cut increases, especially beyond 25 μm, the sensitivity of R_{ws} to depth decreases.

Peng et al. [96] investigated the height of the grinding chip energy distribution ratio and its variation in the high-speed grinding process of nickel-based alloys, analyzing changes in the energy distribution mechanism under wet and dry grinding conditions were studied. As shown in Fig. 50, which presents the ratio of grinding temperature and energy distribution to the workpiece, as well as the heat flow and heat transfer coefficients under identical grinding conditions, the grinding temperature at v_s = 80 m/s is substantially higher than at higher wheel speeds. This finding indicates that the energy distribution mechanism at v_s = 80 m/s differs markedly from that at higher wheel speeds, possibly due to the presence

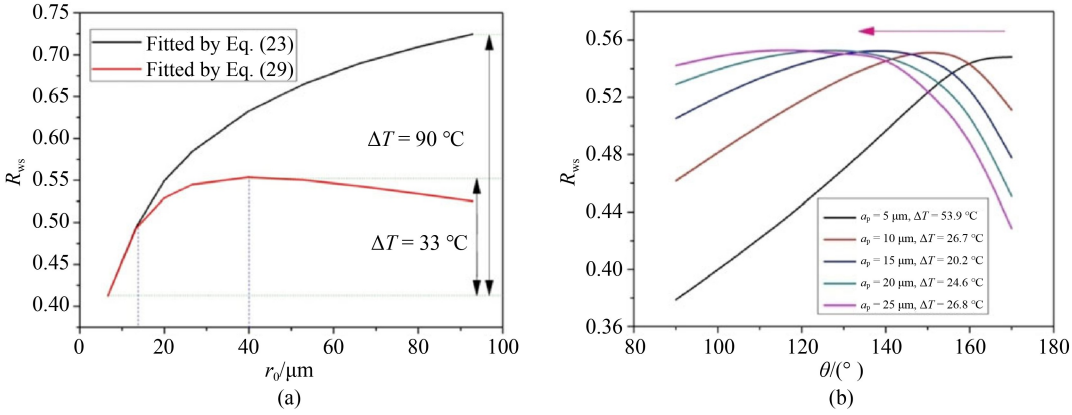

Fig. 49 Workpiece–grinding wheel distribution ratio: (a) taper angle of 106°, varying with depth of cut; (b) depth of cut of 5–25 μm, varying with taper angle [107].

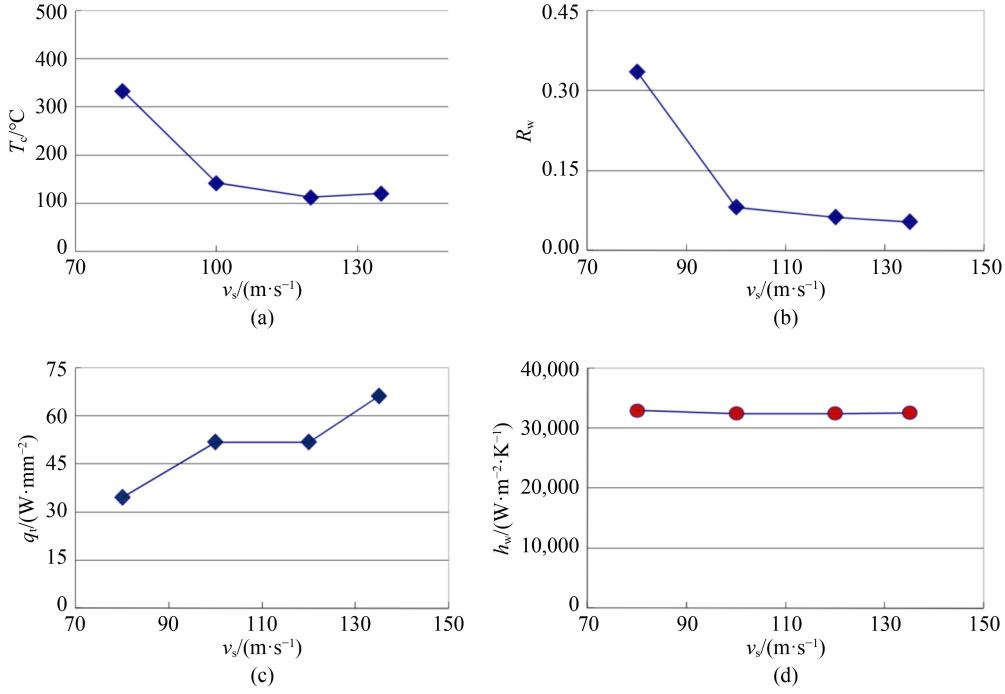

Fig. 50 (a) Measured grinding temperatures, (b) estimated heat partition ratio, (c) total grinding heat flux, and (d) heat conduction factor under different wheel speeds (v_w = 6 m/min, a_e = 0.03 mm, and l_c = 3.46 mm) [96].

of burnout of the grinding fluid or film boiling occurring once the threshold temperature is exceeded.

The conclusions show that under wet grinding conditions, high-speed grinding increases the CHTC and reduces the energy distribution indications. However, when the temperature exceeds the combustion threshold temperature associated with membrane boiling, the fluid has difficulty in wetting and cooling the heated surfaces in the grinding region. This behavior is similar to dry grinding condition, leading to notable increase in the EDC of the workpiece. Under "dry" grinding conditions, approximately 30%–40% of the grinding heat is carried away by the grinding debris.

Zheng et al. [111] established an improved external wet grinding temperature model that accounts for the lubrication effect of the grinding fluid and solved it numerically. They studied and compared the temperature variation of alloy steel during cylindrical wet grinding under different grinding process parameters, considering the lubrication effect. Experimental results show that the value of q_w with lubrication is larger than that without lubrication, and the difference between the two gradually increases with v_s. The value of q_w is directly proportional to the total grinding heat flow q_t of the workpiece and the energy distribution ratio R_w, as shown in Fig. 51.

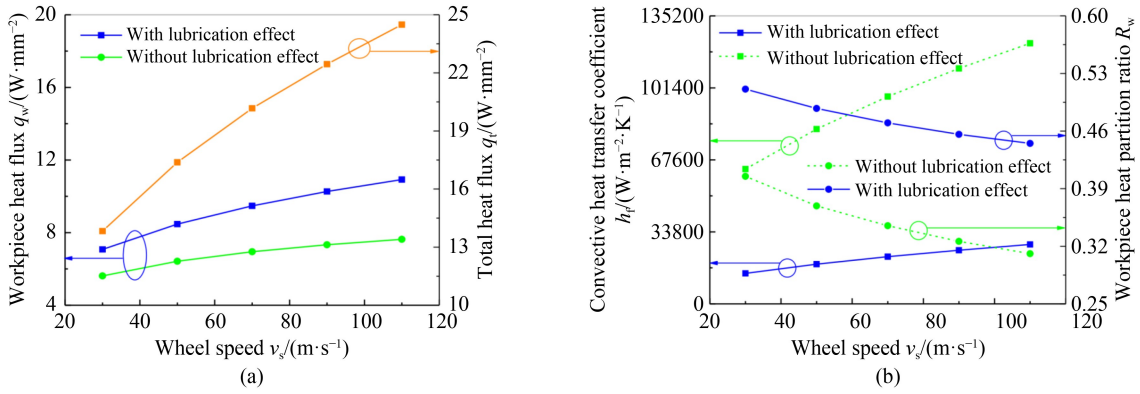

Fig. 51 Grinding process parameters at varying grinding wheel speeds: (a) heat flux into the workpiece and total grinding heat flux; (b) CHTC and heat partition ratio of the workpiece [111].

As shown in Fig. 52, the energy distribution ratio R_w is higher for a lubricated workpiece compared to one without lubrication. This finding indicates that, under lubricated conditions, a greater portion of the grinding heat flow q_w enters the workpiece, resulting in higher grinding temperatures.

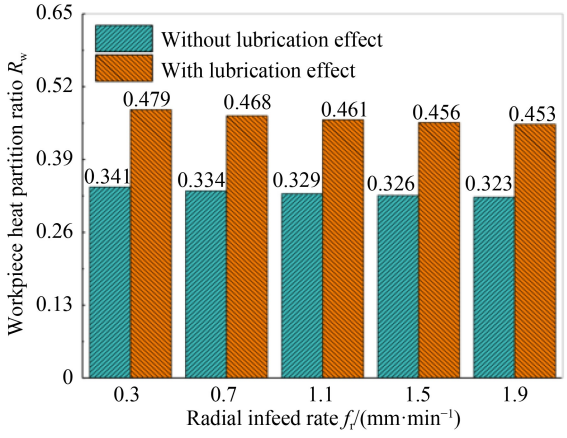

Fig. 52 Heat partition ratio of workpiece at varying radial infeed rate [111].

Lavine et al. [116] analyzed the grinding wheel surface in the grinding zone by approximating it as a thermal composite material comprising abrasive grains and grinding fluid within its pores. The energy distribution was calculated by modeling the grinding zone as a rectangular band of heat sources moving at the working speed along the wheel surface. The study concluded that the thermal properties of this composite solid are difficult to specify and are highly sensitive to the porosity of the grinding wheel near the workpiece surface.

Therefore, Kim et al. [113] investigated the heat flow density and energy distributions of the workpiece during creep-feed grinding

Ren et al. [167] analyzed and modeled the dynamic energy distribution in belt grinding, considering the dynamic characteristics of belt grinding in terms of grinding effect and heat. The thermal characteristics of the system were obtained using a combination of the finite element method and an optimization algorithm. The dynamic energy distribution during continuous grinding was then calculated using an iterative method that considers the heat accumulation effect in the workpiece.

Validation was conducted using SUS304 and AA6061-T6 workpieces, and the results demonstrate the effectiveness of the proposed method for calculating dynamic energy distribution. For the SUS304 workpiece, the validation results are shown in Figs. 53(a) and 53(b), where the maximum percentage error in the calculated q_w is 14.3%, and the maximum error between the calculated and measured temperatures is less than 32.4 ℃. In comparison, for the AA6061-T6 workpiece, the validation results are presented in Figs. 53(c) and 53(d), with the calculated grinding temperature closely following the trend of the measured temperature and a maximum error of 17.18 ℃.

The dynamic energy distribution for the SUS304 workpiece is shown in Fig. 53(e), while the results for the AA6061-T6 workpiece are shown in Fig. 53(f). The results indicate that, unlike traditional grinding with wheel grinding, the mechanical properties of the workpiece in belt grinding substantially influence the energy distribution and the material removal mechanism. As grinding proceeds, the grinding temperature softens the workpiece, making material removal easier. Simultaneously, heat accumulation in the abrasive grits reduces the cooling capacity of the belt.

Mohamed et al. [168] improved the estimation of energy distribution during grinding using surface roughness measurements. Their experimental findings demonstrated that surface roughness can serve as an effective indicator for estimating particle radius. The average difference between the energy distribution predicted using this model and the conventional

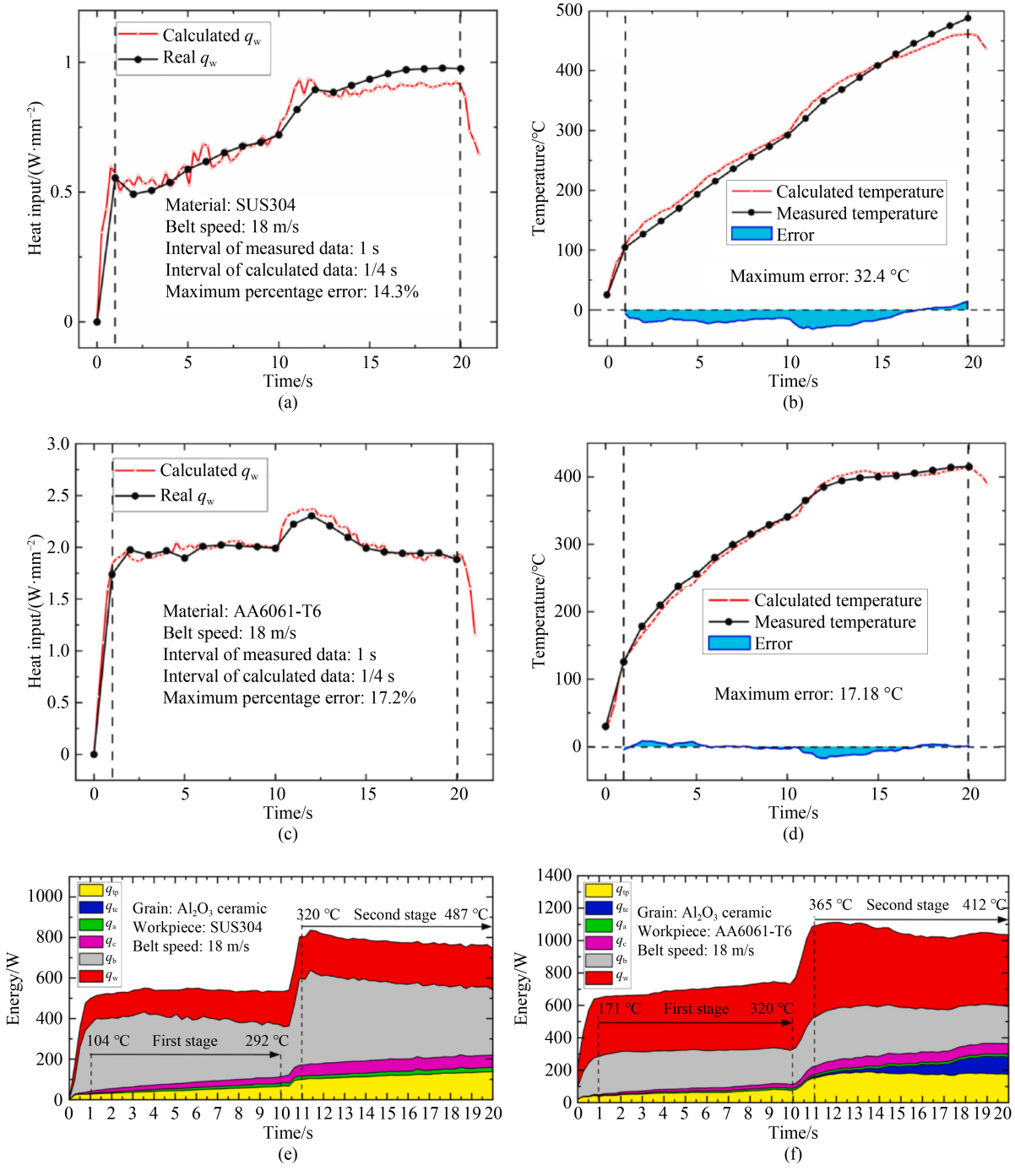

Fig. 53 Validation results for SUS304 workpiece: (a) heat input and (b) grinding temperature. Validation results for AA6061-T6 workpiece: (c) heat input and (d) grinding temperature. Energy partition for (e) SUS304 and (f) AA6061-T6.

method was 7.5%. The results, showing the relationship between energy distribution and surface roughness under three different dressing conditions, are plotted in Fig. 54. Additionally, the energy distribution values calculated using this method are compared to those derived from the traditional trial-and-error method.

Table 9 further summarizes the factors influencing the EDC in cutting and grinding machining.

4.2 Convective heat transfer coefficient

Liu et al. [144] analyzed the flow liquid film heat transfer law at the interface of grinding wheel–workpiece with low-temperature cold air MQL, based on the evolution law of the physical properties

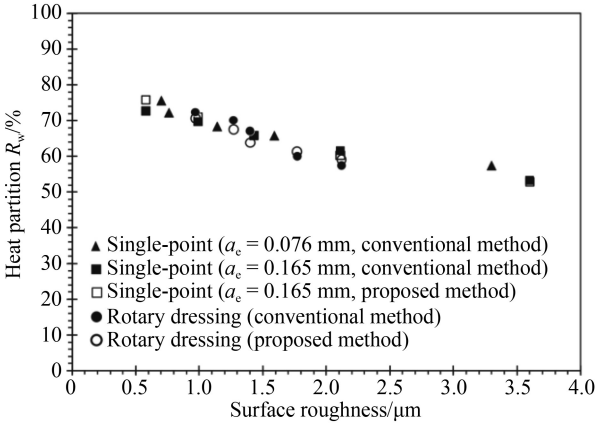

Fig. 54 Comparison of heat partition *vs.* surface roughness for conventional and proposed methods.

of the lubricant and the liquid film heat transfer mechanism in the grinding zone. They also conducted verification experiments on the flow liquid film CHTC and the heat transfer performance of low-temperature cold air MQL for grinding titanium alloy. The results show that, under the same lubricant flow rate, the flow liquid film CHTC h_f increases as the cold air temperature decreases. Under different cold air temperatures, the theoretical calculated value of the heat transfer coefficient h_f is generally consistent with the actual measured value, with the model error ranging from 8.5% to 11.6%.

The theoretical value of CHTC coincides with the measured value, with an error of 8.5% when the cold air temperature is −10 ℃. Additionally, the experimental surface temperature value of the workpiece coincides with the trend of the theoretical value, with

Table 9 Factors influencing the EDC

Reference	Processing tool	Workpiece materials	Cooling method	Coolant	Influencing factor	Processing parameters			Conclusion
						v_s/(m·s^{-1})	v_w/(m·s^{-1})	a_p/mm	
Rowe [84]	Aluminum oxide grinding wheel/CBN grinding wheel	AISI52100 /AISI1055	Wet grinding	TRIM VHP E200 2%	Depth of grind, porosity, contact area	30	0.3		Granular modeling is more appropriate than holistic modeling
Qiu et al. [89]	SG	9Mn2V	Dry grinding	–	Grinding depth, grinding area	27	15	0, 005, 0.01, 0.02	The energy distribution of the ground workpiece reached 76.5% and 84.4% for the AB and BC surfaces, respectively
Guo et al. [86]	Aluminum oxide grinding wheel/CBN grinding wheel	Si_3N_4	Wet grinding	Soluble oils, cold air and ester oils	Machining parameters, thermal properties of abrasives and workpieces, and cooling effect of fluids in the grinding zone	30, 60	150	25, 200, 500	Conventional grinding with resin and CBN-coated grinding wheels has a lower energy distribution ratio than conventional grinding with alumina grinding wheels, which can be reduced to an even lower level with the use of water-based fluids
Ding et al. [98]	Vitrified bond CBN grinding wheel	9Mn2V	Dry grinding	–	Grinding depth, workpiece speed	30, 60, 90, 120	0.12, 0.06, 0.09, 0.24, 0.36, 0.48	0, 017, 0.033, 0.022	The influence of the workpiece speed on the energy distribution to the chip is more pronounced than other grinding parameters. Proper selection of grinding parameters notably reduces the energy distribution into the workpiece from 80% to 30%–50% or even lower
Wang et al. [161]	CBN grinding wheel	Titanium alloy TC4	Dry grinding	–	Grinding wheel speed, depth of cut and workpiece feed rate	20, 25, 30, 35	1, 2, 3, 4 m/min	10, 20, 30, 40, 50 μm	Feed rate has a more substantial effect on grinding temperature and energy distribution than grinding speed and depth of cut
Hadad et al. [95]	Aluminum oxide grinding wheel/CBN grinding wheel	100Cr6 steel	Dry grinding/MQL/wet grinding	Water-based MQL, Oil-based MQL	Types of abrasives and types of coolant	30	2000 mm/min	30 μm	The high thermal conductivity of CBN grinding wheels can effectively reduce the EDC, and the effect of fluid cooling is stronger than that of MQL
Zhan and Xu [162]	Diamond grinding wheels	Cemented carbide YG8	Dry grinding	–	Grinding wheel speed, depth of cut, and workpiece feed rate	14.6–23.5	100–300 mm/s	10–30 μm	Temperature increases with cutting speed and depth of cut and decreases with increasing feed Approximately 35%–70% of the total grinding energy is transferred to the workpiece in the form of heat in the grinding zone

(*Continued*)

Reference	Processing tool	Workpiece materials	Cooling method	Coolant	Influencing factor	Processing parameters			Conclusion
						v_s/(m·s^{-1})	v_w/(m·s^{-1})	a_p/mm	
Li et al. [163]	Corundum grinding wheel	High temperature nickel-based alloys GH4169	MQL	Castor, soybean, rapeseed, corn, peanut, palm and sunflower oil-based MQL	Lubricant type	30	3000 mm/min	10 μm	Castor oil had the highest energy scaling factor, palm oil had the lowest energy scaling factor, and the other five vegetable oils had similar energy scaling factors
Li et al. [164]	Porous metal Bond CBN grinding wheel	High temperature nickel-based alloys Inconel 718	Wet grinding	4% water-based emulsion	Grinding wheel speed, workpiece speed, depth of cut, grinding wheel particle porosity	30–120	600–3600 mm/min	0.1–1 mm	The range of energy distribution of grinding wheels using porous metal-bonded CBN is smaller than that of conventional vitrified CBN and aluminum oxide grinding wheels
Hou and Yao [165]	Grooved and ungrooved grinding wheel	42CrMo	Wet grinding	Water-based coolant (95% water and 5% cutting fluid; Syntilo 9954)	Grinding wheel, grooving conditions	25	400, 800, 1200, 1600, 2000, 2400, 2800, 3200, 3600 mm/min	20 μm	R_w increases with feed rate, R_f decreases with increasing feed rate, and the heat flow density transferred to the coolant when the grinding wheel is grooved is not greater than when the wheel is not grooved
Jin et al. [108]	SG grinding wheel	20CrMnTi	Dry grinding	–	Grinding parameters	1910 r/min	1200, 2400, 3600 mm/min	0.1, 0.2, 0.3	The energy distribution ratio decreases along the involute contact profile, from tooth root to tooth tip, and varies with the grinding parameters. Increasing the grinding depth and table speed is beneficial for reducing the energy distribution
Pang et al. [166]	Diamond grinding wheels	SiC	Dry grinding/ wet grinding	–	Actual contact length, number of active abrasive grains and effective contact radius	20, 60, 100, 140,	0.1	0.008	The effects of v_f and a_p on R_w are substantial, the effect of v_s on R_w is minimal, and R_w decreases with increasing v_f
Zhu et al. [107]	CBN grinding wheel	AISI52100	Wet grinding	Mineral oil	Taper Angle, grain size, and grain concentration	60	0.24	0.017	The taper angle and the effective contact radius of the abrasive grits have a strong influence on the workpiece–wheel distribution ratio
Peng et al. [96]	CBN grinding wheel	nickel-based alloy GH4169	Wet grinding	5% water-based emulsion SY-1	Grinding parameters	80, 100, 120, 135	1, 3, 6, 9, 12, 15	0.03, 0.05, 0.08	At high grinding speeds, the higher CHTC of the grinding fluid allows for effective heat transfer to the workpiece. Burnout occurs when the CHTC drops to zero, and the ratio of energy between the workpiece and the grinding chips will be notably higher
Zheng et al. [111]	Aluminum oxide grinding wheel	9310 alloy steel	Wet grinding	Castrol 981	Whether or not coolant is used	90	20 r/min	1.5 mm/min	The energy distribution ratio R_w is greater for a workpiece with lubrication than for a workpiece without lubrication
Li et al. [116]	Aluminum oxide grinding wheel	–	Wet grinding	–	Coolant heat transfer performance, grinding wheel porosity	20	0.1	0.01	Excellent agreement with published data on conventional and creep-feed grinding
Ren et al. [167]	Belt grinding	SUS304/A A6061-T6	Dry grinding	–	Mechanical properties of workpiece, grinding temperature, and grinding time	–	–	–	The mechanical properties of the workpiece in belt grinding have substantial effects on the energy distribution and the material removal mechanism. Energy distribution is influenced by workpiece material, grinding temperature, and grinding time

(*Continued*)

Reference	Processing tool	Workpiece materials	Cooling method	Coolant	Influencing factor	Processing parameters			Conclusion
						v_s/(m·s^{-1})	v_w/(m·s^{-1})	a_p/mm	
Mohamed et al. [168]	Aluminum oxide grinding wheel	AISI 1018 steel	Dry grinding	–	Roughness of grinding wheel	–	–	–	The average difference between the predicted heat distribution and that predicted by the traditional trial-and-error method was 7.5%

an error of 7.7% when the grinding depth is 30 μm and the cold air temperature is −40 ℃.

Gupta and Yadav [22] used the research method of fluid dynamics to establish a mathematical model for the convective CHTC of grinding fluids. Through experimental and simulation studies under different grinding conditions, they derived the trends of grinding parameters and the influence of the grinding fluid's density, specific heat, conductivity, and viscosity on the changes in CHTC. Experiments were conducted using two grinding fluids at different grinding wheel speeds and grinding depths, and the results indicated that the CHTC of the grinding fluids increases with the speed of the grinding wheel and decreases with the depth of cut. Additional experiments were conducted under the same conditions by separately controlling the differences in the density, specific heat, conductivity, and viscosity of the grinding fluid. The results showed that changes in specific heat had a small effect on the coefficient, while changes in viscosity and conductivity had a substantial effect on the coefficient. The CHTC coefficient increased with the concentration, specific heat, and conductivity of the grinding fluid, and decreased with the viscosity of the grinding fluid.

Lin et al. [148,149] described the heat transfer in the grinding region under different grinding conditions based on fluid dynamics and heat transfer theory. Grinding experiments were conducted on two material powders separately, and the results are shown in the table. Notably, the CHTC values can be remarkably high, substantially exceeding those previously reported. As shown in Fig. 55, the experimental results indicated that the values of CHTC varied with process parameters, such as the actual depth of cut and wheel speed, and decreased as the contact length increased.

Jin et al. [147] used fluid dynamics and thermal simulations to investigate and estimate the CHTC in the grinding zone. They concluded that the CHTC is determined by the grinding wheel speed and the liquid film thickness in the contact zone, which is, in turn, affected by factors such as the grinding wheel speed, porosity, particle size, coolant type, flow rate, and nozzle size.

The grinding temperatures for deep grinding and shallow grinding were calculated based on the estimated CHTC values and compared with the actual grinding temperatures.

Jin et al. [150] used the inverse method to investigate the fluid CHTC in the grinding zone under deep-cut grinding conditions by measuring the temperature in the grinding zone with the help of the EDC. The experiment showed that the distribution pattern of CHTC in the grinding zone under slow-in deep-cut mode is notably different from that of conventional shallow grinding. The distribution of CHTC in the grinding zone is divided into two curves: in the small interval at the front end of the grinding zone, the grinding fluid CHTC exhibits an obvious upward section, while in the main convective heat transfer zone, the CHTC change is relatively flat. The contact arc length and feed rate have minimal influence on the CHTC of the main convective heat transfer zone, with grinding speed being the main factor.

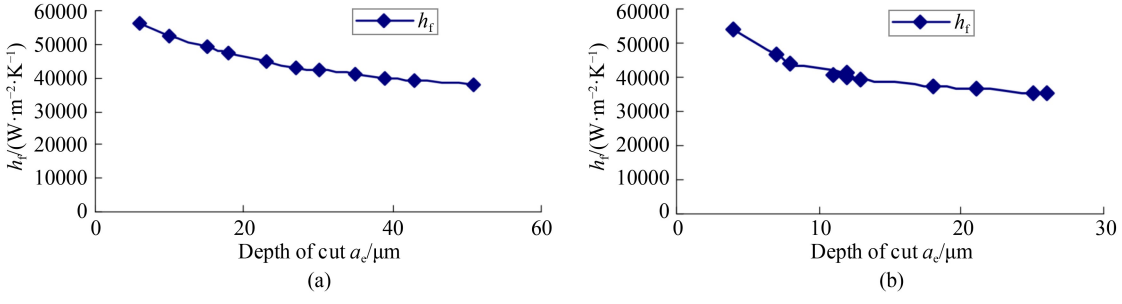

Fig. 55 (a) Effect of depth of cut on the convection heat transfer coefficient (cast iron tests). (b) Effect of depth of cut on the convection heat transfer coefficient (M50 tests) [148,149].

Gao et al. [151] experimentally determined the CHTC and its distribution in the contact zone between the grinding wheel and workpiece during vertical axis surface grinding. Based on heat conduction theory and a large number of experimental results, the grinding temperature follows a parabolic distribution along the depth direction. The CHTC was determined by inverting the model and using the three-point method to measure the surface temperature of the workpiece.

The CHTC within the contact area between the vertical axis plane grinding wheel and the workpiece is unevenly distributed. In dry grinding, the coefficient demonstrates minimal variations, whereas in wet grinding, substantial changes occur at different locations on the contact surface of the grinding wheel. The installation height of the cooling nozzle has a greater impact on the cooling effect. Additionally, the coolant flow rate notable affects h. When the flow rate is small, the effect is more pronounced. However, once the flow reaches a certain value, the cooling heat transfer coefficient increases slowly; that is, the coolant flow rate is too small, the cooling effect is poor, while excessive flow rate leads to waste.

Shen [154] estimated the CHTC using a grinding heat model based on the finite difference method. The accuracy of the model was verified by comparison with the traditional semi-infinite workpiece grinding heat model. The results showed that the effects of free convection and leading-edge cooling are negligible, while trailing-edge cooling only affects the trailing-edge region. The model was further applied to analyze convective cooling in grinding experiments. The estimated average CHTC in the grinding contact zone was approximately 4.2×10^5 W/(m^2·K) for wet grinding and approximately 2.5×10^4 W/(m^2·K) for MQL grinding, whereas the estimated CHTC at the trailing edge was notably lower.

By matching the measured temperature distributions with those calculated by the FDM heat transfer model, the CHTC within the grinding zone (h_{contact}) and at the trailing edge (h_{trailing}) can be obtained. The CHTC in the contact zone is higher than at the trailing edge due to the high flow rate. Additionally, the CHTC in wet grinding is notably higher than in MQL grinding for the contact zone and trailing edge. The results for the trailing edge in wet grinding show good agreement, whereas the results for MQL grinding at the trailing edge do not match well due to the low flow rate.

Zhu et al. [107] proposed an improved temperature calculation model considering the abrasive grain geometry and distribution. Assuming that the abrasive grains on the surface of the grinding wheel are arranged in an orderly manner in a cross-array, an experimental study was conducted to accurately assess the effect of abrasive grain geometry (cone angle, grain size, and grain concentration) on the CHTC.

Notably, increasing the cone angle leads to a reduction in the CHTC, as shown in Fig. 56(a), which can be illustrated by the increasing Reynolds number with the rising cone angle. As shown in Fig. 56(b), a large abrasive grain size leads to a small CHTC. This phenomenon is due to the large grinding wheel size, which results in a smaller corresponding grinding wheel pitch than the finer grinding wheel, making it difficult for the coolant to penetrate into the gap between the grinding wheel and the workpiece. This condition results in an increase in the Reynolds number and a decrease in the CHTC. As shown in Fig. 56(c), a high abrasive grain concentration leads to a low CHTC. This finding is equivalent to Fig. 56(b), where a small abrasive spacing results in a high Reynolds number, leading to a small CHTC.

Zhang and Rowe [155] investigated the modeling of CHTC for different fluid states and compared the experimental values with the predicted values. They compared the predictions of the laminar flow model with the experimental results, as well as those of the fluid wheel model. The CHTC predictions from the turbulent and laminar flow models were compared to a series of earlier experimental results over a range of

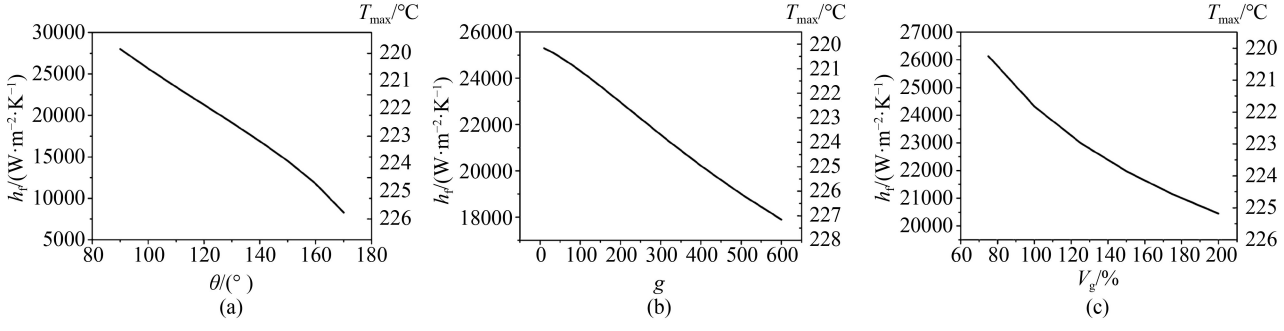

Fig. 56 (a) Convection heat transfer coefficient against cone angle. (b) Convection heat transfer coefficient against grain size. (c) Convection heat transfer coefficient against grain concentration [107].

low grinding temperature values. The turbulent flow model predictions were closer to the actual results. The turbulent flow model predicted drastically higher h_f values than the laminar flow model. However, below the boiling range, the TFM predictions were still lower than the measured results. At notably low grinding temperatures, the predicted values from both models are excessively low, indicating that as the grinding temperature decreases, the heat transfer coefficient diminishes, leading to reduced heat dissipation during the grinding process.

Table 10 further summarizes the factors influencing the CHTC coefficient in cutting and grinding machining.

Table 10 Factors affecting the CHTC coefficients

Reference	Processing parameters			Processing tool	Workpiece materials	Cooling method	Coolant	Influencing factor	Conclusion
	v_s/(m·s^{-1})	v_w/(m·s^{-1})	a_p/mm						
Liu et al. [144]	30	6	10, 20, 30	CBN grinding wheel	Ti–6Al–4V	Low temperature cold-air MQL	Vegetable oil-based F30-A	Lubricant physical properties (density, viscosity, and specific heat capacity), temperature, and flow state	The theoretically calculated values of the heat transfer coefficient h_f at different cold air temperatures are basically in agreement with the actual measured values, with modeling errors ranging from 8.5% to 11.6%
Gupta and Yadav [22]	60, 68, 76	1 mm/s	0.5, 0.7, 0.9, 1.1	CBN grinding wheel	Aluminum	Wet grinding	Water/ kerosene	Depth of grind, grinding wheel speed, nature of grinding fluid	The CHTC increases with grinding wheel speed and decreases with increasing grinding depth. This value is positively correlated with the specific heat, density, and conductivity of the coolant, and negatively correlated with the viscosity
Lin et al. [148,149]	36	270 mm/s	0.01–0.06	Vitrified bond aluminum oxide grinding wheel	Foundry iron/M50	Wet grinding	Water-based coolant	Actual depth of cut, wheel speed, and contact length	The value of the convection coefficient varies with the actual depth of cut and wheel speed of the work and decreases with increasing contact length
Jin et al. [147]	18, 30, 60	0.0006, 0.005, 0.3	1, 0.5, 0.96	Aluminum oxide grinding wheel	AISI 1095, AISI 1010, AISI 1020, AISI 52100	Wet grinding	Oil, emulsion	Liquid film thickness, wheel speed, porosity, grain size, coolant viscosity, and nozzle size	The physical properties of the coolant (viscosity and thermal conductivity) have a slightly greater influence on the sensitivity than the process parameters (grinding wheel speed)
Jin et al. [150]	28–50	10–30 mm/min	0.1–0.7	Porous metal bond CBN grinding wheel	High-temperature alloys	Wet grinding	Oil-based grinding fluids	Contact arc length, Feed rate, grinding rate	Changes in contact arc length and feed rate have a small effect on the distribution of CHTC in the main convection heat transfer zone, and the grinding speed is the main factor affecting CHTC
Gao et al. [151]	–	–	–	Grinding disc	Copper	Wet grinding	Water-based coolant	Coolant flow	The effect of coolant flow rate is more substantial when the flow rate is small, and the cooling heat transfer coefficient increases slowly when the flow rate is large to a certain value
Shen [154]	–	–	–	Vitrified bond aluminum oxide (CBN) grinding wheel	Nodular cast iron	Dry grinding/ wet grinding/ MQL	Water-based/oil-based nanofluids	Grinding zone, coolant flow	The flow velocity in the contact zone is high and the CHTC is higher than the trailing edge. Wet grinding has notably higher CHTC in the contact zone and at the trailing edge than MQL grinding
Zhu et al. [107]	60	0.24	0.017	CBN grinding wheel	Ti–6Al–4V	Dry grinding/ wet grinding	Oil-based coolant	Energy distribution ratio	When the other parameters are kept constant and only the R_{ws} value is changed, the maximum error reaches 22.6%, and a small change in the R_{ws} value can have a large effect on the grinding temperature during the calculation process
Zhang and Rowe [155]	–	–	–	–	–	–	–	Fluid flow state	The predictions of the turbulent flow model are closer to the actual results. The turbulent flow model predicted substantially higher h_f values than the laminar flow model

5 Model synthesis evaluation and parametric impact analysis

Several different models of heat transfer process parameters are available, and the effect of influencing factors on the parameters is full of variations. Models with high accuracy can be effectively identified by summarizing and evaluating the existing models. By analyzing the mechanism of the influence of each factor on the parameters, the change trend of heat transfer process parameters under the influence of each factor can also be effectively understood.

5.1 Evaluation of heat transfer process parameters models

5.1.1 EDC model

In the study of the heat transfer process, a reasonable choice of different EDC models can effectively reduce error projection results. Owing to differences in model construction process, each model adopts different approaches or methodologies, with varying emphasis on influencing factors. Therefore, under different processing conditions, selecting the appropriate type of EDC model based on the importance of influencing factors can help minimize modeling errors. The different models are categorized as shown in Fig. 57.

EDC models can generally be divided into two main categories based on whether experimental involvement is required. The first category does not require experimental data; instead, the models are constructed using known parameters and pre-determined processing parameters. For example, models associated with abrasive grain–workpiece contact are developed by employing intrinsic parameters of the grinding wheel and workpiece (thermal conductivity, specific heat capacity, abrasive grain radius), along with a preset parameters such as rotational speed of the grinding wheel. By modeling the grinding wheel and the fluid as a composite system, a relatively simple predictive model can be constructed based on the thermal parameters of the grinding wheel and the coolant. However, due to unclear overall thermal characteristics of the composite, such models are mainly used for qualitative analysis of the energy distribution during the grinding process. This category also includes partial models based on single particles, material physical parameters, slicing multiple energy distribution subsystems, and considerations such as heat-source tilt angle. A comprehensive model in this group is the one developed from the studies of Mao et al. [100] and Rowe [97], which fully incorporates the physical parameters of the grinding wheel and the workpiece, effective contact radius of the abrasive, the speed of the workpiece and the grinding wheel, coolant properties, effective grinding force per unit width, and wheel accuracy. Owing to its broad adaptability and capability to capture the influence of multiple factors, this model has become a widely adopted method for EDC calculation. The EDC model proposed by Yin and Marinescu [115], based on the assumption that the grinding wheel and the grinding fluid are compounded as a whole, also considers the effects of several factors, including the

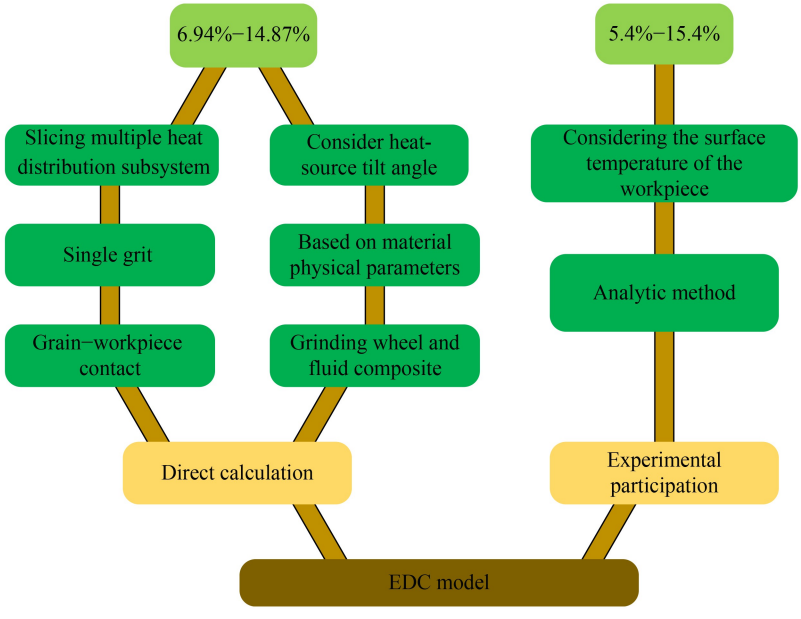

Fig. 57 Classification tree diagram of the EDC model.

workpiece feed rate, depth of cut, equivalent grinding wheel diameter, tangential grinding force, physical and thermal properties of the grinding wheel and the workpiece, and the cooling effect of the grinding fluid. This model has the best accuracy among such models, with errors ranging from 6.94% to 14.87%. The second category requires experimental participation, and the required parameters in the model calculation must be measured experimentally. For example, the turning energy distribution model based on the analytical method of multisystem construction combines the physical and thermal parameters of the workpiece and tool materials, as well as the measured temperature during the turning process and the calculation of the energy distribution of the subsystems, to obtain the energy distribution of the workpiece. Moreover, the grinding energy distribution model, considering the surface temperature of the workpiece, calculates the density of heat flow into the workpiece by combining its temperature increase, which leads to the calculation results. The accuracy of such models is roughly in the range of 10% to 20%, and the accuracy of the energy distribution model derived by Hadad et al. [95], from the maximum temperature increase of the work-in during grinding, can be achieved with an error in the range of 5.4% to 15.4%.

5.1.2 CHTC model

CHTC plays a crucial role in the study of heat transfer during machining. Aiming to control the temperature of the machining zone, the use of coolant is the most common method. As the coolant flow throughs the machining zone, convective heat transfer between the continuously flowing coolant and the surface of the machining zone removes a substantial amount of heat, effectively lowering the temperature of the machining zone. Therefore, an appropriate CHTC model enables more accurate calculation of the heat carried away by the coolant, thereby minimizing the errors in predicting the temperature of the machining zone. Moreover, a well-established convective heat transfer model helps identify the key factors affecting the heat transfer efficiency. This understanding allows for targeted improvements in the cooling process, effectively reducing thermal damage caused by untimely heat dissipation in the machining process.

As shown in Fig. 58, during the machining process, convective heat transfer includes gases and coolants. In terms of gas-based convective heat transfer, one category arises due to natural convective heat transfer between the tool or workpiece and the surrounding air. For example, Yin et al. [123] modeled the CHTC between the workpiece and the air, considering the heat exchange with the air during the continuous rotation of the workpiece. Another category involves the input of cold air into the machining area. This approach, known as low-temperature cold air cooling technology, facilitates strong convective heat transfer between the cold air and the grinding wheel or workpiece, effectively removing the heat generated in the machining area.

In terms of convective heat transfer in coolants, several categories are presented.

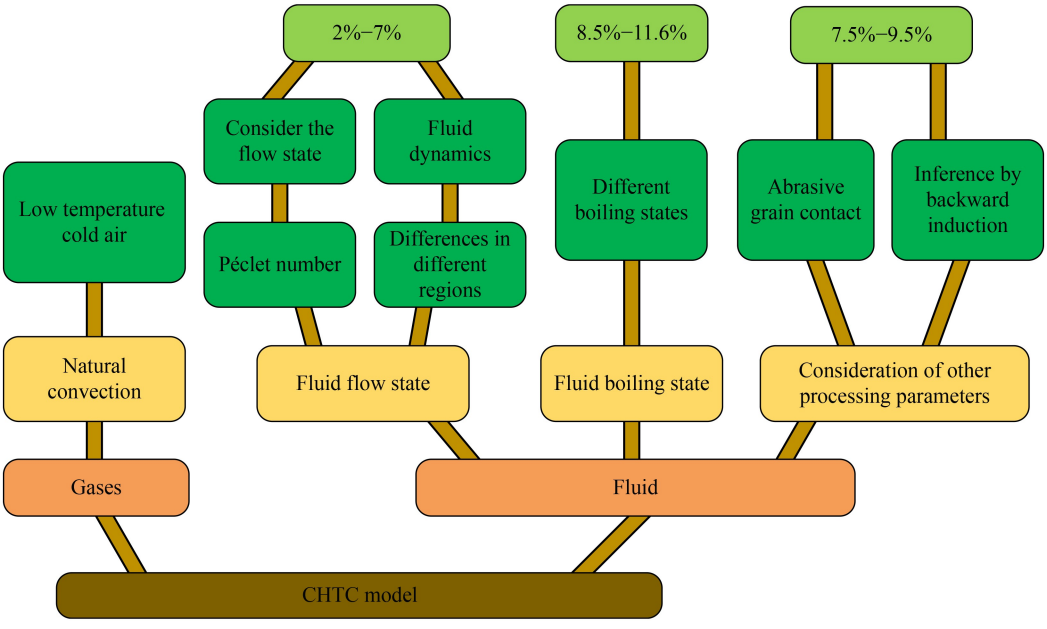

Fig. 58 Classification tree diagram of the CHTC model.

The first category focuses on a model that considers the flow state of the coolant, highlighting the physical properties of the coolant itself and the state of the flow process. Owing to variations in type, density, viscosity, and other physical parameters, different coolants exhibit different heat transfer efficiencies. As the coolant flows through the machining zone, it is agitated by the rotating tool, which leads to changes in its flow state and, consequently, its convective heat transfer efficiency. With the emergence of advanced cooling methods such as MQL, factors such as droplet number and droplet diffusion area have gained importance. Relevant models include those based on fluid mechanics, those incorporating the Péclet number, and those that consider the difference of fluid in different areas of the grinding zone and the fluid flow state. Among such models, the convective heat transfer model derived by Wang [157], considering the flow state and using a system of differential equations, has a good accuracy with an error of 2%–7%.

The second category is a model that considers the boiling state of the coolant. The coolant will change its boiling state after heat absorption in the processing zone. Different boiling states will have varying effects on the convective heat transfer efficiency. Liu et al. [144] constructed a convective heat transfer model with an accuracy error of 8.5%–11.6% in low-temperature cold-air MQL machining, considering the effects of liquid film boiling.

The third category focuses on a model that considers other processing parameters. The machining process is an interconnected and complex process, with various factors affecting each other. The speed of the grinding wheel, particle distribution, contact length, and surface temperature will influence the heat transfer efficiency of the coolant, for example, the model based on the particle contact conditions, and the model using the backpropagation method. Zhu et al. [107] considered the optimization of abrasive particle geometry, and distribution of CHTC calculation model accuracy can achieve errors ranging from 7.5% to 9.5%.

The various types of models are not completely independent, and a cross-mixture often exists. In this paper, the categorization is based primarily on the main influencing factors.

5.2 Parameter effects and mechanistic analysis

5.2.1 Parameters related to EDC

The main parameters affecting the variation of the EDC during machining include the depth of grind (depth of cut), grinding wheel speed, feed rate, coolant, workpiece material, grinding wheel type, grit distribution, and geometry.

The grinding depth refers to the depth of the grinding wheel cutting feed during each grinding process. When the grinding depth is greater, the amount of material removed in a single pass increases, the grinding force increases, and additional heat is generated by friction and cutting. Thus, when the grinding depth is increased, additional energy is consumed in other areas, and the proportion of energy absorbed by the workpiece is relatively reduced [108,162]. As for the grinding wheel speed, at high grinding speeds, higher speeds result in higher cutting temperatures and more heat generated by friction, which leads to the transfer of additional heat to the workpiece surface. Therefore, as the grinding wheel speed increases, the EDC of the workpiece generally increases. The effect of feed rate on the EDC is similar to that of the grind depth in that an increase in feed rate raises the grinding forces and generates additional heat. Therefore, the EDC typically increases with rising feed rate [161,162,165]. However, a larger feed rate helps to spread the generated heat quickly over a larger area, reducing the risk of localized high temperatures and leading to a reduction in the amount of heat absorbed by the workpiece. Consequently, a situation in which the EDC decreases with an increase in the feed rate also occurs. The coolant increases the heat exchange efficiency between the workpiece and the grinding wheel. Thus, minimal heat is absorbed on the surface of the workpiece, and additional heat is carried away. Therefore, coolant application is usually effective in reducing the energy distribution ratio of the workpiece [95,111,163]. Properties such as thermal conductivity, hardness, and heat capacity of different workpiece materials can substantially affect the absorption and conduction of heat energy. Harder workpiece materials generally absorb more thermal energy, while workpieces with higher thermal conductivity can dissipate heat to other areas more quickly, thus changing the energy distribution ratio of the workpiece [167]. Changes in the properties of different grinding wheels can directly influence their cutting performance and heat generation. A grinding wheel with effective thermal conductivity facilitates the transfer of additional heat to the wheel, reducing the energy distribution of the workpiece [84,164]. With the development of technology, the use of new grinding wheels such as heat pipe grinding wheels has increased [39,169,170]. The high thermal conductivity of new grinding wheels can effectively change the proportion of heat transferred to the workpiece [171]. Furthermore, the distribution and geometry of grinding wheel grits affect the energy distribution. The coarseness and fineness of the abrasive grains,

the size of the cone angle, and the unevenness of the distribution all affect the overall energy distribution [107].

5.2.2 Parameters related to CHTC

The main parameters affecting the variation of CHTC during machining include the following: fluid properties (density, specific heat, viscosity, and thermal conductivity), flow rate, speed of the grinding wheel, depth of grinding, parameters of the grinding wheel (taper angle, size of the abrasive grit, and porosity), and temperature difference.

Fluid properties mainly affect convective heat transfer [22]. Dense fluids generally have high heat capacity and efficient heat transfer characteristics. The greater the specific heat, the greater the ability of the fluid to absorb heat, absorbing the heat between the grinding wheel and the workpiece more effectively and improving the heat transfer efficiency. Fluids with high thermal conductivity can efficiently conduct heat. Therefore, when the three aforementioned factors increase, the CHTC will also increase. The greater the viscosity of the fluid, the greater the resistance to fluid flow, making turbulence less likely to occur and reducing heat transfer efficiency of the fluid. The flow rate of the fluid also affects its flow state during the process. A large flow rate of fluid has a greater capability to carry away heat, with higher shear and turbulence intensity on the contact surface, which disrupts the thermal boundary layer and improves heat transfer efficiency [151,155]. Cooling methods, such as the more environmentally friendly MQL, have emerged, but high-flow cast cooling usually provides better cooling results in comparison. Although the increase in the speed of the grinding wheel leads to the generation of additional heat, the high-speed rotation of the grinding wheel helps to increase the disturbance of the fluid, creating stronger turbulence, which, in turn, enhances the convective heat transfer capability of the fluid. The influence of the parameters of the grinding wheel grit on the heat transfer efficiency lies in the size of the heat transfer area. A large cone angle results in a large abrasive grain size, a small abrasive grain spacing, a small porosity, and a reduced heat exchange area with the fluid, thus minimizing the CHTC [107]. Temperature difference is a key factor affecting convective heat transfer efficiency. A larger temperature difference indicates a stronger heat transfer driving force. The larger the temperature difference, the more pronounced the convective effect of the fluid and the higher the heat exchange efficiency. Therefore, low-temperature cold-air cooling technology, which increases the temperature difference by reducing the air temperature, has a good cooling effect.

6 Conclusions and prospects

6.1 Conclusions

This paper provides a comprehensive review of EDC and CHTC models for cutting and grinding machining, including their specific applications and scope. In addition, potential directions for grinding thermal research are introduced to address current issues related to grinding thermal modeling.

(1) Aiming to solve the EDC model of the grinding process, the uniform heat-source model or the triangular heat-source model can be used. The triangular heat source closely algins with the actual working conditions, and the EDC model proposed by Yin, based on the contact between the abrasive particles and the workpiece, has a high accuracy, revealing approximately 6.94%–14.87%.

(2) The study of CHTC requires consideration of process parameters and fluid characteristics, including flow velocity, flow rate, boiling conditions, flow state, fluid type, physical parameters, and injection mode. Wang proposed a CHTC model based on the convective heat transfer differential equation system and fixed conditions, which demonstrated a high accuracy of approximately 2%–2.7%.

(3) Normally, the higher the speed of the grinding wheel, the higher the feed rate, and the harder the workpiece material, the higher the EDC of the workpiece. Conversely, a better cooling effect and a higher thermal conductivity of the grinding wheel result in a smaller workpiece EDC.

(4) The greater the grinding wheel speed, fluid specific heat, and fluid flow rate, the greater the CHTC. A high depth of cut, feed rate, fluid viscosity, and grain size lead to a small CHTC. Simultaneously, the nozzle position, flow rate, and fluid type also have substantial effects on the coefficient of variation.

6.2 Prospects

(1) Current modeling studies on EDC and CHTC are mainly conducted for grinding processes, with a lack of widely recognized, practical, and reliable models in the cutting process. Therefore, further research and exploration of thermal modeling in the cutting process is urgently needed.

(2) The energy distribution ratio plays a crucial role in studying workpiece temperature during machining. However, this coefficient is a complex variable that cannot be directly measured and is affected by many factors such as machining parameters, grain shape,

grinding wheel parameters, coolant, and workpiece properties. While various models have been developed using different methods, a convincing, unified theory is lacking.

(3) The determination of CHTC is crucial for studying the cooling effect in the machining zone. However, due to uncertainties in the physical properties of the coolant, workpiece, grinding wheel, and other physical parameters, as well as the difficulty in fully controlling and simulating the real working conditions in the experiments, the change in boundary conditions will affect the measurement results. Additionally, with the introduction of nanofluids and advanced materials, existing models may not effectively describe their heat transfer characteristics. Therefore, further in-depth research and exploration on this area is still needed.

Nomenclature

Abbreviations

CBN	Cubic boron nitride
CHTC	Convective heat transfer coefficient
EDC	Energy distribution coefficient
HEDG	High-efficiency deep grinding
MQL	Minimum quantity lubrication
NMQL	Nanofluid minimum quantity lubrication
SG	Seeded gel
TFM	Turbulent flow model

Variables

a_1, a_2	Thermal diffusivity of workpiece materials at different temperatures
a_{gmax}	Maximum undeformed chip thickness
a_{p}	Grinding depth
a_{w}	Workpiece length
A	Nominal contact area
A'	Diffusion area of the droplet
A_0	Average single abrasive particle contact area
A_{f}	Convective surface area
A_i	Area of region Ω_i
A_{R}	Actual contact area
A_{t}	Tool–chip contact area coefficient
b	Heat storage coefficient
b_{s}	Grinding width
b_0	Half-width of the nozzle exit section
c	Specific heat capacity
c_{l}	Specific heat capacity of droplets
c_{nf}	Specific heat capacity of fluids
c_{s}	Specific heat of the grinding wheel
c_{v}	Specific heat capacity of steam
C_0	Parameter factor in the circular moving heat-source model
d	Diameter of the circular surface
d_0	Diameter of a single droplet
d_1	Borehole diameter
d_2	Diameter of the heated cylinder
d_{b}	Diameter of a single bubble
d_{drill}	Diameter of the drill bit
d_{g}	Equivalent average particle diameter
d_{s}	Diameter of the grinding wheel
D	Diameter of the milling cutter
e_{s}	Specific grinding energy
e_{sch}	Specific cutting energy
f_z	Feed per tooth
F_{t}	Tangential grinding force
F_{vm}	Principal grinding resistance
G_{a}	Active abrasive particles per unit area of grinding wheel surface
h	Convective heat transfer coefficient
h_0	Heat transfer coefficient
h'_a	Convective heat transfer coefficient of air at room temperature
h_{ch}	Heat transfer coefficient of debris
h_{D}	Depth of cut
h_{f}	Convection coefficient of the coolant
h_{g}	Heat transfer coefficient of the grain
h_{w}	Heat transfer coefficient of the workpiece
h_{fa}	Latent heat of vaporization
J	Heat transfer of a single droplet
k	Thermal conductivity
k_{a}	Thermal conductivity of air
k_{c}	Coating thermal conductivity
k_{g}	Thermal conductivity of grain
k_{nf}	Thermal conductivity of fluids
k_{t}	Thermal conductivity of cutting tools
k_{v}	Thermal conductivity of steam
k_{w}	Thermal conductivity of workpieces
K_0	Type II zero-order modified Bessel function
K_{s}	Cutting force to cutting cross-sectional area ratio
l_{c}	Contact length
l_{f}	Tool–debris contact length

l_{wf}	Average diameter of the wear plane
L	Drilling depth
L_{g}	Average particle spacing
m_0	Mass of droplets participating in heat transfer
m_{d}	Droplet mass
M_z	Torque
n	Spindle speed
N_{l}	Droplet quantity
N_{b}	Number of nucleation sites (per unit area) on the superheated surface
Nu	Nusselt number
N_z	Number of all droplets
p_{a}	Pressure inside the nozzle
$P_{\mathrm{el.meas.}i}$	Effective spindle power
p_0	Atmospheric pressure
Pe	Péclet number
Pr	Prandtl number of flowing air
q_2	Cutting heat generated at the tool–chip interface per unit time
q_{a}	Heat transmitted into abrasive grains
q'_{a}	Heat transfer rate by air convection
q_{ch}	Heat transmitted into debris
q_{d}	Heat flux density of a single droplet during heat transfer
q_{f}	Heat transferred by cooling medium
q_{fluid}	Heat flow of the fluid
q_{s}	Heat transmitted to the grinding wheel
q_{t}	Total heat generated in the grinding area
q_{w}	Intensity distribution of heat source flowing into the workpiece
Q	Grinding power
Q'	Supply amount of nanofluid during the grinding time
r_0	Radius of abrasive wear
r_{g}	Apex radius of conical abrasive grain
r_{surf}	Diffusion radius of a single droplet
R_{ch}	Energy distribution coefficient of the debris
R_{dry}	Proportion of heat transferred to the workpiece at the initial moment
Re	Reynolds number
Re_{lc}	Critical Reynolds number
Re_{r}	Dimensionless rotational Reynolds number
R_{f}	Energy distribution coefficient of the grinding wheel
R_{s}	Energy distribution coefficient of the grinding wheel
R_{w}	Energy distribution coefficient of the workpiece
R_{ws}	Workpiece–grain particle energy distribution ratio
S	Area covered by the nozzle jet
t	Total grinding time
$t_{\mathrm{a}}(\xi_{\mathrm{i}})$	Undeformed chip thickness
t_{l}	Initial temperature of droplets
t_s	Heat transfer time
T	Workpiece temperature rise
T_0	Ambient temperature
T_{l}	Nanofluid temperature
T_{a}	Initial temperature
T_{b}	Fluid burnout temperature
T_{d}	Average temperature of the drill bit surface
T_{f}	Temperature of the coolant
T_{gmax}	Maximum temperature rise at the abrasive grain–workpiece contact surface
T_{max}	Maximum temperature rise of workpiece
$T_{\mathrm{max\text{-}c}}$	Maximum contact temperature
T_{s}	Saturation temperature
T_t	Temperature at time t
T_{w}	Workpiece melting point temperature
T_∞	Convective ambient temperature
$\overline{T}$	average temperature of the workpiece
u	Tangential velocity of ambient air around the circumferential end face
u_0	Exit velocity
v_{av}	Average velocity of the fluid through the grinding zone
v_{c}	Cutting speed
v_{ch}	Chip flow rate
v_{l}	Jet velocity of droplets along the nozzle direction
v_{n}	Vertical impact velocity of droplets on the heat transfer surface
v_{s}	Cutting tool or grinding wheel speed
v_{w}	Workpiece velocity
V	Volume
V_{l}	Volume of a single droplet
We	Weber number
x	Distance from the grinding zone
x_{l}	Coating thickness
z	Number of Teeth
τ	Dimensionless time
α_{f}	Thermal diffusivity of fluids

α_g	Thermal diffusivity of abrasive particles
α_w	Thermal diffusivity of workpieces
β	Constants related to the shape of the heat source
γ	Geometric shape factor of a single abrasive grain
δ	Thickness of the coolant film in the grinding zone
η	Kinematic viscosity of fluid
θ	Angle between the mist jet and the horizontal direction
θ_0	Average temperature of the grain
θ_0'	Initial temperature of the tool
θ_a	Surface temperature of the workpiece
θ_m	Maximum background temperature
θ_n	Contact angle
$\bar{\theta}_s$	Average temperature of the shear surface
λ_c	Thermal conductivity rate of coating
λ_s	Thermal conductivity rate of the matrix
λ_w	Thermal conductivity rate of the workpiece
μ	Dynamic viscosity of air
μ_f	Dynamic viscosity of fluid
μ_v	Dynamic viscosity of steam
σ	Surface tension
ρ	Density
ρ_c	Volume specific heat
ρ_s	Density of the grinding wheel
ρ_a	Air density
ρ_l	Nanofluid density
ρ_{nf}	Fluid density
φ	Mass flow rate
ζ	Roll angle
ζ_b	Latent heat of the bubble
ΔT	Temperature difference in heat exchange
Λ_h	Cutting deformation coefficient

Subscripts

f	Coolant
g	Abrasive grain
w	Workpiece

Acknowledgements This study was financially supported by the National Natural Science Foundation of China (Grant Nos. 52205481 and 52305477), the Support plan for Outstanding Youth Innovation Team in Universities of Shandong Province, China (Grant No. 2023KJ114), the Young Talent of Lifting Engineering for Science and Technology in Shandong, China (Grant No. SDAST2024QTA043), the Key Laboratory of Industrial Fluid Energy Conservation and Pollution Control (Ministry of Education of China) (Grant No. CK-2024-0033), and the General Program of Shandong Provincial Natural Science Foundation, China (Grant No. ZR2024ME205).

Conflict of Interest Changhe LI is a member of the Editorial Board of *Frontiers of Mechanical Engineering*, who was excluded from the peer review and all editorial decisions related to the acceptance and publication of this article. Peer review was handled independently by the other editors to minimize bias.

References

1. Guo C S, Chen Y. Thermal modeling and optimization of interrupted grinding. CIRP Annals, 2018, 67: 321–324
2. Gong P, Zhang Y B, Wang C J, Cui X, Li R Z, Sharma S, Liu M Z, Gao T, Zhou Z M, Wang X M, Dambatta Y S, Li C H. Residual stress generation in grinding: mechanism and modeling. Journal of Materials Processing Technology, 2024, 324: 118262
3. Xian C, Shi Y Y, Lin X J, Liu D. Experimental study on energy partition of polishing aero-engine blades with abrasive cloth wheel. The International Journal of Advanced Manufacturing Technology, 2020, 106: 1839–1853
4. Yao C F, Wang T, Xiao W, Huang X C, Ren J X. Experimental study on grinding force and grinding temperature of Aermet 100 steel in surface grinding. Journal of Materials Processing Technology, 2014, 214(11): 2191–2199
5. Sun J G, Yang M, Yang Y Y, Zhang Y B, Dambatta Y S, Zhou Z M, Li C H. Ultrasonic micro-grinding biological bone non-uniform heat source temperature field model and experimental verification. Journal of Mechanical Engineering, 2024, in press (in Chinese)
6. Brinksmeier E, Aurich J C, Govekar E, Heinzel C, Hoffmeister H W, Klocke F, Peters J, Rentsch R, Stephenson D J, Uhlmann E, Weinert K, Wittmann M. Advances in modeling and simulation of grinding processes. CIRP Annals, 2006, 55(2): 667–696
7. Ma X F, Yao B, Cai Z Q, Li Z M Q, Li Z S, Chen G F, Liu W S. Temperature field responses to face gear

grinding conditions based on a comprehensive force–thermal model. Precision Engineering, 2023, 83: 22–41
8. Dai C W, Ding W F, Zhu Y J, Xu J H, Yu H W. Grinding temperature and power consumption in high speed grinding of Inconel 718 nickel-based superalloy with a vitrified CBN wheel. Precision Engineering, 2018, 52: 192–200
9. Dai S J, Wang X J, Zhang H B, Wen B R. Research on variation of grinding temperature of wind turbine blade robotic grinding. Proceedings of the Institution of Mechanical Engineers, Part B: Journal of Engineering Manufacture, 2021, 235(3): 367–377
10. Langenhorst L, Sölter J, Heinzel C. Partitioning of primary shear zone heat in face milling. CIRP Annals, 2022, 71(1): 53–56
11. Brosse A, Naisson P, Hamdi H, Bergheau J M. Temperature measurement and heat flux characterization in grinding using thermography. Journal of Materials Processing Technology, 2008, 201(1–3): 590–595
12. Zhang Z Y, Shang W, Ding H H, Guo J, Wang H Y, Liu Q Y, Wang W J. Thermal model and temperature field in rail grinding process based on a moving heat source. Applied Thermal Engineering, 2016, 106: 855–864
13. Mohamed A O, Bauer R, Warkentin A. Uncut chip thickness and coolant delivery effects on the performance of circumferentially grooved grinding wheels. The International Journal of Advanced Manufacturing Technology, 2016, 85: 1429–1438
14. Kizaki T, Zheng Q R, Shu L M, Tanaka J, Katsuma T. On reduction of energy flow into workpiece in continuous generating grinding. CIRP Annals, 2022, 71(1): 277–280
15. Jamshidi H, Budak E. Grinding temperature modeling based on a time dependent heat source. Procedia CIRP, 2018, 77: 299–302
16. Fang C F, Lin Y F, Xu X P. A thermal model for the calculation of energy partitions in sawing with a segmented blade. High Temperatures – High Pressures, 2016, 45(1): 35–56
17. Gao T, Xu P M, Wang W, Zhang Y B, Xu W H, Wang Y Q, An Q L, Li C H. Force model of ultrasonic empowered minimum quantity lubrication grinding CFRP. International Journal of Mechanical Sciences, 2024, 280: 109522
18. Shen J Y, Zeng W M, Huang H, Xu X P. Thermal aspects in the face grinding of ceramics. Journal of Materials Processing Technology, 2002, 129(1–3): 212–216
19. Zhang J, Lv M, Wang S Y. The influence of side contact area on the grinding heat partition in narrow narrow deep groove. Machinery Design & Manufacture, 2019, 1: 166–169 (in Chinese)
20. Yang M, Hao J C, Wu W T, Li Z H, Ma Y Q, Zhou Z M, Gao T, Liu M Z, Cui X, Zhang Y B, Li B K, Ma X, Dambatta Y S, Li C H. Critical cutting thickness model considering subsurface damage of zirconia grinding and friction–wear performance evaluation applied in simulated oral environment. Tribology International, 2024, 198: 109881
21. Mao M Z, Liu S B, Jiang J L, Sun S F, Wang D X. Study on flow field and convective heat transfer characteristics in grinding zone of large spiral angle flow disturbance grooved wheel. The International Journal of Advanced Manufacturing Technology, 2023, 129(1-2): 39–63
22. Gupta P K, Yadav N P. Numerical investigation into convective heat transfer coefficient of the grinding fluid used in a deep grinding process. Transactions of Famena, 2024, 48(2): 129–144
23. Song Y X, Li C H, Zhou Z M, Liu B, Sharma S, Dambatta Y S, Zhang Y B, Yang M, Gao T, Liu M Z, Cui X, Wang X M, Xu W H, Li R Z, Wang D Z. Nanobiolubricant grinding: a comprehensive review. Advances in Manufacturing, 2025, 13(1): 1–42
24. He Q S, Fu Y C, Chen J J, Zhang W. Investigation on heat transfer performance of heat pipe grinding wheel in dry grinding. Journal of Manufacturing Science & Engineering, 2016, 138(11): 111009
25. He Q S, Fu Y C, Chen J J, Zhang W, Cui Z M. Experimental investigation of cooling characteristics in wet grinding using heat pipe grinding wheel. The International Journal of Advanced Manufacturing Technology, 2018, 97(1–4): 621–627
26. Gu G Q, Wang D Z, Wu S J, Zhou S, Zhang B X. Research status and prospect of ultrasonic vibration and minimum quantity lubrication processing of nickel-based alloys. Intelligent and Sustainable Manufacturing, 2024, 1(1): 10006
27. Li C H. Thermodynamic Mechanism of MQL Grinding with Nano Bio-lubricant. Singapore: Springer Nature Singapore Pte. Ltd., 2024, 117–140
28. Mao C, Zou H F, Huang Y, Li Y F, Zhou Z X. Analysis of heat transfer coefficient on workpiece surface during minimum quantity lubricant grinding. The International Journal of Advanced Manufacturing Technology, 2013, 66(1): 363–370
29. Song Y X, Xu Z L, Li C H, Zhou Z M, Liu B, Zhang Y B, Dambatta Y S, Wang D Z. Research progress on the grinding performance of nanobiolubricant minimum quantity lubrication. Surface Technology, 2023, 52(12): 1–19 (in Chinese)
30. Sinha M K, Madarkar R, Ghosh S, Rao P V. Application of eco-friendly nanofluids during grinding of Inconel 718 through small quantity lubrication. Journal of Cleaner Production, 2017, 141: 1359–1375
31. Cui X, Li C H, Zhang Y B, Ding W F, An Q L, Liu B, Li H N, Said Z, Sharma S, Li R Z, Debnath S. Comparative assessment of force, temperature, and wheel wear in sustainable grinding aerospace alloy

using biolubricant. Frontiers of Mechanical Engineering, 2023, 18(1): 3

32. Sharma P, Said Z, Kumar A, Nižetić S, Pandey A, Hoang A T, Huang Z H, Afzal A, Li C H, Le A T, Nguyen X P, Tran V D. Recent advances in machine learning research for nanofluid-based heat transfer in renewable energy system. Energy & Fuels, 2022, 36(13): 6626–6658
33. Liu J Y, Srebric J, Yu N Y. Numerical simulation of convective heat transfer coefficients at the external surfaces of building arrays immersed in a turbulent boundary layer. International Journal of Heat and Mass Transfer, 2013, 61: 209–225
34. Zhu D H, Li B Z, Ding H. A combined model with optimal solution for prediction of grinding temperature. International Journal of Materials & Product Technology, 2014, 49(4): 203–223
35. García E, Méresse D, Pombo I, Harmand S, Sánchez J A. Identification of heat partition in grinding related to process parameters, using the inverse heat flux conduction model. Applied Thermal Engineering, 2014, 66(1–2): 122–130
36. Zhao B, Huang Q, Cao Y, Ding W F, Xu J H, Liu G L. Thermal analysis of ultrasonic vibration-assisted grinding with moment-triangle heat sources. International Journal of Heat and Mass Transfer, 2023, 216: 124552
37. Rowe W B, Jin T. Temperatures in high efficiency deep grinding (HEDG). CIRP Annals, 2001, 50(1): 205–208
38. Wang Y L, Zhang Y B, Cui X, Liang X L, Li R Z, Wang R X, Sharma S, Liu M Z, Gao T, Zhou Z M, Wang X M, Dambatta Y S, Li C H. High-speed grinding: from mechanism to machine tool. Advances in Manufacturing, 2025, 13(1): 105–154
39. Zhang L Y, Chen J J, Jiang H F, Xu Y L, Qian N, Fu Y C, Chen Y, Dai C W. Analysis for green grinding of Ti-6Al-4V titanium alloys with profile rotating heat pipe-grinding wheel. The International Journal of Advanced Manufacturing Technology, 2024, 131: 2537–2549
40. Jiang J L, Ge P Q, Sun S F, Wang D X, Wang Y L, Yang Y. From the microscopic interaction mechanism to the grinding temperature field: an integrated modelling on the grinding process. International Journal of Machine Tools & Manufacture, 2016, 110: 27–42
41. Wang Y, Xie J H, Xiong W, Yang L, Zhang S. Research on simulation of heat source model based on finite element method in surface grinding. Journal of System Simulation, 2016, 28(11): 9 (in Chinses)
42. Zhang L, Ge P Q, Meng J F, Cheng J H, Wang M. Newheat flux model in surface grinding. Materials Science Forum, 2004, 471–472: 298–301
43. Lefebvre A, Vieville P, Lipinski P, Lescalier C. Numerical analysis of grinding temperature measurement by the foil/workpiece thermocouple method. International Journal of Machine Tools & Manufacture, 2005, 46(14): 1716–1726
44. Zhang Y B, Gong P, Tang L Z, Cui X, Jia D Z, Gao T, Dambatta Y S, Li C H. Topography modeling of surface grinding based on random abrasives and performance evaluation. Chinese Journal of Mechanical Engineering, 2024, 37(5): 93
45. Wang D X, Ge P Q, Bi W B, Jiang J L. Grain trajectory and grain workpiece contact analyses for modeling of grinding force and energy partition. The International Journal of Advanced Manufacturing Technology, 2014, 70: 2111–2123
46. Ren X K, Huang X K, Feng H J, Chai Z, He Y B, Chen H B, Chen X Q. A novel energy partition model for belt grinding of Inconel 718. Journal of Manufacturing Processes, 2021, 64: 1296–1306
47. Li Z, Ding W F, Liu C J, Su H H. Prediction of grinding temperature of PTMCs based on the varied coefficients of friction in conventional-speed and high-speed surface grinding. The International Journal of Advanced Manufacturing Technology, 2016, 90: 2335–2344
48. Duan Z J, Wang S S, Wang Z H, Li C H, Li Y H, Song J L, Liu J Y, Liu X. Tool wear mechanisms in cold plasma and nano-lubricant multi-energy field coupled micro-milling of Al-Li alloy. Tribology International, 2024, 192: 109337
49. Chen J Y, Xu X P. Temperature and energy partition in high-speed grinding of alumina with a brazed diamond wheel. Machining Science and Technology, 2010, 14(4): 440–454
50. Lefebvre A, Sinot O, Torrance A A, Lipinski P. Determination of the partition coefficient for the grinding of a hard WC-Co-Cr coating with a diamond wheel. Machining Science and Technology, 2014, 18(4): 585–602
51. Jin T, Stephenson D J, Xie G Z, Sheng X M. Investigation on cooling efficiency of grinding fluids in deep grinding. Cirp Annals, 2011, 60(1): 343–346
52. Zhang Y B, Li L Y, Cui X, An Q L, Xu P M, Wang W, Jia D Z, Liu M Z, Dambatta Y S, Li C H. Lubricant activity enhanced technologies for sustainable machining: mechanisms and processability. Chinese Journal of Aeronautics, 2025, 38(6): 103203
53. Duan Z J, Wang S S, Li C H, Wang Z H, Bian P, Sun J, Song J L, Liu X. Cold plasma and different nano-lubricants multi-energy field coupling-assisted micro-milling of Al-Li alloy 2195–T8 and flow rate optimization. Journal of Manufacturing Processes, 2024, 127: 218–237
54. Zhang J Z, Tan X M, Liu B, Zhu X D. Investigation for convective heat transfer on grinding work-piece surface subjected to an impinging jet. Applied Thermal Engineering, 2013, 51(1–2): 653–661
55. Duan Z J, Wang S S, Li C H, Wang Z H, Bian P,

Song J L, Liu X. Performance evaluation of cold plasma and h-BN nano-lubricant multi-field coupling assisted micro-milling of aluminum alloy 6061–T651. Alexandria Engineering Journal, 2024, 109: 610–625

56. Li B K, Li C H, Zhang Y B, Wang Y G, Yang M, Jia D Z, Zhang N Q, Wu Q D. Effect of the physical properties of different vegetable oil-based nanofluids on MQLC grinding temperature of Ni-based alloy. The International Journal of Advanced Manufacturing Technology, 2017, 89(9–12): 3459–3474
57. Said Z, Sundar L S, Rezk H, Nassef A M, Chakraborty S, Li C H. Thermophysical properties using ND/water nanofluids: an experimental study, ANFIS-based model and optimization. Journal of Molecular Liquids, 2021, 330: 115659
58. Tahvilian A M, Liu Z H, Champliaud H, Hazel B. Experimental and finite element analysis of temperature and energy partition to the workpiece while grinding with a flexible robot. Journal of Materials Processing Technology, 2013, 213(12): 2292–2303
59. Yi J, Jin T, Deng Z H. The temperature field study on the three-dimensional surface moving heat source model in involute gear form grinding. The International Journal of Advanced Manufacturing Technology, 2019, 103(5–8): 3097–3108
60. Yang Y. Li J L, Zhou L. Research on cutting thermal modeling and simulation of turning AISI 1045. Modular Machine Tool & Automatic Manufacturing Technique, 2018, 5: 34–36 (in Chinese)
61. Ding Z H, Huang L, Wang X C, Yuan J T. Simulation study on cutting heat distribution of cemented carbide coated tools for titanium alloy cutting. Tool Engineering, 2023, 57: 77–82 (in Chinese)
62. Liu W Y, Zhang Y, Li J, Liu X K. Simulation of heat distribution with FEA in high-speed cutting. Tool Engineering, 2009, 43(8): 14–17 (in Chinese)
63. Huang S W, Tao B, Li J D, Fan Y J, Yin Z P. Estimation of the time and space-dependent heat flux distribution at the tool-chip interface during turning using an inverse method and thin film thermocouples measurement. The International Journal of Advanced Manufacturing Technology, 2018, 99(5–8): 1531–1543
64. Quan Y M, He Z W, Dou Y. Cutting heat dissipation in high-speed machining of carbon steel based on the calorimetric method. Frontiers of Mechanical Engineering in China. 2008, 3(2): 175–179
65. Ma L J, Chen J Q, Deng H, Zhou Y G, Cai C Y, Sun Z C. Theoretical model of heat conduction of brittle material in the process of turning fluorophlogopite ceramics. Science Technology and Engineering, 2020, 20(11): 4345–4350 (in Chinese)
66. Bartoszuk M. Temperature and heat partition testing in the cutting zone for turning AISI 321 steel. Strojniški vestnik - Journal of Mechanical Engineering, 2020, 66(11): 629–641
67. Quan Y M, He Z W. Cutting heat distribution in turning of carbon steel. China Mechanical Engineering, 2006, 17: 2155–2158 (in Chinese)
68. Zhao J F, Zheng L R, Li W Q, Liu Z Q, Li L L, Wang B, Cai Y K, Ren X P, Liang X L. Effects of PVD CrAlN/(CrAlB)N/CrAlN coating on pin–disc friction properties of Ti2AlNb alloys compared to WC/Co carbide at evaluated temperatures. Metals, 2024, 14(6): 662
69. Xiao M H, He N, Li L, Lu A H. Study on cutting heat in high speed milling of nickel-based superalloy. Journal of Harbin Institute of Technology, 2011, 43: 105–109 (in Chinese)
70. Komanduri R, Hou Z B. Thermal modeling of the metal cutting process. International Journal of Mechanical Sciences, 2000, 42(9): 1715–1752
71. Sölter J, Gulpak M. Heat partitioning in dry milling of steel. CIRP Annals, 2012, 61(1): 87–90
72. Hu Y H, Ding H, Shi Y T, Zhang H Y, Zheng Q C. A predictive model for cortical bone temperature distribution during drilling. Physical and Engineering Sciences in Medicine, 2021, 44(1): 147–156
73. Patne H S, Kumar A, Karagadde S, Joshi S S. Modeling of temperature distribution in drilling of titanium. International Journal of Mechanical Sciences, 2017, 133: 598–610
74. Liu Y, Pan Z T, Zhou H G, Jing X W, Li G C. Review and prospect of drilling heat for fiber reinforced composite. Acta Materiae Compositae Sinica, 2023, 40(8): 4416–4439
75. Feng K K, Zhang F P, Wang W H. The micro-drilling process fine modeling with the strain characteristics of undeformed chip considered. Journal of Mechanical Science and Technology, 2022, 36(2): 883–895
76. Cuesta M, Aristimuño P, Garay A, Arrazola P J. Heat transferred to the workpiece based on temperature measurements by IR technique in dry and lubricated drilling of Inconel 718. Applied Thermal Engineering, 2016, 104: 309–318
77. Thanedar A, Dongre G G, Joshi S S. Analytical modelling of temperature in cylindrical grinding to predict grinding burns. International Journal of Precision Engineering and Manufacturing, 2019, 20(1): 13–25
78. Zhang B, Lu S X, Rabiey M, Axinte D, Bleicher F. Grinding of composite materials. Cirp Annals, 2023, 72(2): 645–671
79. Wang L, Ge P Q, Qin Y, Liu Z C, Sun J G, Gao W. Analysis of wet-grinding temperature field based on finite element method. Journal of Mechanical Engineering, 2002, 38(9): 155–158 (in Chinese)
80. Su J X, Zhang Y Z, Deng X Z. Analysis and experimental study of cycloid gear form grinding temperature field. The International Journal of Advanced Manufacturing Technology, 2020, 110: 949–965

81. Aurich J C, Herzenstiel P, Sudermann H, Magg T. High-performance dry grinding using a grinding wheel with a defined grain pattern. Cirp Annals, 2008, 57(1): 357–362
82. Biermann D, Holtermann R, Menzel A, Schumann S. Modelling and simulation of thermal effects in internal traverse grinding of hardened bearing steel. Cirp Annals, 2016, 65(1): 321–324
83. Fritsche A, Bleicher F. Experimental investigation of the heat flux distribution in grinding of titanium alloy. Procedia Engineering, 2015, 100: 987–993
84. Rowe W B. Temperature case studies in grinding including an inclined heat source model. Proceedings of the Institution of Mechanical Engineers, Part B: Journal of Engineering Manufacture, 2001, 215(4): 473–491
85. Hou Z B, Komanduri R. On the mechanics of the grinding process, Part II - thermal analysis of fine grinding. International Journal of Machine Tools & Manufacture, 2004, 44(2–3): 247–270
86. Guo C, Wu Y, Varghese V, Malkin S. Temperatures and energy partition for grinding with vitrified CBN wheels. CIRP Annals, 1999, 48(1): 247–250
87. Guo G Q, An Q L, Lin L F, Yang C Q, Chen M. Analytical and experimental investigation of temperature in form grinding. Journal of Mechanical Engineering, 2018, 54(3): 203–215 (in Chinese)
88. Guo C S, Malkin S. Energy partition and cooling during grinding. Journal of Manufacturing Processes, 2000, 2(3): 151–157
89. Qiu K X, Guo G Q, Yang C Q, Dong D P, Chen M. Investigation on temperature distribution in form grinding of 9Mn2V thread gauge. Proceedings of the Institution of Mechanical Engineers, Part B: Journal of Engineering Manufacture, 2018, 232: 1342–1350
90. Xu K Z, Wei C J, Hu D J, Xu L M, Xu M M. Temperature investigation of coated workpieces in intermittent grinding with a cup wheel. Proceedings of the Institution of Mechanical Engineers, Part B: Journal of Engineering Manufacture, 2012, 226(2): 239–246
91. Li B M, Zhao B. Modern Grinding Technology. Beijing: China Machine Press, 2003, 44–64
92. Su J X, Ke Q X, Deng X Z, Ren X Z. Numerical simulation and experimental analysis of temperature field of gear form grinding. The International Journal of Advanced Manufacturing Technology, 2018, 97: 2351–2367
93. Kizaki T, Takahashi K, Katsuma T, Shu L M, Sugita N. Prospects of dry continuous generating grinding based on specific energy requirement. Journal of Manufacturing Processes, 2021, 61: 190–207
94. Zhang P F, Zhang W L, Yuan Y J, Fan X Q, Zhu M H. Probing the effect of grinding-heat on material removal mechanism of rail grinding. Tribology International, 2020, 147: 105942
95. Hadad M J, Tawakoli T, Sadeghi M H, Sadeghi B. Temperature and energy partition in minimum quantity lubrication-MQL grinding process. International Journal of Machine Tools & Manufacture, 2012, 54–55: 10–17
96. Peng K L, Lu P, Lin F H, Jin T, Bao W C, Xie G Z, Shang Z T. Convective cooling and heat partitioning to grinding chips in high speed grinding of a nickel based superalloy. Journal of Mechanical Science and Technology, 2021, 35: 2755–2767
97. Rowe W B. Thermal analysis of high efficiency deep grinding. International Journal of Machine Tools & Manufacture, 2001, 41(1): 1–19
98. Ding Z S, Jiang X H, Guo M X, Liang S Y. Investigation of the grinding temperature and energy partition during cylindrical grinding. The International Journal of Advanced Manufacturing Technology, 2018, 97(5–8): 1767–1778
99. Zhang J C, Wu W T, Li C H, Yang M, Zhang Y B, Jia D Z, Hou Y L, Li R Z, Cao H J, Ali H M. Convective heat transfer coefficient model under nanofluid minimum quantity lubrication coupled with cryogenic air grinding Ti–6Al–4V. International Journal of Precision Engineering and Manufacturing-Green Technology, 2021, 8(4): 1113–1135
100. Mao C, Zhou Z X, Zhou D W, Gu D Y. The properties and the influence factors of the white layer in the surface grinding. Advanced Materials Research, 2008, 53–54: 285–292
101. Jin T, Stephenson D J, Corbett J. Burn threshold of high-carbon steel in high-efficiency deep grinding. Proceedings of the Institution of Mechanical Engineers, Part B: Journal of Engineering Manufacture, 2002, 216(3): 357–364
102. Yang M, Kong M, Li C H, Long Y Z, Zhang Y B, Sharma S, Li R Z, Gao T, Liu M Z, Cui X, Wang X M, Ma X, Yang Y Y. Temperature field model in surface grinding: a comparative assessment. International Journal of Extreme Manufacturing, 2023, 5(4): 042011
103. Ramanath S, Shaw M C. Abrasive grain temperature at the beginning of a cut in fine grinding. Journal of Manufacturing Science and Engineering, 1988, 110(1): 15–18
104. Kohli S, Guo C, Malkin S. Energy partition to the workpiece for grinding with aluminum oxide and CBN abrasive wheels. Journal of Engineering for Industry, 1995, 117(2): 160–168
105. Jin T, Stephenson D J. Analysis of grinding chip temperature and energy partitioning in high-efficiency deep grinding. Proceedings of the Institution of Mechanical Engineers, Part B: Journal of Engineering Manufacture, 2006, 220(5): 615–625
106. Hadad M, Sadeghi B. Thermal analysis of minimum quantity lubrication-MQL grinding process. International Journal of Machine Tools &

Manufacture, 2012, 63: 1–15
107. Zhu D H, Li B Z, Ding H. An improved grinding temperature model considering grain geometry and distribution. The International Journal of Advanced Manufacturing Technology, 2013, 67: 1393–1406
108. Jin T, Yi J, Li P. Temperature distributions in form grinding of involute gears. The International Journal of Advanced Manufacturing Technology, 2017, 88: 2609–2620
109. Yang M, Li C H, Said Z, Zhang Y B, Li R Z, Debnath S, Ali H M, Gao T, Long Y Z. Semiempirical heat flux model of hard-brittle bone material in ductile microgrinding. Journal of Manufacturing Processes, 2021, 71: 501–514
110. Rowe W B. Temperatures in grinding—a review. Journal of Manufacturing Science and Engineering, 2017, 139(12): 121001
111. Zheng Y, Wang C Q, Zhang Y F, Meng F M. Study on temperature of cylindrical wet grinding considering lubrication effect of grinding fluid. The International Journal of Advanced Manufacturing Technology, 2022, 121(9–10): 6095–6109
112. Lavine A S. On the linear stability of mixed and free convection between inclined parallel plates with fixed heat flux boundary conditions. International Journal of Heat and Mass Transfer, 1993, 36(5): 1373–1381
113. Kim N K, Guo C, Malkon S. Heat flux distribution and energy partition in creep-feed grinding. CIRP Annals, 1997, 46(1): 227–232
114. Takazawa K. Theory and measuring method of the temperature distribution in ground surface layer. Journal of the Japan Society of Precision Engineering, 1964, 30(358): 851–857
115. Yin G X, Marinescu I D. A heat transfer model of grinding process based on energy partition analysis and grinding fluid cooling application. Journal of Manufacturing Science and Engineering, 2017, 139(12): 121015
116. Li Y X, Eldredge J D, Lavine A S, Fisher T S, Drolen B L. A conjugate heat transfer model of oscillating heat pipe dynamics, performance, and dryout. International Journal of Heat and Mass Transfer, 2024, 227: 125530
117. Jin T, Cai G Q, Jeong H D, Kim N K. Study on heat transfer in super-high-speed grinding: energy partition to the workpiece in HEDG. Journal of Materials Processing Technology, 2001, 111(1–3): 261–264
118. Wei W, Ren J L. Finite element analysis of cutting force and cutting temperature for stainless steel. Tool Engineering, 2009, 43(2): 67–70 (in Chinese)
119. Thomas J A, DeVincentis B, Janz E, Turner B. A general approach for predicting convective heat transfer coefficients in turbulent systems. International Journal of Heat and Mass Transfer, 2024, 220: 124989
120. Gong P, Zhang Y B, Cui X, Xu S Q, Yang M, Jia D Z, Li C H. Lubricant transportation mechanism and wear resistance of different arrangement textured turning tools. Tribology International, 2024, 196: 109704
121. Pervaiz S, Deiab I, Wahba E, Rashid A, Nicolescu M. A numerical and experimental study to investigate convective heat transfer and associated cutting temperature distribution in single point turning. The International Journal of Advanced Manufacturing Technology, 2018, 94: 897–910
122. Zhang D K, Li C H, Zhang Y B, Jia D Z, Zhang X W. Experimental research on the energy ratio coefficient and specific grinding energy in nanoparticle jet MQL grinding. The International Journal of Advanced Manufacturing Technology, 2015, 78: 1275–1288
123. Yin J, Zhou X H, Zhang L, Yang J J, Liu W M, Zhao H J. Deformation analysis of twin-cutter turning slender shaft under thermal-mechanical coupling. Ordnance Industry Automation, 2023, 42: 92–96 (in Chinese)
124. Yi J, Zhou W, Deng Z H. Experimental study and numerical simulation of the intermittent feed high-speed grinding of TC4 titanium alloy. Metals, 2019, 9(7): 802
125. Chen G, Gao Q, Yang X P, Liu J, Su Y X, Ren C Z. Investigation of heat partition and instantaneous temperature in milling of Ti-6Al-4V alloy. Journal of Manufacturing Processes, 2022, 80: 302–319
126. Özerdem B. Measurement of convective heat transfer coefficient for a horizontal cylinder rotating in quiescent air. International Communications in Heat and Mass Transfer, 2000, 27(3): 389–395
127. Wang Y B, Li Z J, Tan G Y, Liu L. Study on boundary condition of temperature field for waved-edge milling insert. Tool Engineering, 2004, 11: 16–19 (in Chinese)
128. Shariar F, Karagüzel U, Karpat Y. Heat partition evaluation during dry drilling of thick CFRP laminates with polycrystalline diamond drills. Manufacturing Letters, 2024, 41: 483–493
129. Farahani S D, Tahmasebi V, Toghraie D. Estimation of heat flux entering the bone during the drilling process using the inverse heat transfer method. International Communications in Heat and Mass Transfer, 2024, 154: 107444
130. Kurgin S, Dasch J M, Simon D L, Barber G C, Zou Q. Evaluation of the convective heat transfer coefficient for minimum quantity lubrication (MQL). Industrial Lubrication and Tribology, 2012, 64(6): 376–386
131. Pontes D W, Crichigno Filho J M, Zdanski P S B. Prediction of the convective heat transfer coefficient of cutting fluid in helical drills. Journal of the Brazilian Society of Mechanical Sciences and Engineering, 2017, 39(12): 5195–5204
132. Jin T, Stephenson D J. A study of the convection heat transfer coefficients of grinding fluids. CIRP Annals, 2008, 57(1): 367–370

133. Kizaki T, Takahashi K, Katsuma T, Tanaka J, Shu L M, Sugita N. Effect of grinding fluid supply on workpiece temperature in continuous generating grinding. Journal of Manufacturing Processes, 2020, 60: 410–417
134. Jin T, Stephenson D J. Three dimensional finite element simulation of transient heat transfer in high efficiency deep grinding. CIRP Annals, 2004, 53(1): 259–262
135. Weber D, Kirsch B, da Silva E J, Aurich J C. 3D-FEM-Wärmeübertragungssimulation des Schleifens. Zeitschrift für wirtschaftlichen Fabrikbetrieb, 2022, 117(7–8): 484–488 (in German)
136. Xie G Z, Huang H. An experimental investigation of temperature in high speed deep grinding of partially stabilized zirconia. International Journal of Machine Tools & Manufacture, 2008, 48(14): 1562–1568
137. Xiao X W, Li B, Peng R T, Hao X Q, Huang X F, Li Y Y, Zhao L F, Chen M L, Gao J X. Analysis of the material removal and heat transfer during internal cooling grinding of GH4169. Journal of Materials Processing Technology, 2023, 322: 118199
138. Shao Y M, Li B Z, Chiang K N, Liang S Y. Physics-based analysis of minimum quantity lubrication grinding. The International Journal of Advanced Manufacturing Technology, 2015, 79(9–12): 1659–1670
139. He Z Y, Jia D Z, Zhang Y B, Qu D, Lv Z L, Zeng E J. Investigation into the heat transfer behavior of electrostatic atomization minimum quantity lubrication (EMQL) during grinding. Lubricants, 2024, 12(5): 158
140. Huang W T, Liu W S, Wu D H. Investigations into lubrication in grinding processes using MWCNTs nanofluids with ultrasonic-assisted dispersion. Journal of Cleaner Production, 2016, 137: 1553–1559
141. Yang M, Li C H, Zhang Y B, Jia D Z, Zhang X P, Hou Y L, Shen B, Li R Z. Microscale bone grinding temperature by dynamic heat flux in nanoparticle jet mist cooling with different particle sizes. Materials and Manufacturing Processes, 2018, 33(1): 58–68
142. Sun L Y, Zhang Y B, Cui X, An Q L, Chen Y, Jia D Z, Gong P, Liu M Z, Dambatta Y S, Li C H. Magnetic lubricants: preparation, physical mechanism, and application. Friction, 2024
143. Yang M, Li C H, Zhang Y B, Wang Y G, Li B K, Li R Z. Theoretical analysis and experimental research on temperature field of microscale bone grinding under nanoparticle jet mist cooling. Journal of Mechanical Engineering, 2018, 54(18): 194–203 (in Chinese)
144. Liu M Z, Li C H, Zhang Y B, Yang M, CuiX, Li B K, Gao T, Wang D Z, An Q L. Heat transfer mechanism and convective heat transfer coefficient model of cryogenic air minimum quantity lubrication grinding titanium alloy. Journal of Mechanical Engineering, 2023, 59(23): 343–357 (in Chinese)
145. Mao C, Zou H F, Huang Y, Zhou Z X. Research on heat transfer mechanism in grinding zone for MQL surface grinding. China Mechanical Engineering, 2014, 25(6): 826–831 (in Chinese)
146. Yang M, Li C H, Zhang Y B, Wang Y G, Li B K, Jia D Z, Hou Y L, Li R Z. Research on microscale skull grinding temperature field under different cooling conditions. Applied Thermal Engineering, 2017, 126: 525–537
147. Jin T, Stephenson D J, Rowe W B. Estimation of the convection heat transfer coefficient of coolant within the grinding zone. Proceedings of the Institution of Mechanical Engineers, Part B: Journal of Engineering Manufacture, 2003, 217(3): 397–407
148. Lin B, Morgan M N, Chen X W, Wang Y K. Study on the convection heat transfer coefficient of coolant and the maximum temperature in the grinding process. The International Journal of Advanced Manufacturing Technology, 2009, 42(11–12): 1175–1186
149. Lin B, Chen X W, Morgan M N, Wu H. Estimation of the convection heat transfer coefficient of coolant and prediction of the maximum temperature within the grinding zone. International Journal of Abrasive Technology, 2009, 2(2): 130–153
150. Jin T, Ma X. Hu H, Qu M N, Shang Z T. Inverse approach to derive the distribution of convection heat transfer coefficient of grinding fluid within grinding zone for deep grinding of nickel based super alloy. Journal of Mechanical Engineering, 2022, 58(15): 55–62 (in Chinese)
151. Gao H, Song Z W, Zhen H W. Experimental determination of cooling CHTC for vertical spindle surface grinding. Diamond & Abrasives Engineering, 1991, 6: 16–20 (in Chinese)
152. Lavine A S, Jen T C. Thermal aspects of grinding: heat transfer to workpiece, wheel, and fluid. Journal of Heat Transfer, 1991, 113(2): 296–303
153. Vinay P V, Srinivasa Rao C. Temperature assessment in surface grinding of tool steels. Journal of Mechanical Science and Technology, 2015, 29(11): 4923–4932
154. Shen B. Minimum quantity lubrication grinding using nanofluids. Dissertation for the Doctoral Degree. Ann Arbor: University of Michigan, 2008, 107–135
155. Zhang L, Rowe W B. Fluid convection models for low-temperature grinding and effect of fluid warming. Journal of Manufacturing Science and Engineering, 2021, 143(2): 021010
156. Zhang L, Rowe W B. Study of convective heat transfer in grinding applied to tool carbide. Journal of Manufacturing Science and Engineering, 2020, 142(2): 021001
157. Wang Y C. Study on effective supply of grinding fluid and convective heat transfer in grinding zone. Thesis for the Master's Degree. Jinan: Shandong University, 2016, 31–40 (in Chinese)
158. Yang M, Ma H, Hao J C, Li Z H, Li R Z, Zhou Z M,

Gao T, Liu M Z, Cui X, Wang X M, Zhang Y B, Dambatta Y S, Long Y Z, Li C H. Droplet size distribution model of needle electrode electrostatic atomization and milling nickel-based alloy performance evaluation. Journal of Manufacturing Processes, 2024, 119: 682–698

159. Yang M, Ma H, Li Z H, Hao J C, Liu M Z, Cui X, Zhang Y B, Zhou Z M, Long Y Z, Li C H. Force model in electrostatic atomization minimum quantity lubrication milling GH4169 and performance evaluation. Frontiers of Mechanical Engineering, 2024, 19: 28
160. Yang M, Li C H, Luo L, Li R Z, Long Y Z. Predictive model of convective heat transfer coefficient in bone micro-grinding using nanofluid aerosol cooling. International Communications in Heat and Mass Transfer, 2021, 125: 105317
161. Wang X Z, Yu T B, Sun X, Shi Y, Wang W S. Study of 3D grinding temperature field based on finite difference method: considering machining parameters and energy partition. The International Journal of Advanced Manufacturing Technology, 2016, 84: 915–927
162. Zhan Y J, Xu X P. An experimental investigation of temperatures and energy partition in grinding of cemented carbide with a brazed diamond wheel. The International Journal of Advanced Manufacturing Technology, 2011, 61: 117–125
163. Li B K, Li C H, Zhang Y B, Wang Y G, Jia D Z, Yang M. Grinding temperature and energy ratio coefficient in MQL grinding of high-temperature nickel-base alloy by using different vegetable oils as base oil. Chinese Journal of Aeronautics, 2016, 29(4): 1084–1095
164. Li Z, Ding W F, Ma C Y, Xu J H. Grinding temperature and wheel wear of porous metal-bonded cubic boron nitride superabrasive wheels in high-efficiency deep grinding. Proceedings of the Institution of Mechanical Engineers, Part B: Journal of Engineering Manufacture, 2017, 231(11): 1961–1971
165. Hou Z B, Yao Z Q. Investigation on grinding temperature and heat flux distribution with grooved grinding wheels. The International Journal of Advanced Manufacturing Technology, 2023, 124(10): 3471–3487
166. Pang J Z, Wu C J, Shen Y M, Liu S Q, Wang Q X, Li B Z. Heat flux distribution and temperature prediction model for dry and wet cylindrical plunge grinding. Proceedings of the Institution of Mechanical Engineers, Part B: Journal of Engineering Manufacture, 2019, 233(10): 2047–2060
167. Ren X K, Huang X K, Chai Z, Li L F, Chen H B, He Y B, Chen X Q. A study of dynamic energy partition in belt grinding based on grinding effects and temperature dependent mechanical properties. Journal of Materials Processing Technology, 2021, 294: 117112
168. Mohamed A M O, Warkentin A, Bauer R. Use of surface roughness measurements to improve the estimation of the heat partition in grinding. Journal of Materials Processing Technology, 2011, 211(4): 566–572
169. Chen J J, Liu S Y, Yang Y, Yuan D D, Zhang L Y, Fu Y C, Qian N. Evaluation of heat transfer performance of nanofluid heat pipe grinding wheel forming and grinding titanium alloy. Journal of Mechanical Engineering, 2024, 60(15): 407–419 (in Chinese)
170. Chen J J, Fu Y C, Qian N, Ching C Y, Ewing D, He Q S. A study on thermal performance of revolving heat pipe grinding wheel. Applied Thermal Engineering, 2021, 182: 116065
171. He Q S, Liu J W, Wang X, Fu Y C. Thermal performance analysis of phase change heat storage grinding wheel in high-efficiency dry grinding. The International Journal of Advanced Manufacturing Technology, 2024, 134(7–8): 3599–3609